KIT SCIENTIFIC REPORTS 7593

Test and simulation results of LIVE-L4 + LIVE-L5L

X. Gaus-Liu
A. Miassoedov
T. Cron
J. Foit
B. Fluhrer
S. Schmidt-Stiefel
T. Wenz

KIT Scientific Publishing

X. Gaus-Liu, A. Miassoedov, T. Cron, J. Foit, B. Fluhrer,
S. Schmidt-Stiefel, T. Wenz

Test and simulation results of LIVE-L4 + LIVE-L5L

Karlsruhe Institute of Technology
KIT SCIENTIFIC REPORTS 7593

Test and simulation results of LIVE-L4 + LIVE-L5L

by
X. Gaus-Liu
A. Miassoedov
T. Cron
J. Foit
B. Fluhrer
S. Schmidt-Stiefel
T. Wenz

KIT Scientific Publishing

Report-Nr. KIT-SR 7593

Impressum

Karlsruher Institut für Technologie (KIT)
KIT Scientific Publishing
Straße am Forum 2
D-76131 Karlsruhe
www.ksp.kit.edu

KIT – Universität des Landes Baden-Württemberg und nationales
Forschungszentrum in der Helmholtz-Gemeinschaft

KIT Scientific Publishing 2011
Print on Demand

ISSN 1869-9669
ISBN 978-3-86644-692-2

Abstract

The sequence of a postulated core melt down accident in the reactor pressure vessel (RPV) of a pressurised water reactor (PWR) involves a large number of complex physical and chemical phenomena. The main objective of the LIVE program is to study the core melt phenomena during the late phase of core melt progression in the RPV both experimentally in large-scale 3D geometry and in supporting separate-effects tests and analytically using CFD codes in order to provide a reasonable estimate of the remaining uncertainty band under the aspect of safety assessment.

The main objective of the LIVE-L4 and LIVE-L5L experiments was to investigate the transient and steady state behavior of the molten pool and the crust at the melt/vessel wall interface influenced by the several melt relocation numbers and different heat generation rate. The test conditions in the LIVE- L4 test were similar to the LIVE-L5L test. In both test the insulation lid was used above the test vessel and the melt was cooled externally with water. The test vessel wall outer wall surface was in almost isothermal condition. Non-eutectic binary material KNO_3-$NaNO_3$ in 80%-20% mole relation was used as stimulant material of corium. The melt height was 430 mm and it was heated homogenously from vessel bottom to 310 mm. In both test there were heating periods in order of 18 kW, 10 kW, 5 kW and 10 kW of 430 mm height pool. The main difference between the two tests was the pouring times. The melt was poured in two charges in LIVE-L5L test whereas in L4 test the total amount of 210 l was discharged only in one melt pour performance. Besides in L4 test the heating power in the last period was 15 kW due to the failure of one heating plane.

The information obtained in the two tests includes transient and steady state melt temperature and heat flux distribution through the RPV wall. The timing of the transient state characterized by the crust growth rate was obtained. The range of crust thermal conductivity and the crust thickness during the test was estimated. The extensive measurements of the melt vertical profiles revealed the heat transfer regimes in the melt pool. The motion pattern and the velocity of the surface melt obtained from the infrared camera give additional information about the movement of the melt. It was observed that that more times of melt pouring and frequent power transition could facilitate gap formation at crust/wall interface and crust rapture with the consequence of filling the gap with hot melt. The crust thickness became thicker after such events.

Besides the experimental program the LIVE-L4 test case was simulated with CONV code. The melt temperature, heat flux distribution and crust thickness was calculated during different power generation rate. The simulation results were validated with the experimental results and showed general good agreement with each other. The measuring error of the test data and the limitation of the code are discussed.

The report summarizes the objectives of the LIVE program and presents the main results obtained in the LIVE-L4 test compared to the LIVE-L5L test.

TABLE OF CONTENTS

LIST OF TABLES

LIST OF FIGURES

Annex A Data Acqusition and instrumentation

Annex B: Test data of LIVE-L4

1 Introduction

The behavior of the corium pool in the lower head is still a critical issue in the understanding of Pressurized Water Reactors (PWR) core meltdown accidents. A number of studies have already been performed to understand of core melting severe accident including its course, critical phases and their timing, and the influence of these processes on the accident progression. The thermal behavior of a single-phase melt pool during steady-state can be meanwhile well modeled [1]-[3]. However, uncertainties still exist in the description of the transient melt behavior, such as formation and growth of in-core melt pool, characteristics of corium arrival in the lower head, and molten pool behavior after debris melting. These phenomena or behaviors are plant and accident sequence dependent and have strong impacts on a potential termination of a severe accident [4]

It is necessary to study the core melt phenomena both experimentally and analytically to provide a reasonable estimation of the remaining uncertainty band in regard to safety assessment. To complement the experimental data on melt pool behavior in the vessel lower head, Karlsruhe Institute of Technology (KIT) performs large-scale tests in the LIVE program [5], [6]. LIVE tests are designed to investigate the core melt behavior in the lower plenum of the reactor pressure vessel and the effect of external water cooling under conditions that may occur during core meltdown accident in PWRs [7]. To simulate the corium melt binary mixtures of sodium nitrate $NaNO_3$ and potassium nitrate KNO_3 are used.

The information obtained from the LIVE experiments includes the melt temperature evolution during different stages of the test, heat flux distribution along the reactor pressure vessel wall in transient and steady-state conditions, crust growth velocity and the influence of the crust formation on heat flux distribution along the vessel wall. In post-test analysis crust thickness profile along the vessel wall, crust composition and crust morphology are determined.

Complimentary to other international programs with real corium melts, the results of the LIVE activities provide data for a better understanding of in-core corium pool behavior. The experimental results are being used for the development of mechanistic models for the describing in-core molten pool behavior and their implementation in the severe accident codes like ASTEC und MELCOR.

2 LIVE-4 and LIVE-L5L test design

2.1 Test facility description

The LIVE test facility consists of 3 main parts: the test vessel including cooling system, the volumetric heating system and a separate heating furnace. All parts of the LIVE test facility are arranged in a scaffold having three levels. On level 0 (the floor of the experimental hall), all cables of measurement signals come together from different control cabinets and are transmitted to the control room next to the experimental hall. In the control room, the data acquisition system and online monitoring systems are arranged. Also the power supply of the heating system and its control system is located on level 0.

On level 1, the LIVE test vessel is positioned. The LIVE test vessel is a 1:5 scaled reactor pressurized vessel (RPV) of a typical PWR. For the first and second phase of the LIVE experimental program (LIVE 1 and LIVE 2), only the hemispherical bottom of the RPV is used (Figure 1). The inner diameter of the test vessel is 1 m and the wall thickness is ~ 25 mm. The test vessel is fabricated from stainless steel. To investigate the influence of different external cooling conditions on melt pool behavior, the test vessel is enclosed by a second vessel (cooling vessel) to be able to cool the test vessel externally. The cooling water inlet is located at the bottom of the cooling vessel and the outlet is positioned at the top of the vessel. The volumetric heating system inside the test vessel is also shown in Figure 1. More details on the heating system are given in the section 2.3.

Figure 1: Picture of the LIVE test vessel with volumetric heating system

The top of the LIVE test vessel just before the start of a LIVE test is shown in Figure 2. The LIVE test vessel and the cooling vessel are installed on three steel beams. The cooling vessel is enclosed with an insulation layer. The test vessel is covered with a lid at the top. This lid consists of a layer of 102 mm insulation materials surrounded by 20 mm stainless steel plate at the top and 1 mm stainless plate at the sidewall and at the bottom. Additionally, there is a 1 mm shield plate mounted 5 mm below the insulation layer to protect the lid from the radiation of hot melt (Figure 3).

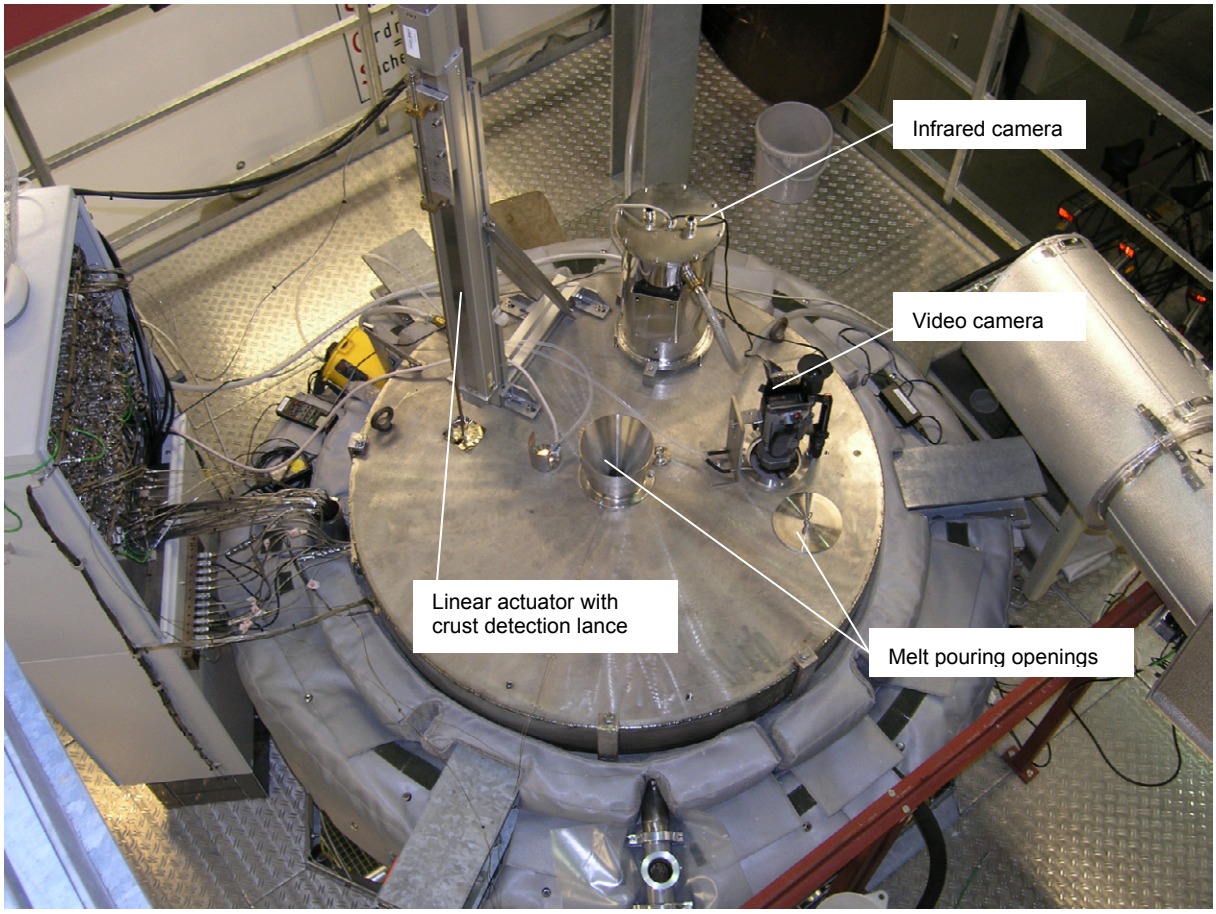

Figure 2: View from the top of the LIVE test vessel before the start of the test

The lid has several openings. There are two melt pouring openings to allow pouring of the melt centrally or close to the side wall of the lower. The pouring position near the wall is located at polar angle 65.5°, and the azimuth angle157.5°. There are different small openings to allow lighting up the vessel (for optical observation) or taking melt samples during the test. These small openings can also be used for a crust detection lance. Additionally there are two openings for video observation of the melt surface. The atmosphere between the melt surface and the upper lid is filled with nitrogen. The flow rate of nitrogen covering is 2 l/min.

To allow fast pouring of melt into the test vessel, the melt is produced in the external heating furnace (Figure 4). The capacity of the heating furnace is 220 l. If scaled to reactor case, this melt amount corresponds to the most conservative core melt down situation with 100% anticipated melting of the core inventory including both oxide and metallic components [8]. The maximum temperature of the heating furnace is 1100 °C. The heating furnace is mounted on

a lifting device and is controlled in a separate scaffold, which is integrated into the scaffold of the test facility. During the pouring process the heating furnace can be tilted and moved upwards at the same time so that the pouring orifice remains at the same position.

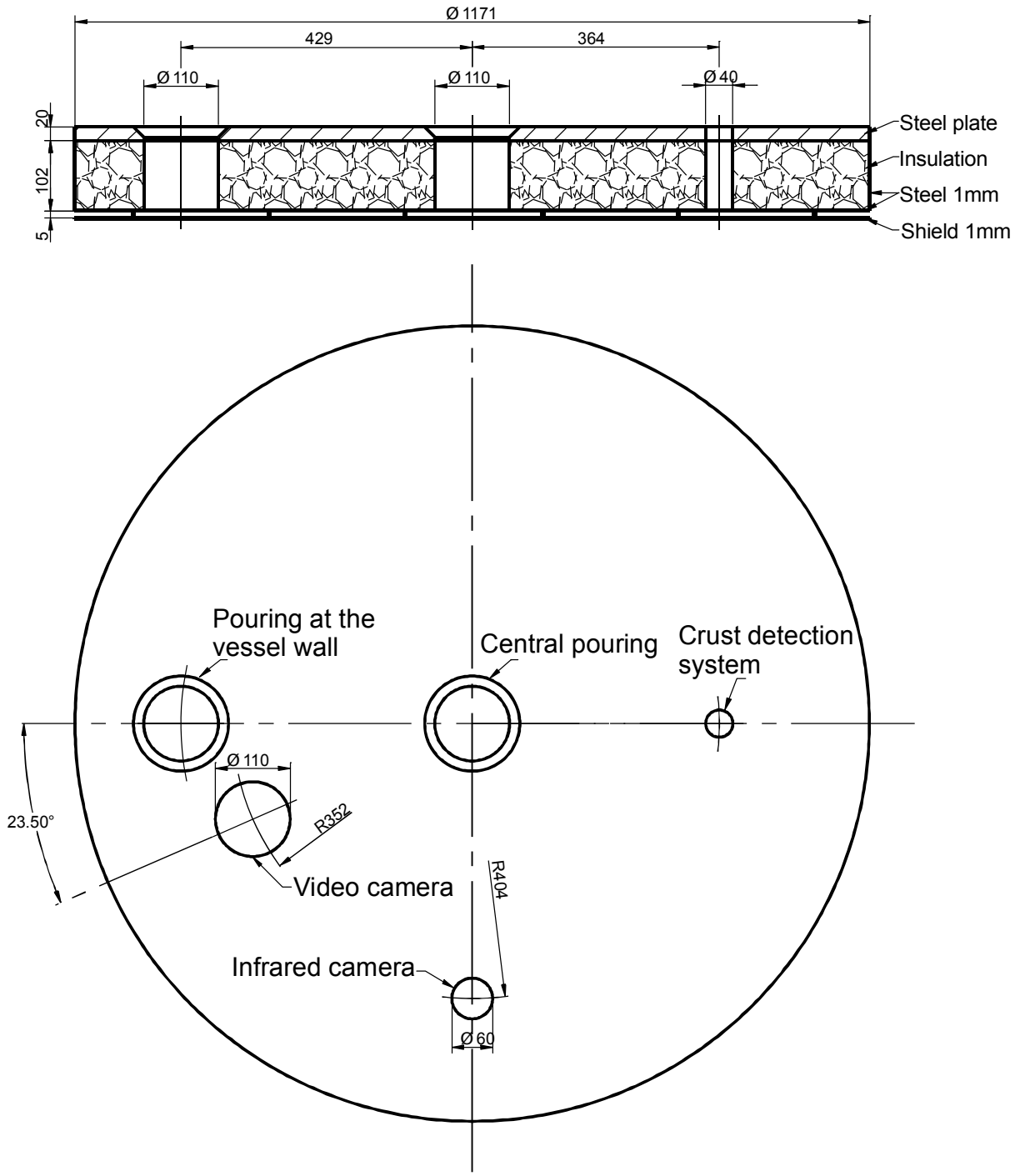

Figure 3: Scheme of the insulation lid on the top of the LIVE test vessel

Figure 4: Picture of the heating furnace for the melting of simulant materials

Before the pouring initiation, the melt is heated to designed temperature and the heating furnace is driven to the start vertical position. The pouring operation is started by tilting the heating furnace. Melt is discharged with into the test vessel via a heated pouring spout. The beginning of the test (0 second) is defined as the time point of the first response of the thermocouple in the pouring spout ST1. The amount of the discharged melt is defined by the final tilting angle and the melt mass flow rate depends on tilting velocity. There are two pouring spouts available for the melt pouring either to the centrally or near the test vessel wall, as shown in Figure 5. In addition, the heating furnace is equipped with a vacuum pump in order to extract the residual melt out of the test vessel back into the heating furnace at the end of the experiment, so that the crust formed during the test can be uncovered. In this way, the crust thickness and the total mass of the crust can be measured after one test. The atmosphere in the heating furnace is filled with nitrogen during melt preparation.

The control panel of the heating furnace is installed at level 2 of the LIVE test facility. From this level the heating furnace is charged with solid melt components.

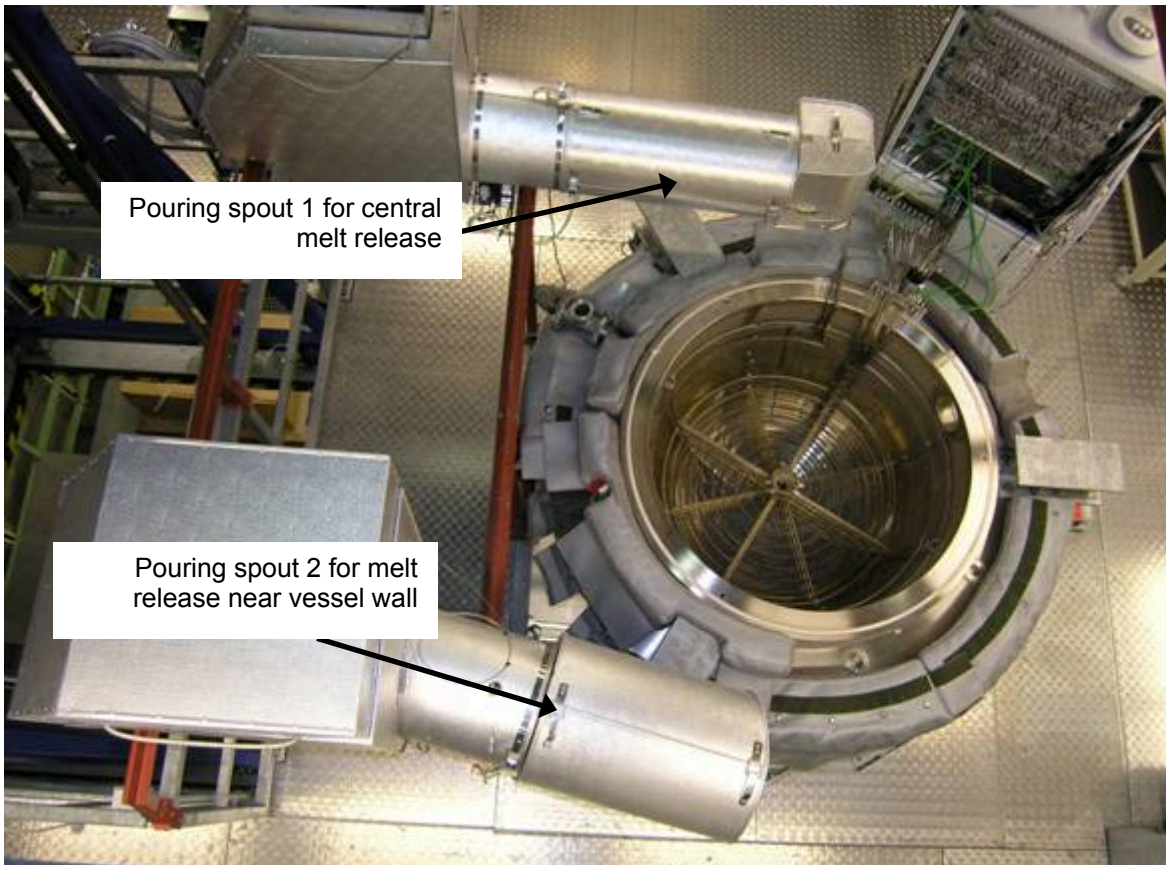

Figure 5: Top view of the LIVE test vessel with pouring spouts

2.2 Melt composition and melt generation

2.2.1 Selection of simulant materials

Simulant materials used in the LIVE program should, to the possible greatest extent, represent the real core materials in important physical properties and in thermo-dynamic and thermo-hydraulic behaviour. Therefore, the applicability of several binary melt compositions as a simulant for the oxidic part of corium has been investigated. Important criteria for the selection are that the simulant melt should be a non-eutectic mixture of several components with a distinctive solidus-liquidus range, and that the simulant melt should have similar solidification behaviour as the oxidic corium. Moreover, the simulant melt should not be toxic and aggressive against steel and vessel instrumentation. And finally, the temperature of the simulant melt should not exceed 1000 °C distinctively because of the technical handling and the selection of a volumetric heating system and a heating furnace.

For the first series of experiments binary mixtures of sodium nitrate $NaNO_3$ and potassium nitrate KNO_3 are used. However, since the nitrate salts are soluble in water, the application of such melts is restricted to dry conditions inside the test vessel. The eutectic composition of this melt is 50-50 mole% and the eutectic temperature is 225 °C [16]. The maximum temperature range between solidus and liquidus is ~60 K and corresponds to a 20-80 mole% $NaNO_3$-KNO_3 mixture. This melt composition can be used in a temperature range from 284 °C (liquidus) to 370 °C (chemical decomposition). Although the mixtures of KNO_3 and $NaNO_3$ are often applied in the simulation of corium melt in nuclear engineering, the exact phase

diagram, especially the position of the solidus line, is still in discussion [9]. Due to this uncertainty, we have measured the liquidus line of KNO_3-$NaNO_3$ mixtures [14]. The measured liquidus from 100 % KNO_3 to 50 mole% KNO_3 – 50 mole% $NaNO_3$ are given in Table 1. The liquidus line was also shown in Figure 6. The liquidus temperature at 20-80 mole% $NaNO_3$-KNO_3 composition of our own measurement is 284.4 °C.

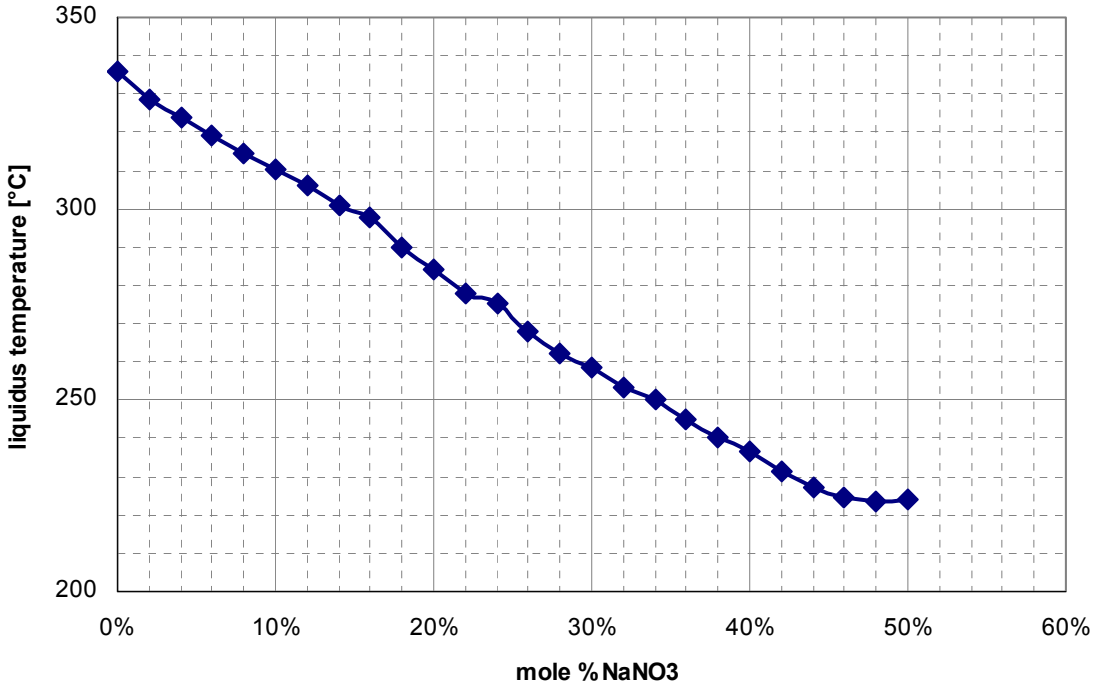

Figure 6: KNO_3-$NaNO_3$ phase diagram measured with Optimelt by KIT

Table 1: Liquidus temperature of KNO_3-$NaNO_3$ mixture (KNO_3 100 mole % to 50 mole %)

KNO_3, mole%	Liquidus, °C	KNO_3, mole%	Liquidus, °C
50	223.8	76	275.2
52	223.7	78	278.0
54	224.4	80	284.4
56	227.2	82	290.1
58	231.4	84	297.8
60	236.7	86	300.7
62	240.4	88	306.0
64	245.0	90	310.1
66	250.0	92	314.2
68	253.5	94	319.0
70	258.3	96	324.1
72	262.2	98	328.5
74	267.9	100	336.0

2.2.2 Melt preparation and generation

For the experiments LIVE-L4 and LIVE-L5L the non-eutectic 20-80 mole% $NaNO_3$-KNO_3 melt composition was used. In Table 2 the properties of the simulant material cited from literature and from the own measurement of KIT are given. In both experiments LIVE-L4 and LIVE-L5L, the heating furnace was loaded with new melt components, which means that the residual melt of the previous tests was not recycled anymore. Therefore, in each case, the heating furnace was loaded with 68 kg $NaNO_3$ and 324 kg KNO_3 powder to produce about 210 l melt of the desired composition.

Table 2: Properties of 80 mol% KNO_3-20 mol% $NaNO_3$

80 mol KNO_3- 20 mol% $NaNO_3$	Solid	Liquid
Mol weight, [g/mol]	97.88 g	97.88
Particle density, [g/cm³]	2.1-2.26 [own measurement]	284°C: 1.914; 340 °C: 1.873 [10]
Transition temperature, [°C]	104. 8°C [own measurement]	284.4 °C [own measurement]
Transition/fusion enthalpy, [J/g]	65.7 60°C-118°C [own measurement] 42.27 [Segal]	161.96, 220°C-286°C [own measurement]
Heat capacity [J/g/°C]	1.14 at 100 °C; 1.328 at 210 °C [Segal]	1.46 [13]] 1.369 [16]
	0.9474+0.00113·T (°C) (119°C<T<182°C) [own measurement]	1.2475+2.8E-4·T (300°C<T<400°C) [own measurement]
Thermal conductivity [W/(mK)]	0.4-0.6 [LIVE crust data]	0.458-0.46 at 50%-50% 0.42 at 100% KNO_3 [12]
Viscosity [pa·sx10^3]		280°C: 3.772; 350°C: 2.508 [16]

After loading the heating furnace, the mixture was heated up for about 3 days to obtain the designed temperature of 350 °C. This temperature was kept before the test initiation. During this period the atmosphere in the heating furnace was filled with nitrogen at 2 l/min to avoid the chemical decomposition of the melt.

2.3 Decay heat simulation

The heating system in the test vessel should simulate the volumetric decay heat released from corium melt. Consequently, the heating system has to produce the heat in the melt as homogeneously as possible. Therefore a heater grid with several independent heating elements was constructed, as shown in Figure 7. The heating elements are shrouded electrical resistance wires. The maximum designed temperature of the heating system is 1100 °C. To allow a quasi-homogeneous heating of the melt pool, the heating system has six heating planes at different elevations with a distance of about 45 mm. Each heating plane consists of a spirally formed heating element with a distance of ~40 mm between each winding. The heating elements are located in a special cage to ensure the correct positioning. To realise a quasi-homogeneous heating of the melt, each plane can be controlled separately. The six heating planes can created a homogenous heating in the melt below 310 mm. The melt height in L4 and L5l tests were about 431 mm, thus the melt region above 310 mm height was not heated.

The power, which the heating coil of each plane can provide, is determined by the length of the heating wire, the corresponding resistance and the supplied voltage. The maximum power of the heating planes and the vertical position of the heating planes in the test vessel are given in Table 3. For the quasi-homogeneously heating below height 310 mm, the maximum heating power is limited to 18.5 kW

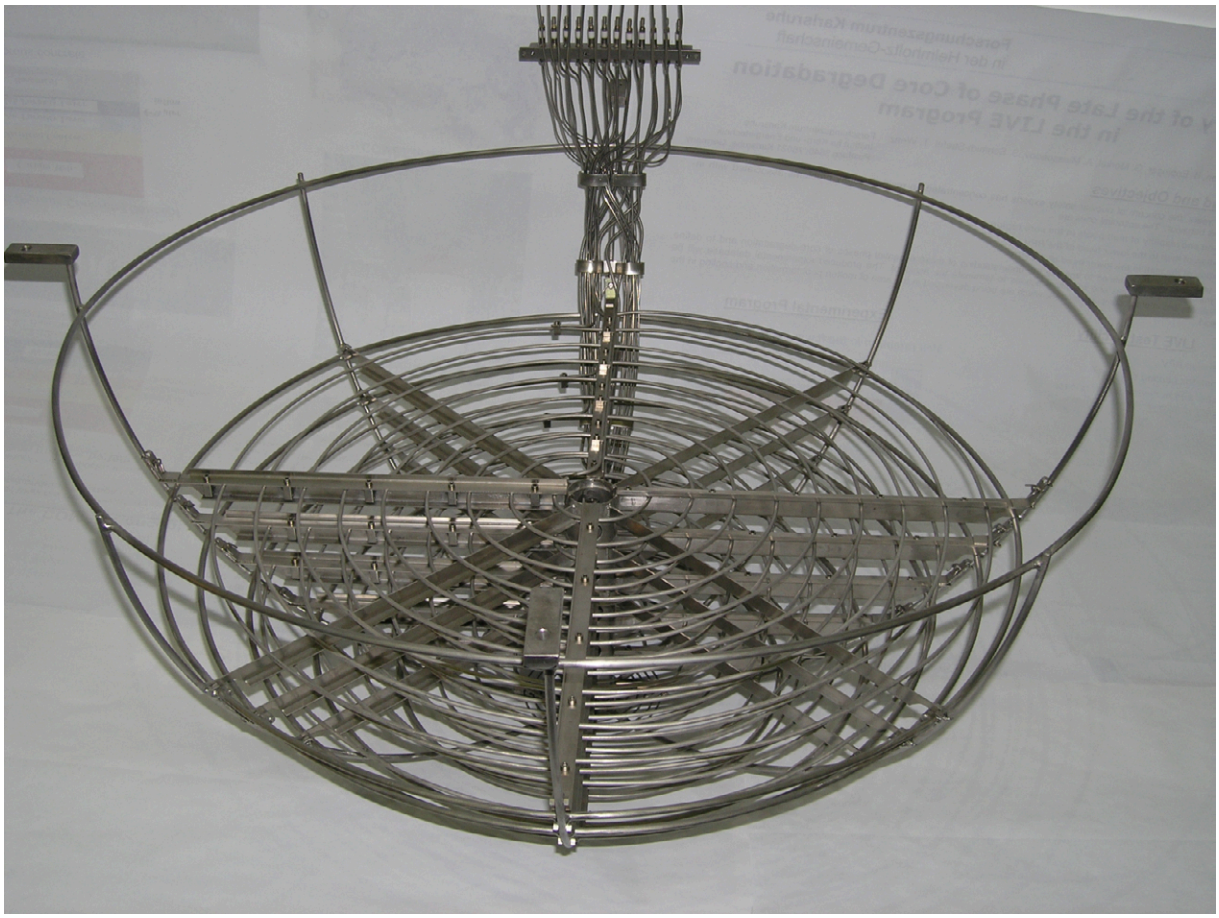

Figure 7: LIVE volumetric heating system

To control the heating system and to avoid the overheating of the heating elements, two monitoring thermocouples are installed at each heating element: one at the outer region and another one at the inner region of the heating element coil. The power switches off automatically when the surface temperature of the heating coils exceeds 380 °C to avoid the overheating and chemical decomposition of the melt.

The heating system is controlled by a separate PC control system, which is independent from the PC data acquisition system. The programme Visual Designer 4.0 is used to store and to display the performance of the heating system and the measurement signals.

Table 3: Characteristics of the LIVE heating system

Heating plane	height of the heating planes from the test vessel bottom [mm]	Diameter of the heating elements [mm]	Maximum power measured during commissioning [W]
1	282.4	4	5300
2	237.2	4	6607
3	189.2	4	6624
4	140.2	4	2715
5	91.7	3	2338
6	39.7	2	1080
			Σ 24464

2.4 Facility Instrumentation and data acquisition

The LIVE test facility is extensively instrumented to monitor and control the experiment and to collect data for subsequent evaluation. All data are stored on PC data acquisition system running under the Visual Designer 4.0. The measuring channels, the designation of the signals and the measuring positions are listed in the instrumentation list in Annex .A.1.

In Figure 8 a scheme of LIVE test vessel with some instrumentation is given. To measure the temperature at the inner and outer surface of the vessel wall, 17 thermocouples are installed at five levels and along 4 azimuth angles at 22.5°, 112.5°, 202.5° and 292.5° on the inner wall surface (named IT) and 17 thermocouples at the same locations on the outer wall surface (named OT). The positions of the IT and OT thermocouples are given in the Figure A- 1 and Figure A- 2 in the Annex .A.2. Temperatures measured at these locations are used to calculate the heat flux through the vessel wall. The temperatures at the insulation lid upper surface (named DTA) and at the downside of the protection shield below the insulation lid (named DTI) are measured at the center area and near the vessel wall. The temperatures are documented by the paper writer (Figure A- 11). With these temperatures the heat loss through the insulation lid can be estimated.

Furthermore, 36 thermocouples are positioned in the melt pool to measure the melt pool temperatures at different positions (named MT). The positions of the MT thermocouples are given in Figure A- 3 to Figure A- 7. The thermocouples are uniformly distributed in the melt at a distance of 100 mm in horizontal and vertical direction between each other. The thermocouples are mounted at the cage of the volumetric heating system.

To quantify the crust growth rate at the vessel wall and the crust thermal conductivity, three thermocouple trees were installed. The thermocouple trees were attached at the inner vessel wall along the azimuth angle of 35°. Each thermocouple tree consists of 7 thermocouples, which are arranged parallel to the vessel wall. At the lowest position (polar angle of 37.6°), thermocouple tree CT4 was used in LIVE-L4 test with the thermocouples at 0, 9, 18, 27, 36, 45, 54 mm in the melt., whereas in LIVE-L5L, a combination of CT1 and CT4 was applied. The positions of the thermocouples at this position were 0, 5, 10, 15, 20, 25, 30, 45, 54 mm in the melt. For the other two thermocouple trees CT2 and CT3, which are positioned at polar angles of 52.9° and 66.9° respectively, the distance of the thermocouples from the inner vessel wall is 0, 3, 6, 9, 12, 15, 18 mm in both test (Figure A- 8). Here the distance between the thermocouples is smaller comparing to the lowest thermocouple tree, since thinner crust was expected at these positions.

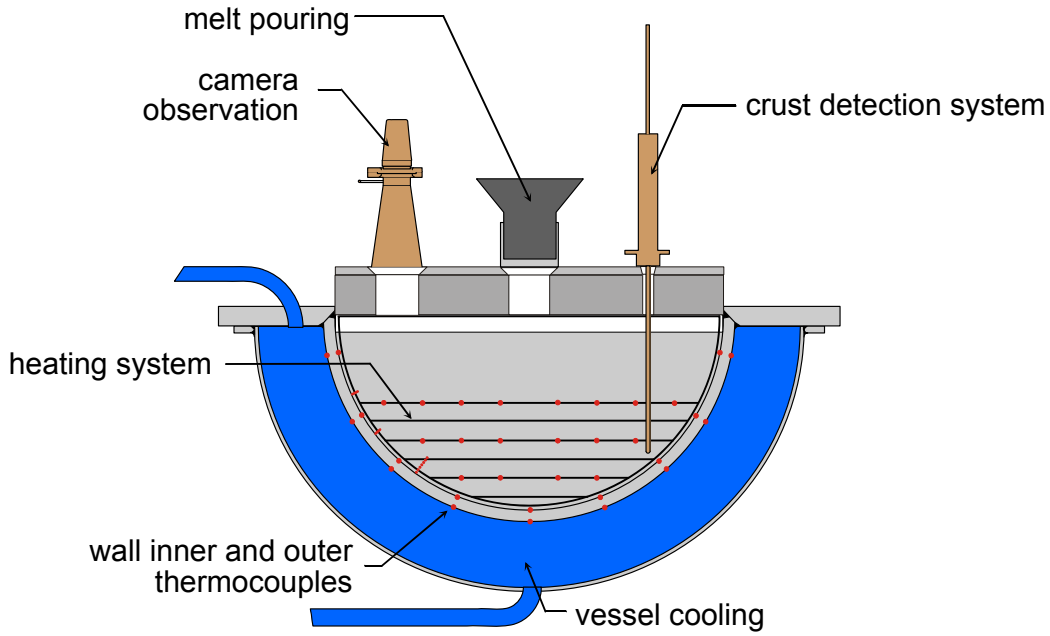

Figure 8: Scheme of the LIVE test vessel with some instrumentation

The melt pool vertical temperature profile and the boundary temperature at the melt/crust interface can be measured by a crust detection system. A picture of the crust detection system mounted on the lid of the test vessel is shown in Figure 9. The crust detection system consists of a linear actuator and a measuring probe. The linear actuator is mounted on the lid of the test vessel. The measuring probe is driven vertically into the melt by the linear actuator at 0.1 mm accuracy. The position of the crust detection system on the lid is at radius 365 mm and azimuth angle 340°. At the bottom part of the probe 5 thermocouples are horizontally

arranged with vertical distance of 5 mm between each other. When the measuring probe touches the crust front, the temperature of the lowest thermocouple stops to change. By moving the lance with small steps, melt boundary temperature and melt pool vertical temperature profile can be determined.

In addition, several video systems are installed to observe the pouring process and the behaviour of the melt surface during one experiment, including:

- a conventional video camera mounted on the upper lid of the test vessel viewing the surface of the melt;

- an infrared (IR) video camera mounted on the upper lid of the test vessel viewing the surface of the melt with a ZnSe window. The view area of the camera is 22x17 cm. This camera operates in the IR wavelength range from 7.5 to 13.0 μm and produces a real-time infrared recording with a frequency of 0.25 s to 5 s according to the needs of the experiment. Motion pattern and flow velocity at the melt surface can be recorded by the IR camera;

- a video camera installed at the side of the test vessel. With this camera, the pouring process of the melt can be observed in more detail.

Melt samples are extracted during the steady state of each test heating period to analyse the actual bulk melt liquidus temperatures, which is also the melt/liquidus temperature of each heating period. At the end of each test, the melt was extracted out of the test vessel. The crust at the vessel wall was uncovered for the post test analysis. The weight of the crust can be determined by the difference of the vessel weight before and after the melt extraction. At the outer surface of the cooling tank three thermocouples are installed to measure the temperature between the cooling tank and the insulation layer.

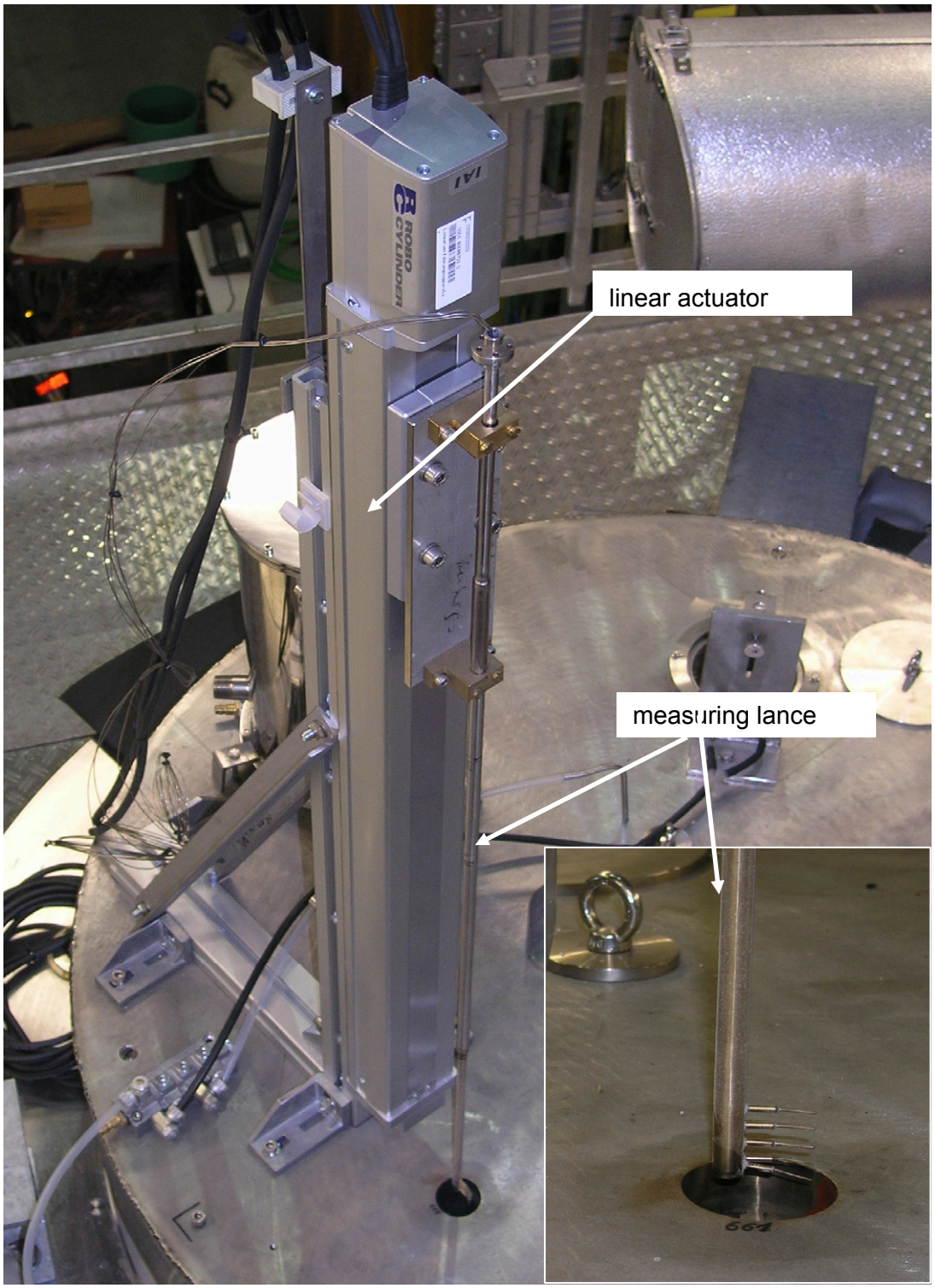

Figure 9: Crust detection system mounted on the lid of the test vessel

3 Preparation and test conditions of LIVE-L4

The experiment LIVE-L4 was successfully conducted on October 15-17, 2008. The simulated core melt was generated in the heating furnace as described in section 2.2.2. The experiment started with the melt pouring from the heating furnace into the test vessel. Five heating phases were conducted. The planned heating powers of the heating phase in chronological order were 18 kW-I, 10 kW-I, 5 kW, 10 kW-II and 18 kW-II respectively. Due to the defect of a heating plan at the beginning of the last heating phase 18 kW, only about 15 kW of the total heating power could be reached. In Table 4 the main test parameters and the performed test phases are summarised. Each heating phase lasted several hours so that the thermal hydraulic steady state was assumed to be established at the end of each heating phase. The melt was discharged in one single central pouring and the planned initial temperature of the melt was 350 °C. The poured mass was 210 l and corresponds to the most conservative core melt down situation with 100% anticipated melting of the core inventory including both oxidic and metallic components.

The cooling vessel was already filled with water before the test and 4 minutes before start of melt pouring the flow rate of the cooling water was started with a value of ~1.3 kg/s. These conditions allow fast crust formation and the boundary conditions with this flow rate of cooling water are nearly isothermal. The measured water flow rate is shown in Figure 10.

Table 4: Designed test parameter and test phases of the experiment LIVE-L4

	LIVE-L4 **15-17.10.2007**	
Melt characteristics and preparation		
Type	$NaNO_3$	KNO_3
Mole %	20 %	80 %
Mass	68 kg	324 kg
Total mass	392 kg	
Loading of the furnace	~455 l powder (for T=20 °C) ~210 l melt (for T=350°C)	
Poured Mass	210 l (corresponds to ~43.5 cm melt height)	
Initial temperature	350 °C	
nitrogen covering of heating furnace	2 l/min	
Melt pour		
Position	central	
Number of pours	1	
Furnace tilting velocity	0.5 °/s	
Furnace target angle	91°	

Hold time	120 s
Trace heating pouring spout	360 °C
Phase 1: 18 kW-I	
Start pouring	0 s
Start heating	84 s
Cooling conditions	Water, continuous cooling
Cooling water flow rate	~1.3 kg/s
Heating planes	All
Heating power	18 kW
Heat generation	Homogeneous for 31 cm melt height [1]
Maximum melt temperature	370 °C
Phase 2: 10kW-I	
Test conditions	Reaching of steady state conditions in Phase 1
Start time	23484 s (6.52 hours)
Boundary conditions	Water, continuous cooling
Cooling water flow rate	~1.3 kg/s
Heating planes	All
Heating power	10 kW
Heat generation	Homogeneous for 31 cm melt height
Maximum melt temperature	370 °C
Phase 3: 5kW	
Test conditions	Reaching of steady state conditions in Phase 2
Start time	87011 s (24.12 hours)
Boundary conditions	Water, continuous cooling
Cooling water flow rate	~1.3 kg/s
Heating planes	All
Heating power	5 kW
Heat generation	Homogeneous for 31 cm melt height [1]
Maximum melt temperature	370 °C
Phase 4: 10kW-II	
Test conditions	Reaching of steady state conditions in Phase 3
Start time	113571 s (31.5 hours)
Boundary conditions	Water, continuous cooling
Cooling water flow rate	~1.3 kg/s
Heating planes	All
Heating power	10 kW
Heat generation	Homogeneous for 31 cm melt height [1]

Maximum melt temperature	370 °C
Phase 5: 15kW	
Test conditions	Reaching of steady state conditions in Phase 3
Start time	173930 s (48.3 hours)
Boundary conditions	Water, continuous cooling
Cooling water flow rate	~1.3 kg/s
Heating planes	All
Heating power	Planned 18 kW, due to failure of heating plane 4 only 15.4 kW could be realised
Heat generation	Not homogeneous due to the failure of heating plane 4
Maximum melt temperature	370 °C
Phase 6: Test termination and melt extraction	
End time	195221 s (54.23 hours)
Test conditions	Reaching of steady state conditions in Phase 5
Heating power	0 kW

[1]: Since the highest plane of the heating wire located at 282 mm above the vessel bottom (Table 3), homogenous heating was created in the melt pool from bottom up to 310 mm of vessel height. Above this height, the melt located in a convection zone.

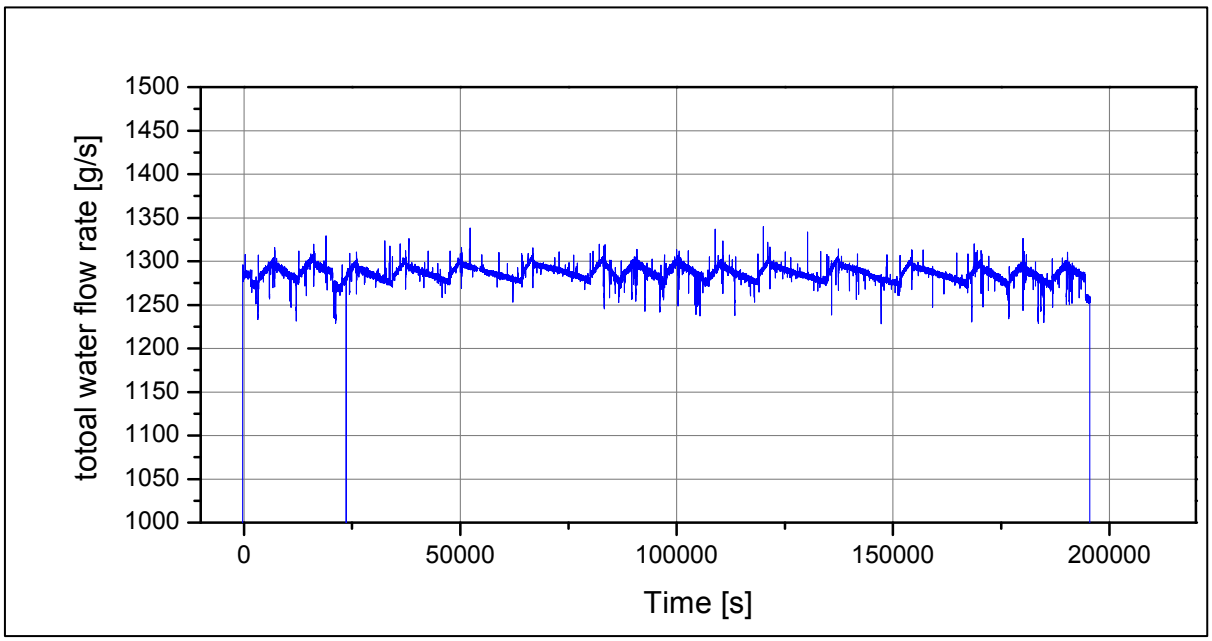

Figure 10: Flow rate of cooling water in LIVE-L4

In Table 5 the course of the test LIVE-L4 is described in chronological order.

Table 5: Course of the experiment LIVE-L4

Time of day	Event
15.10.2007	
8:03	Melt temperature in furnace 350 °C and 345 °C
8:50	PC data acquisition start
8:55	Weight of test vessel 2013 kg
8:56	Outer vessel cooling start, ~1.3 l/s
8:58	Video record pouring start
8:58:30	Video record vessel vertical and lateral start
8:59	IR camera record start
9:00	Start of pouring program of heating furnace
9:03:15	Heating system on, P = 18 kW homogeneous under 31 mm
9:06	Weight of test vessel 2400 kg (without pouring spout)
9:25	Video record vessel stop
9:08:20	Heating of heating furnace switched-off
15:00	Start measurement with crust detection lance
15:28	Extraction first melt sample through central pouring opening in the lid
15:33	Reduction of heating power, P = 10 kW homogeneous under 31 mm
16:45	Start night operation
16.10.2007	
8:32	Start measurement with crust detection lance
8:47	End measurement with crust detection lance
8:51	Extraction second melt sample through central pouring opening in the lid
9:00	Reduction of heating power, P = 5 kW homogeneous
9:55	Video record vessel lateral in time intervals start
15:05	Start measurement with crust detection lance
15:30	End measurement with crust detection lance
16:25	Increase of heating power, P = 10 kW homogeneous under 31 mm
16:45	Start night operation
17.10.2007	
8:39	Start measurement with crust detection lance
8:48	End measurement with crust detection lance
9:00	Extraction third melt sample through central pouring opening in the lid
9:09	Increase of heating power, P = 18 kW homogeneous under 31 mm
9:14	Start of decrease of heating power of heating plane 4
9:30	Heating plane 4 failed through short-circuit; further operating without

	heating plane 4
14:37:30	Video record lateral in time intervals stops
14:39	Start measurement with crust detection lance
14:43	End measurement with crust detection lance
14:49	Extraction fourth melt sample through central pouring opening in the lid
14:59	Weight of test vessel 2407 kg (without suction tube, with suction funnel)
14:59	Video record test vessel start
15:02	Weight of test vessel 2412 kg (with suction tube)
15:03:25	Start extraction of residual melt
15:03:30	Heating power 0 kW
15:04:45	Extraction end
15:06	Weight of test vessel 2066 kg (without suction tube)
15:08	Cooling water off
15:16	Video record stop
15:20	PC data acquisition stop

4 LIVE-L4 test results

4.1 Melt mass and water temperature

The experiment LIVE-L4 started with the pouring of the simulated corium melt from the heating furnace centrally into the LIVE test vessel via the preheated pouring spout. The experimental time t = 0 s is determined by the first response of the ST1 thermocouple located in the pouring spout. The initial temperature of the $NaNO_3$-KNO_3 melt in the pouring spout was about 343 °C, which was in good agreement with the planned 350 °C.

The mass of the test vessel during the pouring of the melt rose from about 2013 kg to 2400 kg (Figure 11). Therefore about 387 kg of nitrate melt has been poured into the test vessel. With a density of about 1871 kg/m^3 for a 20-80 mole% $NaNO_3$-KNO_3 melt with a temperature of 343 °C, determined in [10], a volume of ~207 l nitrate melt has been poured into the test vessel. This value was in good agreement with the planned 210 l melt. The pouring lasted about 100 s. The maximum pouring rate derived from the analysis of the weight of the test vessel was ~6 kg/s.

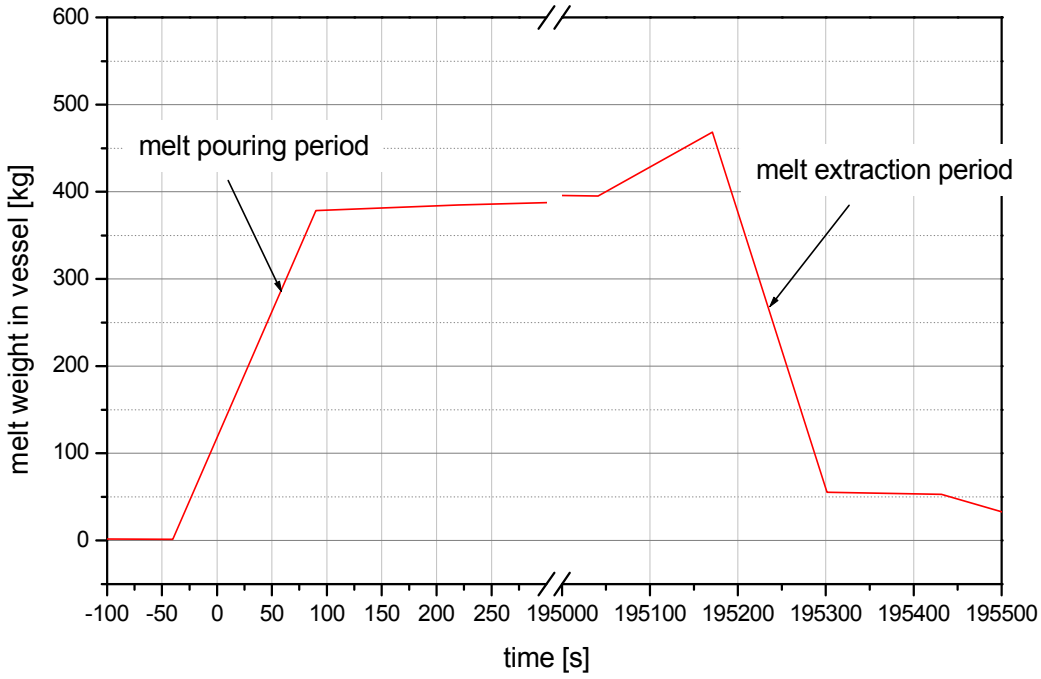

Figure 11: Weight of the test vessel and melt release rate in LIVE-L4

The inlet temperature of the cooling water was about 15.4 °C and the outlet temperature was dependent on the heating power and differed from 16 °C to 19 °C, as shown in Figure 12. The high flow rate and the correspondent minor difference in the water temperature inside the cooling vessel created a quasi isothermal condition on the outer surface of the test vessel.

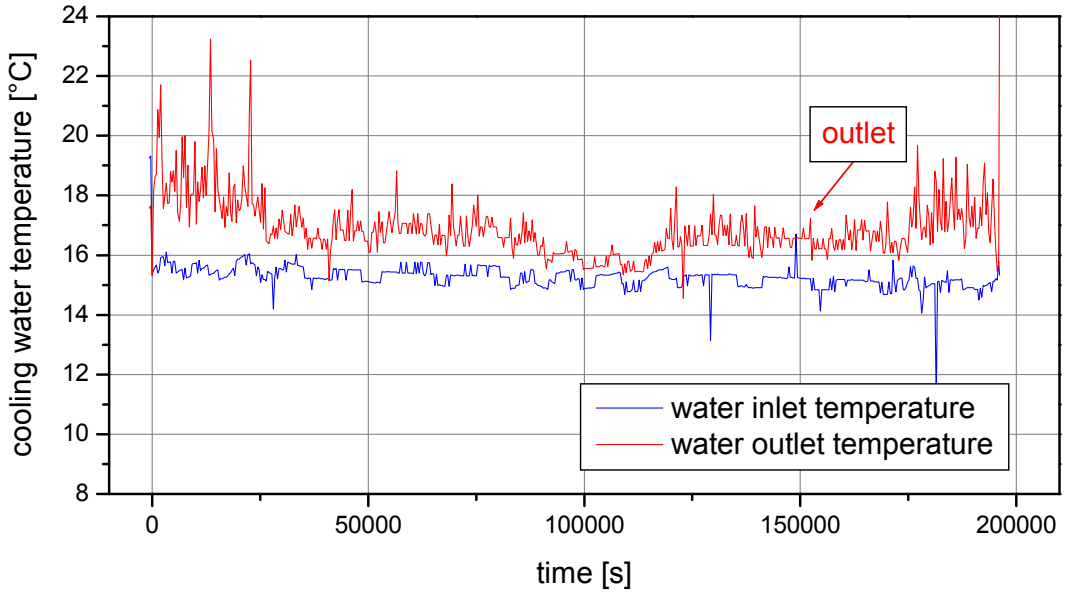

Figure 12: Cooling water inlet temperature and outlet temperature during LIVE-L4

4.2 Decay heat simulation in LIVE-L4

The decay heat was simulated by 6 planes of heating wires. The heating system was described in detail in 2.3. In LIVE-L4 test the maximum homogenous volumetric heating power was 18 kW for the melt pool region from vessel bottom to 31 cm of vessel height. The melt surface in L4 was about 43.5 cm from vessel bottom. In the upper part of the melt pool which was above 31 cm, there was no heating input. In Table 6 the heating periods and real heating powers of each plane of the 6 heating periods are given. The real total heating powers in each heating period was in gut agreement with the planed heating power except the last heating period.

Table 6: Heating power and heating periods during LIVE-L4

	Heating period	**18 kW** 84-23483 s	**10 kW-I** 23484-87010 s	**5 kW** 87011-113570 s	**10 kW-II** 113571-173929 s	**15 kW** 173230-195221 s
	Height [mm]	[W]	[W]	[W]	[W]	[W]
HE1	36.4	5138	2881	1477	2881	5131
HE2	90.4	4075	2263	1133	2260	4064
HE3	135.4	3393	1849	895	1849	3386
HE4	182.4	2586	1438	726	1440	1
HE5	233.4	1942	1069	527	1069	1937
HE6	278.4	930	514	257	515	927
total		18064	10015	5015	10014	15445

During the last heating period, which was foreseen 18 kW, the heating plane 4 failed after about 174180 s and only a power level of ~15.4 kW could be realised. Due to the failure of heating plane 4, the homogeneous heating of the melt could not be realised anymore, but nevertheless, this reduced power level was kept for about 5.8 hours.

The heating power distribution between the heating planes is shown in Figure 13.

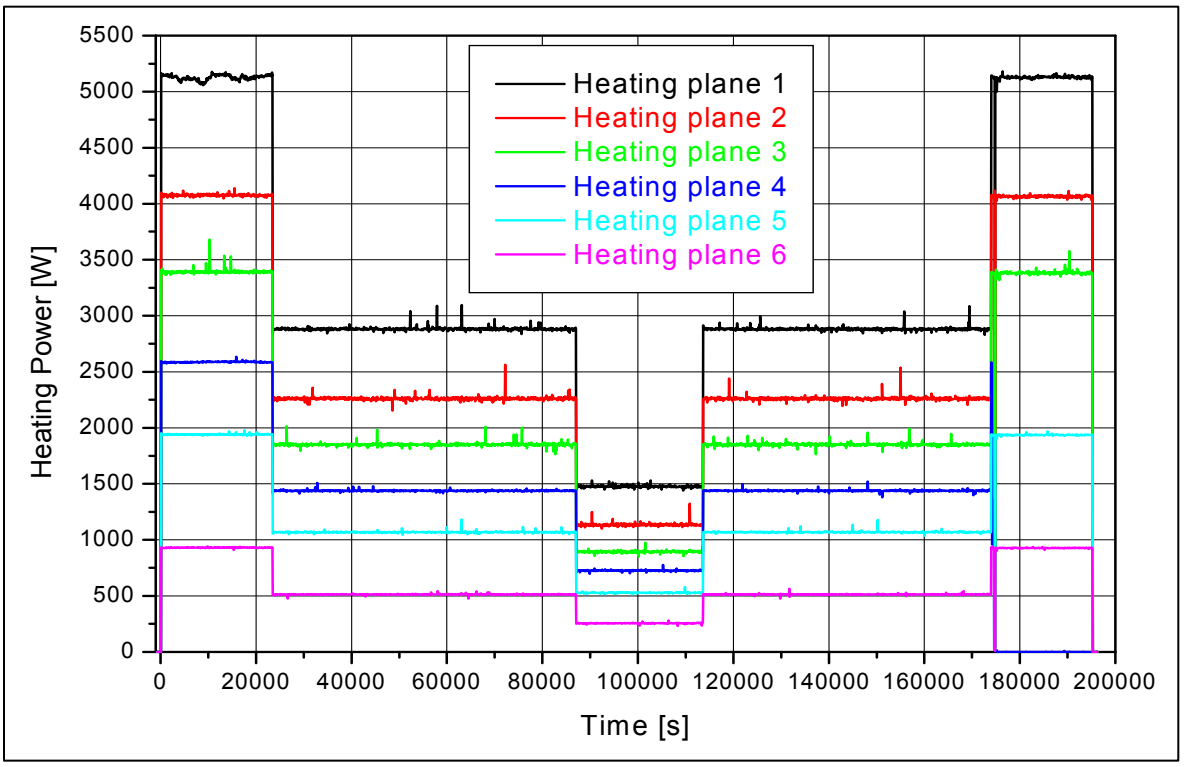

Figure 13: Heating power generated by each heating plane in LIVE-L4

4.3 Melt behaviour in LIVE-L4

The melt pool temperature can be observed with the 36 MT thermocouples (Figure A- 4 in Annex .A.2) distributed evenly below the melt height 27 cm during the whole experimental period and with the crust detection system. The crust detection lance can measure the thickness of the boundary melt layer and detailed vertical temperature profiles at polar angle 47°, radius 365 mm and azimuth angle 340°.

4.3.1 Melt temperature measured by MT thermocouples

The change of melt temperatures during power transition periods are shown in Figure 14. After melt pouring the melt pool underwent formation of temperature stratification, which led to a slight increase of the melt temperature at the top region during the initial period. This phenomenon was not observed when the melt pool temperature stratification already existed, as the case of the transition from 18 kW to 10 kW and from 10 kW to 5 kW. During all the cases of heating power reduction, the melt temperature near the surface decreased more slowly than the lower part of the melt. Near the top surface the duration from power transition to the time that the melt temperature became stabile took about 1500 s after melt pouring,

3500 s after the transition of 18 kW to 10 kW and 5000 s after the transition of 10 kW to 5 kW.

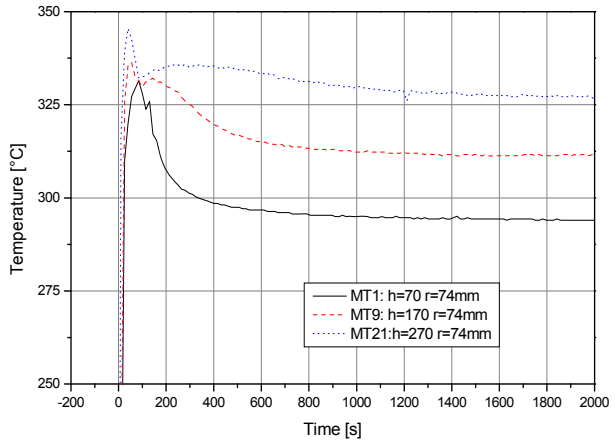

After melt pouring

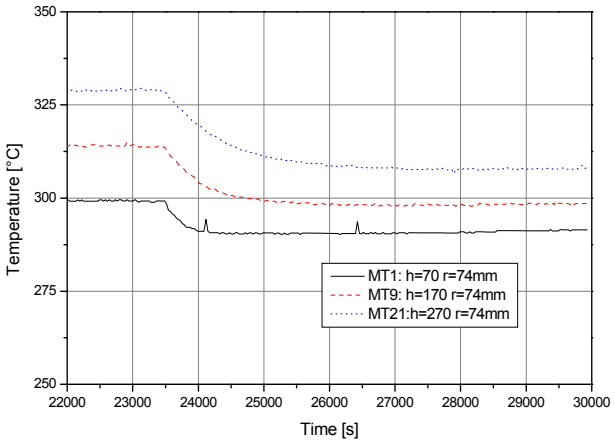

Transition from 18 kW to 10 kW

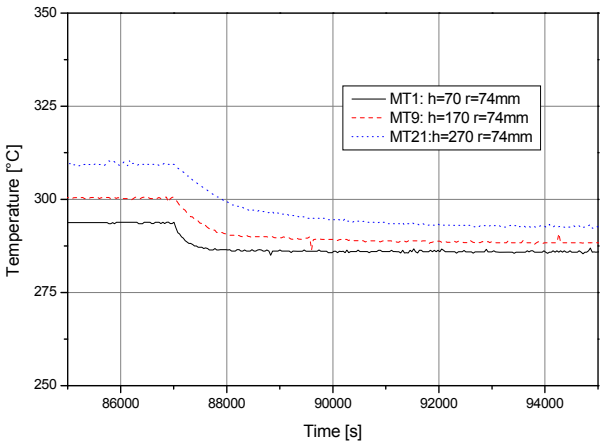

Transition from 10 kW to 5 kW

Figure 14: L4 melt temperature during the transient periods: after melt pouring (top, left), from 18 kW to 10 kW (top, right) and from 10 kW to 5 kW (bottom)

An overview of the melt temperature during the whole test is given in Figure 15. Melt temperature stratification was observed. The considerably low melt temperature at the position of MT5 indicates that the crust grew over at this position. For the two 10 kW heating periods, the temperatures in the melt pool were comparable. The temperature measurements along the azimuths at 90°, 180° and 270° are similar to the temperature measurements along the azimuth at 0° and are shown in Annex B from Figure B- 1 to Figure B- 3.

The melt temperatures at steady state at all positions and the global averaged temperatures of the pool are given in Table 7. The given values are averaged for 1 minute. The global mean temperature is the integration of the weighted local temperature, which are weighted by their occupied volume fraction. Figure 16 shows the melt temperature along vessel height at five heating periods. The slopes of increasing temperature with vessel height became greater with increasing heating power. When the local melt temperature is termed as dimen-

tionless parameter in term of temperature difference between melt local temperature and interface temperature $(T-T_{int})/(T_{mean}-T_{int})$ or $\Delta T/\Delta T_{mean}$, the slopes of $\Delta T/\Delta T_{mean}$ with vessel height were identical of all the heating powers, as shown in Figure 17.

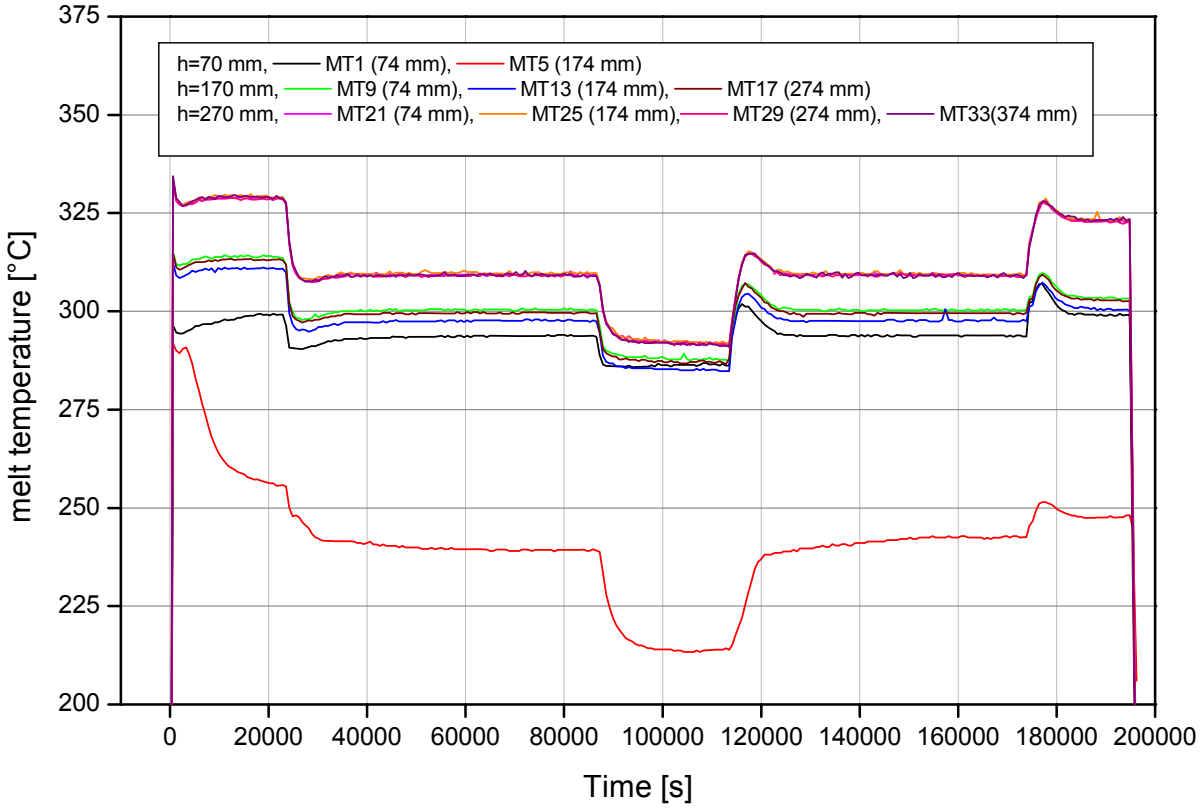

Figure 15: Melt pool temperatures at different elevations along the azimuth 0° in LIVE-L4

The horizontal temperature distribution is also shown in Figure 15 (for different radius) and in Figure 18 (for different azimuth angles). Large asymmetry of temperature distribution is observed at the bottom since some thermocouples at this region measured the temperature of solid crust and the temperature within the crust was very sensible to the crust local thickness. At the middle part of the liquid pool (170 mm vessel height), the maximum temperature difference was within 5 °C at 18 kW. The difference became smaller with decreasing heating power. At the top part of the pool the melt temperature was very homogenous during all heating powers.

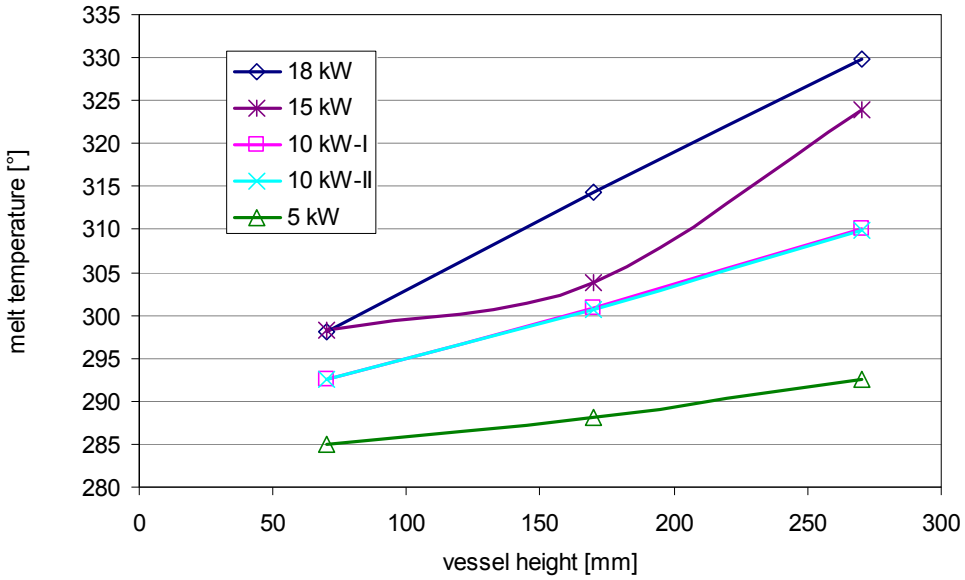

Figure 16: Steady state melt temperature along vessel height at vessel radius 74 during LIVE-L4

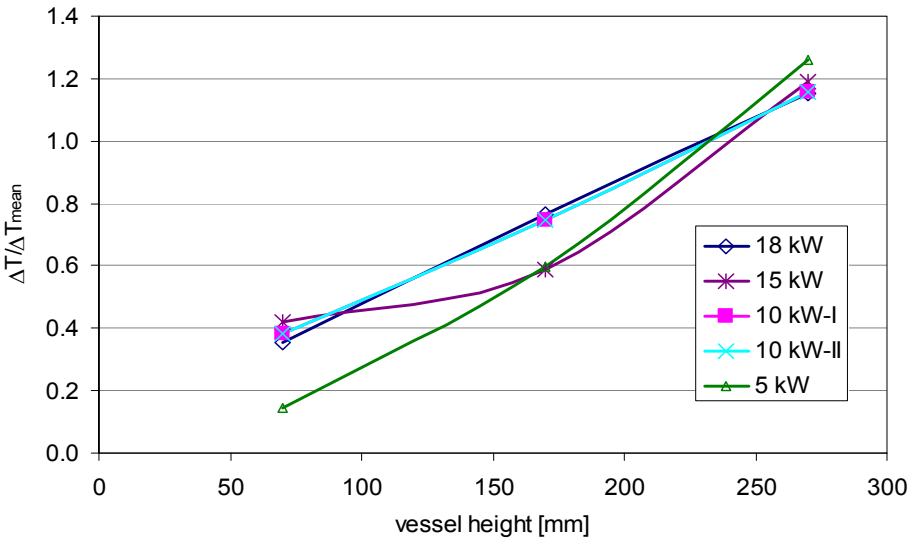

Figure 17: $\Delta T/\Delta T_{mean}$ at vessel radius 74 mm in LIVE-L4

Table 7: 60 s average melt temperature during the the steady state of all test phases

Radius [mm]	Height [mm]	Azimuth angle				
		0°	90°	180°	270°	mean
Test phase 1 18kW, t = 20000 s, Δt = 60 s						
74	70	299.0	296.0	300.8	296.4	298.1
	170	313.9	315.5	311.7	316.2	314.3
	270	329.0	330.7	330.1	329.2	329.8
174	70	256.3	230.9	297.2	257.0	260.4

	170	310.9	312.6	314.1	311.0	312.2
	270	329.4	330.1	329.2	329.9	329.6
274	170	313.1	313.4	312.6	313.5	313.1
	270	328.6	328.8	328.5	329.5	328.8
374	270	329.1	329.8	329.9	328.5	329.3
Global mean $T_{average}$		323.7				
Test phase 2: 10kW-I, t = 80000 s, Δt = 60 s						
74	70	293.7	290.4	294.9	291.4	292.6
	170	300.5	301.6	298.2	302.9	300.8
	270	309.4	311.1	310.5	309.4	310.1
174	70	239.3	207.9	271.0	242.2	240.1
	170	297.7	299.0	300.4	298.0	298.8
	270	309.7	310.6	309.6	310.3	310.0
274	170	299.6	299.9	299.3	300.3	299.8
	270	309.2	309.1	308.9	309.7	309.2
374	270	309.4	310.2	310.2	308.5	309.6
Global mean $T_{average}$		306.5				
Test phase 3: (5 kW), t = 110000 s, Δt = 60 s						
74	70	286.4	282.6	287.3	283.6	285.0
	170	287.5	289.0	285.5	290.1	288.1
	270	291.9	293.8	292.9	291.7	292.6
174	70	213.8	192.3	252.4	213.7	218.1
	170	284.9	286.5	287.7	285.6	286.2
	270	292.3	293.1	292.0	292.7	292.5
274	170	287.2	287.5	286.8	287.8	287.3
	270	291.7	291.7	291.2	292.0	291.7
374	270	291.5	292.8	293.1	291.3	292.2
Global mean $T_{average}$		290.8				
Test phase 4: 10kW-II, t = 160000 s, Δt = 60 s						
74	70	293.8	290.4	295.1	291.0	292.6
	170	300.3	301.6	298.2	302.6	300.7
	270	309.2	310.9	310.4	309.2	309.9
174	70	242.5	212.4	270.4	243.3	242.1
	170	297.6	299.0	300.3	298.1	298.7
	270	309.4	310.4	309.5	310.3	309.9
274	170	299.5	299.8	299.2	300.1	299.7

	270	309.2	309.2	308.9	309.6	309.2
374	270	309.1	310.2	310.1	308.2	309.4
Global mean $T_{average}$		306.4				
Test phase 5: 15.4 kW, t = 190000 s, Δt = 60 s						
74	70	299.2	295.7	300.9	296.9	298.2
	170	303.4	304.6	301.2	306.0	303.8
	270	323.0	324.8	324.6	323.4	324.0
174	70	247.6	232.3	295.2	248.0	255.8
	170	300.6	302.1	303.2	301.5	301.9
	270	323.4	324.2	323.5	324.3	323.8
274	170	302.8	303.1	302.3	303.6	303.0
	270	322.8	323.1	322.9	323.9	323.2
374	270	323.3	324.1	324.3	323.0	323.7
Global mean $T_{average}$		317.6				

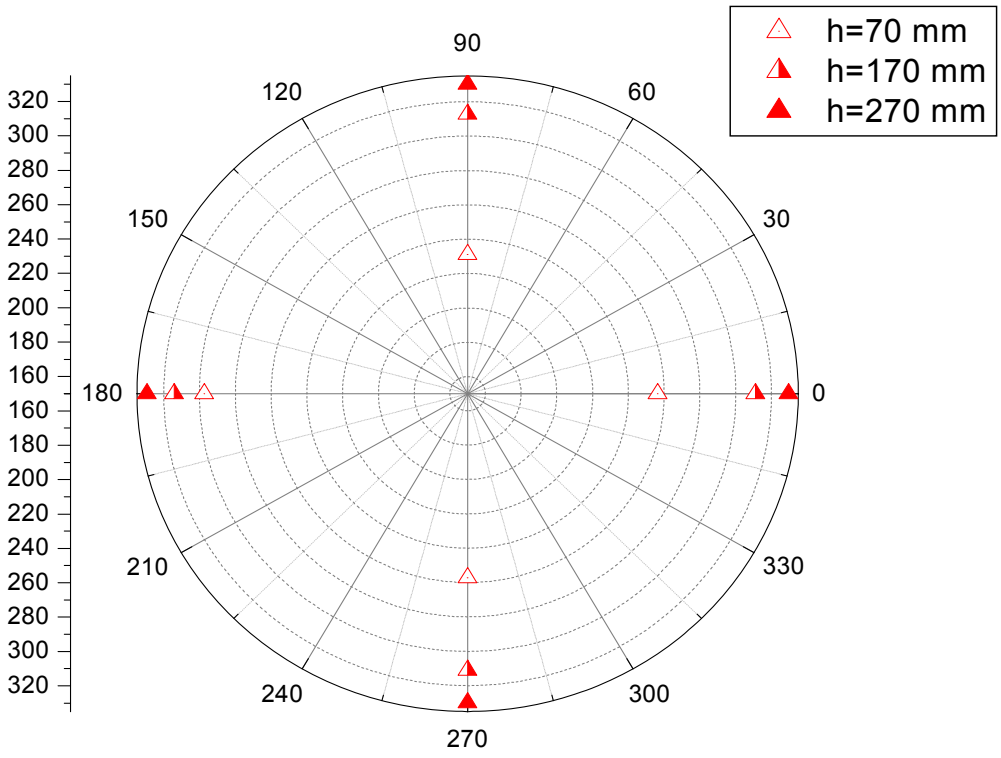

Figure 18: Melt temperature distribution along azimuth angle at radius 174 mm at 18 kW

4.3.2 Melt pool vertical profiles measured by crust detection lance

The crust detection system can measure the vertical melt pool temperature profile, the crust thickness and the melt/crust boundary temperature, as shown in Figure 19.

The measurements with the crust detection lance were performed during the steady state phases of 10 kW-II, 5 kW and 15 kW. The crust thicknesses at polar angle 47° during 10 kW, 5 kW and 15 kW were 45.3 mm, 25.8 mm and 18 mm respectively. The vertical temperature profiles are shown in Figure 20. A temperature boundary layer with 4-5 mm thickness was detected at the melt/crust interface.

The lowest melt/crust interface temperature was measured during the 5 kW heating power, the lowest heating power in the test. Since the interface temperature during the steady state phase is the liquidus temperature of the melt, which is subject to the melt composition, the decrease of the interface temperature in low power generation indicates that the liquid melt was depleted in KNO_3 as the KNO_3-enriched crust grew.

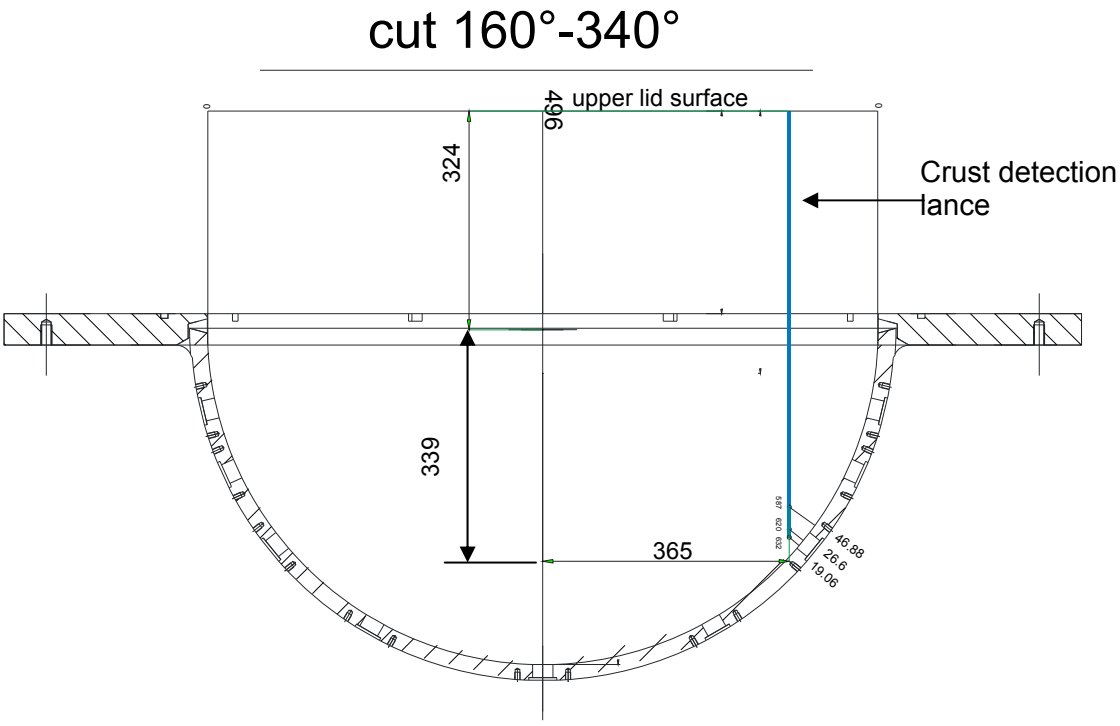

Figure 19: Position of the crust detection lance used for crust thickness and vertical temperature profile measurements

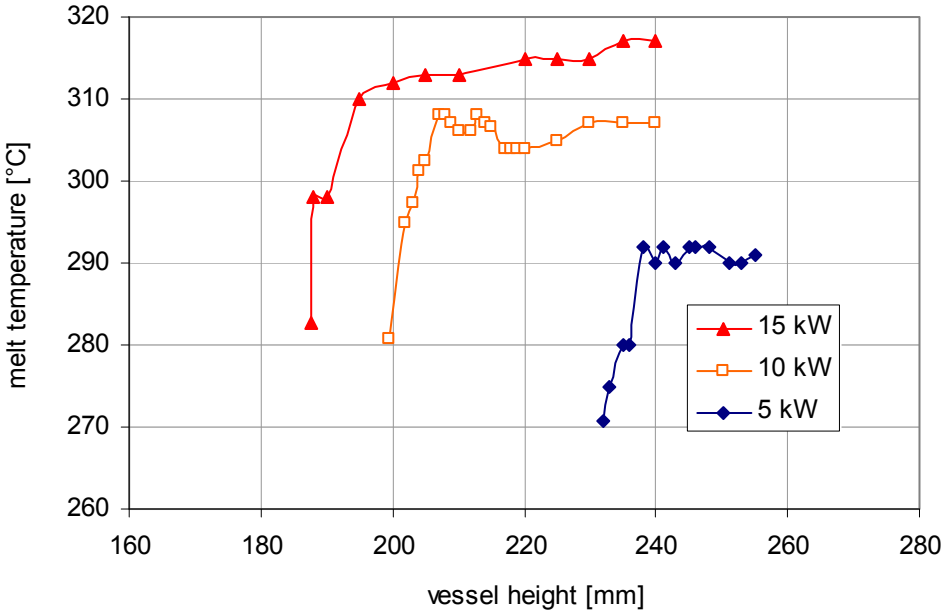

Figure 20: Melt temperature profiles measured by crurst detection lance at radius 365 mm

4.4 Heat flux and heat balance in LIVE-L4

The heat flux through the vessel wall can be calculated based on the temperature difference between the inner and outer surface of the test vessel wall. The heat flux q through a plane wall is given by:

$$q_{pla} = -k \cdot (T_o - T_i)/L \qquad (1)$$

where

q_{pla}: heat flux, W/m^2,

k: thermal conductivity of the wall, [W/(m·K)]

T_o: outer wall temperature (measured by OT thermocouples), [K]

T_i: inner wall temperature (measured by IT thermocouples), [K]

L : wall thickness, [m]

To calculate the heat flux through a spherical wall, q_{sph}, as in the case of the LIVE test vessel, the heat flux expressed in the Eq (2) should be corrected accordingly. Assuming the inside area of a spherical wall is the same as that of a plane wall, and the spherical wall also has the same thickness as the plane wall one can obtain:

$$q_{sph} = q_{pla} \cdot (R_i / R_o) \qquad (2)$$

where

Ri: inner spherical wall radius, m,

Ro: outer spherical wall radius, m.

Wall inner surface temperature (IT) and outer surface temperature (OT) at 17 positions were measured during the L4 test at five levels, their steady state values are given in Table 11. Five heat flux zones are defined on the test vessel wall surface according to the 5 levels, as shown in Figure 21. Each zone has its own local heat flux and surface area. The boundary between each zone under the melt surface is the middle position of two levels of IT and OT thermocouples. The upper boundary of zone 5 is the melt surface. The geometric data of the zones are given in Table 8.

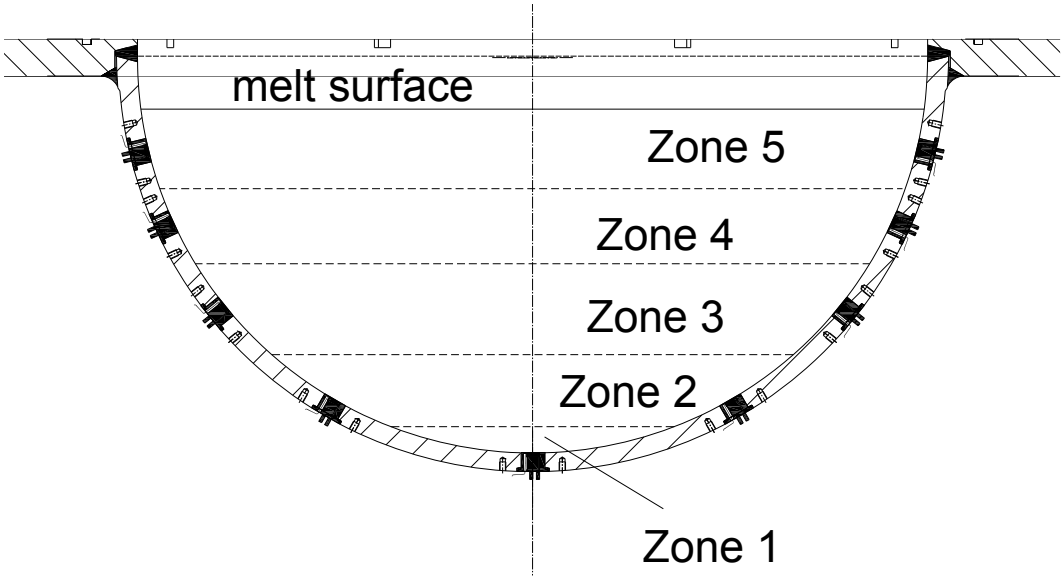

Figure 21: Definition of heat flux zones on the test vessel wall surface

Table 8: Geometries of the heat flux zones

	IT/OT Nr.	**Zone upper surface to bottom [mm]**	**Height of zone [mm]**	**Zone inner surface area A_i [m²]**
Zone 1	1	32.5	32.5	0.1014
Zone 2	2-5	124	91.5	0.2855
Zone 3	6-9	236.5	112.5	0.3510
Zone 4	10-13	335	98.5	0.3073
Zone 5	14-17	431.6	96.6	0.3015

The test vessel wall thickness is measured at the local positions of IT/OT thermocouples. The groove depth for the IT thermocouples is 0.5 mm, and that for the OT thermocouples is 1 mm. Therefore the half of the total groove depth should be deducted from the wall thickness. In Table 9 the real wall thickness at the positions of IT/OT thermocouples is given. The correction factor "*Ri/Ro"* for the five horizontal heat flux zones is also given in Table 9.

Table 9: Heat flux form correction factor for spherical form and wall thickness

	Zone 1	**Zone 2**	**Zone 3**	**Zone 4**	**Zone 5**
Thermocouple	IT1/OT1	IT/OT2-5	IT/OT6-9	IT/OT10-13	IT/OT14-17
Vertical angle [°]	0	30	51	65.5	76.5
Ri/Ro	0.957	0.956	0.956	0.956	0.955
Wall thickness [mm]	23.3	23.5	23.63	23.76	23.9

The test vessel is made of stainless steel AISI316Ti, the material number is X6CrNiMoTi17-12-2. The thermal conductivity of this material is taken from [13] and is shown in Table 10.

Table 10: Heat conductivity of AISI316Ti

Temperature [K]	**300**	**400**	**600**
Heat conductivity [W/(mK)]	13.4	15.2	18.3

Since the working temperature of the test vessel during L4 test was between 300 K and 400 K, following equation can be obtained from the data in Table 10. The temperatures are given in K.

$$k(T) = 13.4 + 0.018 \cdot (T - 300) \tag{3}$$

Table 11: Test vessel wall inner temperatures and outer temperatures during L4 test

	IT				OT			
	azimuth angle [°]				azimuth angle			
polar angle	22.5	112.5	202.5	292.5	22.5	112.5	202.5	292.5
	18 kW 20000 s							
0.0		24.2				17.6		
30.0	23.1	20.4	24.6	22.1	18.4	18.0	18.7	18.2
51.0	40.1	42.1	41.7	45.2	24.9	25.8	28.1	27.7
65.5	**93.8**[1]	65.6	74.7	62.5	32.8	38.5	40.8	39.8
76.5	75.3	78.6	80.3	75.1	41.6	44.6	47.3	46.9
	10kW-I 80000 s							
0.0		23.7				17.1		

30.0	20.1	18.0	22.0	19.2	17.3	17.3	17.7	17.4
51.0	27.3	28.6	28.7	31.2	20.6	21.1	22.6	23.4
65.5	**65.6**[1]	43.8	48.4	41.6	25.8	28.8	31.2	30.5
76.5	46.2	52.2	55.0	49.5	30.8	33.3	36.4	35.7
	5 kW 110000 s							
0.0		22.4				16.3		
30.0	19.2	17.0	19.9	19.8	16.4	16.3	16.6	16.9
51.0	20.6	19.5	22.1	25.7	17.7	17.5	19.1	20.9
65.5	**41.1**[1]	25.3	26.7	25.8	19.4	20.5	21.9	22.1
76.5	25.6	28.0	28.9	28.7	21.1	22.1	23.6	23.8
	10 kW-II 160000s							
0.0		24.3				16.8		
30.0	20.6	18.6	21.3	19.8	17.2	16.9	17.3	17.0
51.0	27.4	27.7	29.2	29.0	19.9	20.8	22.8	22.1
65.5	**79.7**[1]	40.0	45.1	41.2	25.0	28.1	30.7	28.8
76.5	44.9	53.8	53.1	50.1	30.3	33.4	35.8	35.5
	15 kW 190000s							
0.0		25.3				16.4		
30.0	21.3	18.3	21.7	20.2	16.9	16.9	17.4	17.0
51.0	35.9	32.8	35.9	35.7	22.1	22.7	24.7	24.3
65.5	**154.6**[1]	58.0	60.9	59.4	31.0	33.8	38.3	36.9
76.5	64.5	75.3	72.2	69.2	39.3	41.4	44.4	44.3

Note: [1]: the IT thermocouple at this position was detached from the vessel wall, therefore the measured values were not reliable.

The accuracy of the IT measurement direct influences the heat flux calculation. The system error of the device and the transmission are ±1.5 °C and ±0.5%. The difference of the system error of a pair of IT and OT, which directly influences the accuracy of local heat flux calculation, was calibrated based on a pre-test measurement in an isothermal environment. Nevertheless, moderate deviation and error of the local heat flux still exist due to the small difference between IT and OT temperature, as shown in Table D- 1.

The IT and OT temperatures during the whole test period are also shown in Annex B, Figure B- 4 to Figure B- 11. It is found that the thermocouple IT10 (at polar angle 65.5° and azimuth angle 22.5°) gave unreliable value. Probably the thermocouple was detached from the wall

during crust formation and measured the temperature of local crust of gap. The unusual high value of IT10 is shown in Figure B- 6. Therefore the heat flux value at IT10 is not calculated.

It is observed that there were several sharp increasing pulses of IT temperatures at the middle and lower part of the wall during the heating period of 5 kW. These events could be the result of crust cracking and the penetration of hot melt through the crust. The crust cracking was probably resulted by the stress release during growing or melting of the crust.

The heat flux distributions during the five steady state phases are given in Table 12. The heat flux level mean values and global mean values are also given in the table. The heat flux along the polar angle at five heating periods is shown in Figure 22. Large uncertainties could exist in the heat flux level mean value, which is affected by the measuring uncertainty of local IT as well as by the asymmetry of horizontal heat flux distribution. Especially large deviation was calculated at level 2, polar angle 30° (Table D- 1). In addition, at the vessel bottom the heat flux could be overestimated due to local heat dissipation from the lowest level of the heating element, which is located near the vessel bottom. Increasing heat generation rate in the melt pool led to the intensification of heat transfer at the upper part of vessel. However when the local heat flux is normalized with the global mean heat flux, described as q/q_{mean}, the normalized value at the vessel upper part was comparable among different power densities, as shown in Figure 23. The maximum value of q/q_{mean} is about 1.7.

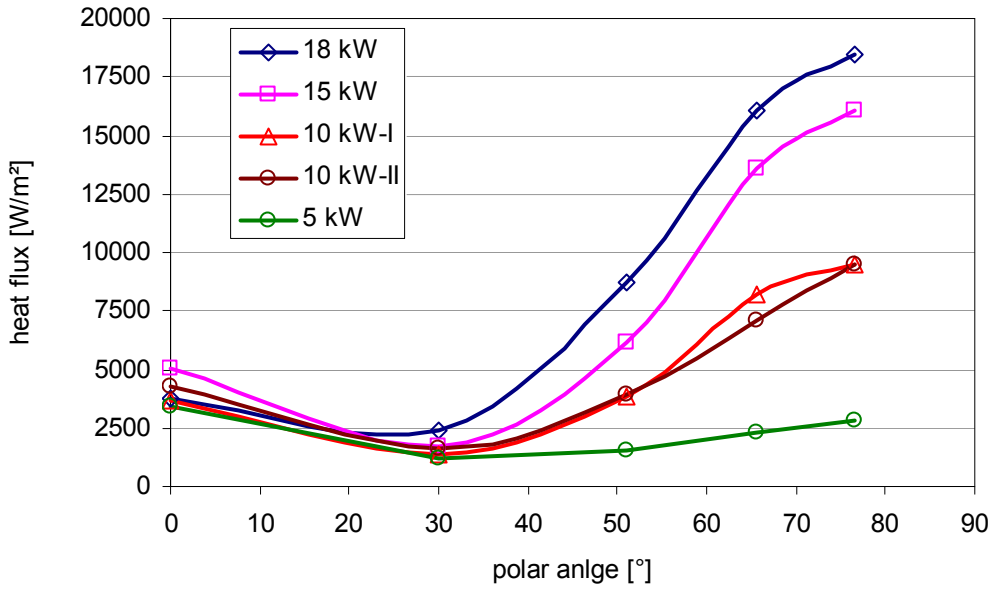

Figure 22: Heat flux along the vessel polar angle in LIVE-L4

Table 12: Calculated heat fluxes during steady states in LIVE-L4 test, W/m^2

Heating period	Polar angle	Azimuth angle				Level mean value	Global mean value
		22.5°	112.5°	202.5°	292.5°		
18 kW 20180s	0	3748	3748	3748	3748	3748	10759
	30	2682	1319	3278	2183	2366	
	51	8745	9277	7280	9568	8718	
	65.5		15771	19310	13011	16031	
	76.5	19307	19487	19012	16132	18485	
10 kW-I 80190s	0	3637	3637	3637	3637	3637	5528
	30	1497	491	2399	1053	1360	
	51	3760	4150	3176	4415	3875	
	65.5		8460	9722	6513	8232	
	76.5	8749	10440	10589	8054	9458	
5 kW 112314s	0	3437	3437	3437	3437	3437	2073
	30	1536	413	1838	1071	1215	
	51	1492	1005	1585	1991	1518	
	65.5		2533	2620	1889	2347	
	76.5	2568	3342	2812	2595	2829	
10 kW-II 160133s	0	4264	4264	4264	4264	4264	5403
	30	1910	922	2122	1492	1612	
	51	4192	3915	3739	3815	3915	
	65.5		6657	8023	6661	7114	
	76.5	8170	11588	9828	8333	9480	
15 kW 184496s	0	5039	5039	5039	5039	5039	9072
	30	2251	636	2235	1743	1716	
	51	7648	5357	5593	6072	6168	
	65.5		13403	13414	14073	13630	
	76.5	14508	19271	16085	14524	16097	

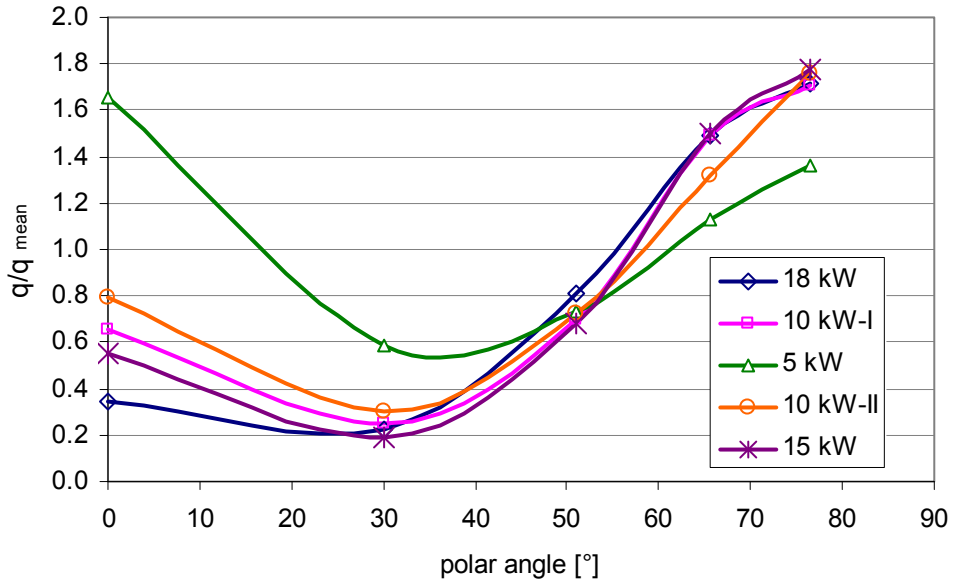

Figure 23: q/q_{mean} along vessel polar angle in LIVE-L4

The transient heat fluxes after melt pouring are shown in Figure 24. The heat flux reached its maximum during the period of melt pouring. The maximum heat flux has reached 43 kW/m² at the position of IT12, which was 3.5 times of its steady state value during 18 kW. The heat flux decreased to ~20 kW/m² in 200 s and then decreased slowly further to steady state values.

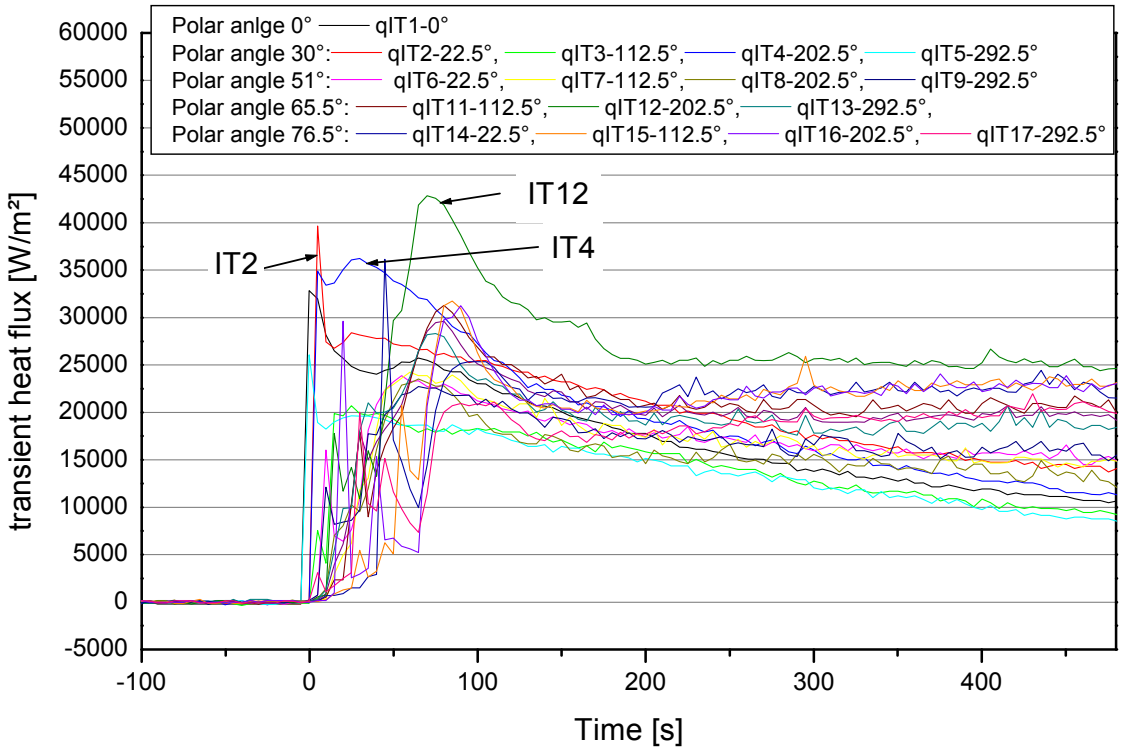

Figure 24: Transient heat flux during and after melt pouring in LIVE-L4

In the following the heat balance among the heat generation, heat through the vessel wall and heat removal by cooling water is analysed. The heat balance gives implications of the effectiveness of the external cooling for different power densities.

In the LIVE test facility the heat through the vessel wall is removed by water which flows from the bottom to the top opening of the cooling vessel. The heat through the test vessel wall under the melt surface can be calculated from the heat flux estimation, and the heat removed by water (Q_{water}) can be calculated based on the water inlet and outlet temperature and the water flow rate. The aim of the heat balance calculation in this test is a) to determine the Q_{wall} for different heat generation levels and b) to check the reliability of the measurements in the LIVE facility by comparing Q_{wall} with Q_{water}.

The total heat transfer through the vessel wall Q_{wall} is determined by summing up the local heat flux multiplied by the corresponding surface area of the vessel wall. The heat flux of each zone was calculated in section 2.4 and the corresponding surface areas are shown in Table 8.

$$Q_{wall} = \sum q_i \cdot A_i \tag{4}$$

where

q_i: local heat flux, W/m^2,

A_i: surface area of the of the corresponding local heat flux zone, m^2.

The heat removed by cooling water (Q_{water}) is calculated according to (5):

$$Q_{water} = c_p \cdot f_w \cdot (T_{out} - T_{in}) \tag{5}$$

where

c_p: specific heat capacity of water, 4.193 J/gK at 10 °C,

f_w: water mass flow rate, g/s,

T_{out}: outlet temperature of the cooling water, K

T_{in}:inlet temperature of the cooling water, K

To calculate Q_{water}, the water inlet T_{in} and outlet T_{out} temperatures were measured during the test. It was found out that the measuring value of the inlet and outlet temperature slightly deviate from the real values in the working temperature range. After the calibration of these two thermocouples with a PT100 thermometer, Eq(6) and Eq(7) are obtained to correct the system errors of the water inlet and outlet thermocouples. The water inlet and outlet temperature after correction are shown in Figure 12.

$$T_{in}^{real} = -0.3389 + 1.0089 \cdot T_{in}^{measured} \tag{6}$$

$$T_{out}^{real} = 0.1419 + 0.9518 \cdot T_{out}^{measured} \tag{7}$$

The heat balance including heating power, calculated Q_{wall} and Q_{water} are shown in Figure 25. Good agreement was observed between Q_{wall} and Q_{water}, which proves the correctness of the measured parameters for the calculation. The portion of heat transfer through the vessel wall under the melt surface amounted from 80 % during 18 kW to about 56 % during 5 kW. This implies that more fraction of heat can be transferred through vessel wall in high heating power. The high value of Q_{wall} is a result of the good insulation of the vessel upper lid.

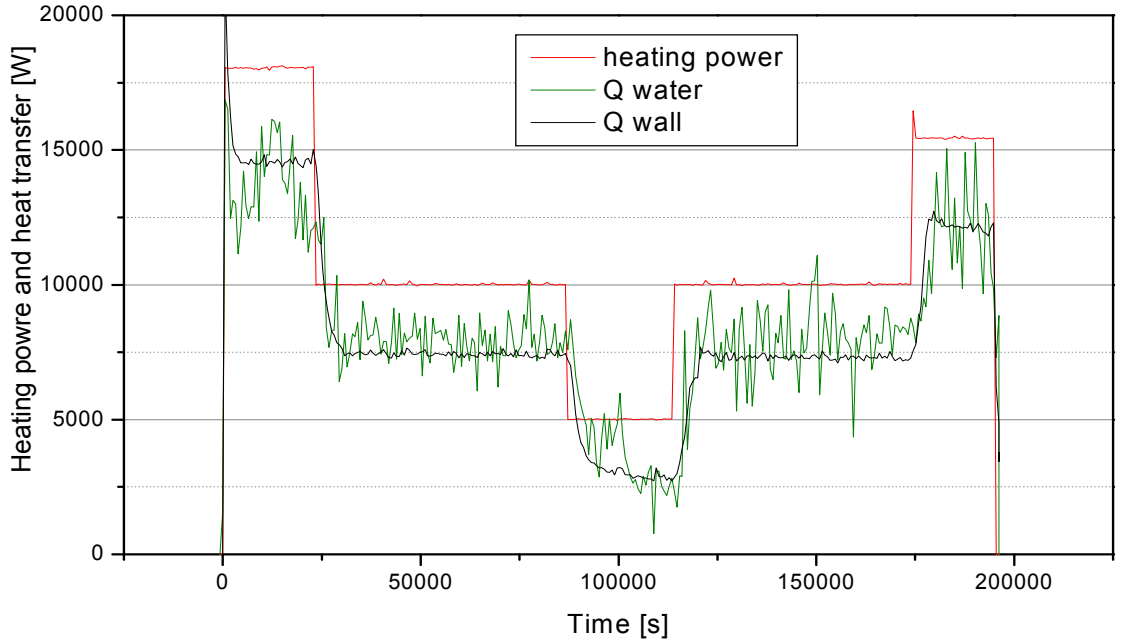

Figure 25: Heat balance between heating power, heat through vessel wall and heat removed by cooling water in LIVE-L4

The internal Ra_i and Nu_{dn} numbers during the five heat generation rate are also calculated according Eq (8) and Eq (9) respectively. The height of the melt pool was used as the characteristic length in Nu and Ra calculation In Table 13 the Nu_{dn}, Ra_i and some other important heat transfer parameters in the test are given.

$$Ra_i = g.\beta \cdot q_i \cdot L^5 /(\nu \cdot \alpha \cdot \lambda) \quad (8)$$

$$Nu_{dn} = q_{mean} \cdot L /(\lambda \cdot (T_{\max} - T_{\text{int}}) \quad (9)$$

Where:

β: thermal expansion coefficient, [1/K], 3.81E-04

α: thermal diffusivity, [m²/s], 1.69E-07

λ: themal conductivity, [W/(m·K)], 0.439

ν: kinematic viscosity, [m²/s], value in Table 13

T_{max}: pool maximum temperature, [°C], value in Table 13

T_{int}: melt temperature at melt/crust interface,[°C], is the liquidus temperature, 284 °C,

q_{mean}: mean heat flux through vessel wall, [W/m²], value in Table 13

q_i: heat density, [W/m³], value in Table 13.

Table 13: Nu, Ra and some important heat transfer parameters in LIVE-L4

heating power, kW	**18**	**10**	**5**	**10**	**15**
T_{mean}, °C	323.7	306.5	290.8	306.4	317.6
T_{max}, °C	329.9	310	292.3	310	324.5
T_{int}, °C	-	-	270.8[1]	280.0[1]	281.2[1]
$Q_{heating}$, W	18064.2	10014.1	5014.7	10014.0	15445.4
Q_{wall}, W	14488.7	7444.5	2792.1	7275.9	12216.0
$Q_{wall}/Q_{heating}$, -	0.802	0.743	0.557	0.727	0.791
Heat density, W/m³	87692	48613	24344	48613	74979
$q_{dn\ mean}$, W/m²	10759	5528	2729	5403	9072
ν, m²/s	1.56E-06	1.70E-06	1.82E-06	1.70E-06	1.61E-06
Pr	9.3	10.1	10.8	10.1	9.6
Nu and Ra, L=vessel height					
Nu_{dn}	-	-	99.3	179	208
Ra_i	4.31E+13	2.17E+13	9.99E+12	2.17E+13	3.56E+13

[1]: measurement data from the crust detection lance.

4.5 Post tests analysis of LIVE-L4

As mentioned in chapter 4.1, about 387 kg of nitrate melt, corresponding to 207 l, was poured into the test vessel at the beginning of the test. The height of the melt was 431 mm. At the end of the test, 341 kg of melt was extracted back into the heating furnace. Thus, the mass of the crust formed on the vessel wall at the end of the test is 46 kg, which corresponds to 11.9 % of the total melt mass in the test vessel.

4.5.1 Average composition of the melt in LIVE-L4

The original melt composition and the melt composition at the end of test were analysed. The original melt sample was taken from the remaining in the pouring spout and the melt sample at the end of the test was taken with a steel rod intruding in the melt. The melt solidified on the cold surface of the rod was used for the composition analysis. The samples were dissolved in water and the composition analysis was performed by determining the content of Na and K cations in the aqueous solution. The composition of the melt and the corresponding melt liquidus temperature are given in the Table 14. The KNO_3 concentration in the original melt was 79.5 mole%. It became slightly lower at the end of the test.

Table 14: Composition of the melt pool

	Original sample	End of test Measurement 1	End of test Measurement 2
K [w/o]	29.377	30.381	31.468
Na [w/o]	4.449	4.668	4.800
Na/K [w/w]	0.15146	0.15366	0.15254
K [mol-%]	79.518	79.281	79.402
Na [mol-%]	20.482	20.719	20.598
Na/K [mol/mol]	0.25757	0.26133	0.2594
KNO_3 [w/o]	82.203	81.990	82.098
$NaNO_3$ [w/o]	17.797	18.010	17.902

4.5.2 Crust growth characters, crust thickness and crust thermal conductivity

A view of a segment of the test vessel after removing the top lid of the vessel is shown in Figure 26. The crust formed during the test at the vessel wall of this vessel segment can be clearly seen. The thickness of the crust was measured along the azimuth sections 67.5°-247.5° and 157.5°-337.5°. Crust samples have been taken for the analysis of crust liquidus temperature and composition.

Figure 26: View of a segment of the test vessel after disassembly of the lid in LIVE-L4

Some important parameters related to the melt solidification process can be determined with crust temperatures measured by the crust thermocouple trees (Figure A- 8). The detailed description of the thermocouple trees is given in section 2.4. The times at which the crust front arrived at a thermocouple location can be determined based on the changing slope of the crust temperature due to the phase change. The crust growth parameters include crust thickness development with time, crust growth rate, temperature gradient in the crust and the time period of crust growth. Based on these parameters the melt solidification condition can be determined.

The temperatures of the thermocouple trees are shown in Figure B- 12 to Figure B- 14. Based on the crust temperature measurements the crust thickness progression after melt pouring is calculated[14]. Table 15 givens the crust thickness z, crust growth rate R and crust temperature gradient G at the position of CT2, polar angle 52.9°. The crust thickness development is illustrated in Figure 27. There are some uncertainties of the crust thickness evaluation during the time period of 1500 s to 2000 s. The uncertainty originates from how a pair of neighbouring thermocouples in the thermocouple tree is selected. When both the two thermocouples were in the crust, the crust thickness was underestimated; when one thermocouple was in the crust and the other in the melt, the crust thickness was overestimated. These two methods results in the minimum and maximum boundary of crust thickness estimation which are shown in Table 15 as the z_{min} and z_{max}. For the calculation of crust growth rate the minimum crust thickness the Z_{min} was used.

Table 15: Crust thickness, growth rate and temperature gradient after melt pouring at polar angle 52.9°

Time	Crust thickness, low Z_{min}, mm	Crust thickness, high z_{max}, mm	Crust growth rate R, µm/s	Temperature gradient G_{min}, °C/mm	G/R
80	1.93	1.93	8.99	44.27	4924
100	2.11	2.11	8.93	49.36	5528
180	2.82	2.82	2.14	44.59	20863
400	3.29	3.29	1.52	38.31	25259
1001	4.21	4.21	1.19	30.92	25964
1502	4.80	5.53	0.41	27.42	66415
1602	4.84	5.58	0.80	27.18	34184
1752	4.96	5.75	0.18	26.45	147912
1802	4.97	5.74	0.59	26.33	44408
1900	5.03	5.83	0.32	26.10	80916
2000	5.06	5.88	1.15	18.78	16366

3000	6.21	6.21	0.36	18.46	50876
3500	6.39	6.39	-0.01	17.87	-1423355
4000[1]	6.38	6.38	0.25	18.11	**71412**
4500	6.51	6.51	0.14	17.77	125810
5002	6.58	6.58	0.04	17.41	440004
5998	6.62	6.62			

Note: [1]: End of the constitutional supercooling condition.

The time period from melt pouring to the end of crust growth at the polar angle positions of 37.6°, 52.9° and 66.9° were 133 min, 100 min and 3 min respectively. According to the criterion of constitutional supercooling condition described in the L3A report [15], the time period of the constitutional supercooling at 52.9°, in which mush zone existed, was about 4000 s or 66 min.

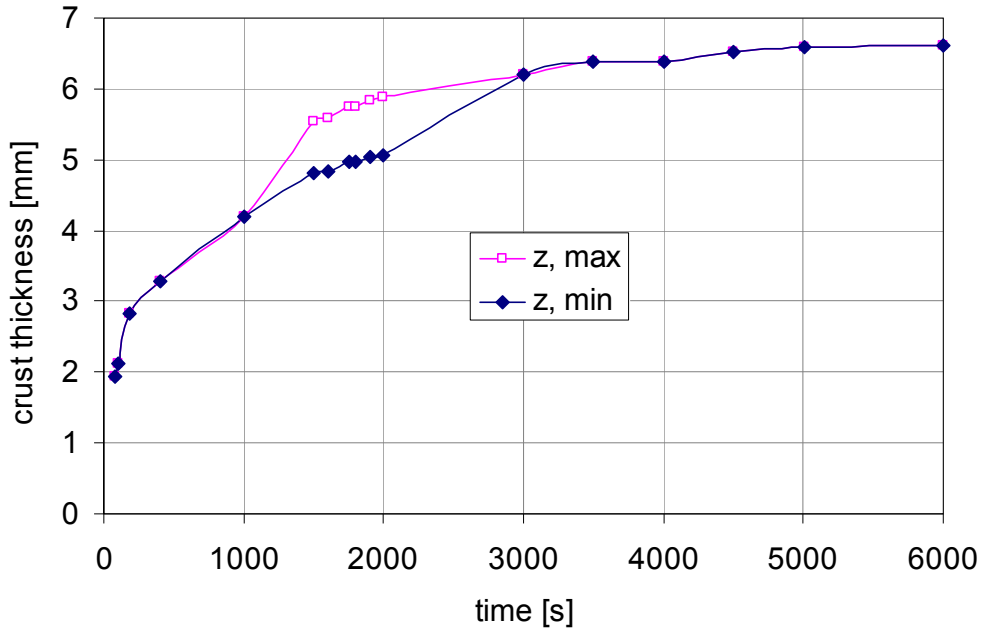

Figure 27: Crust thickness development after melt pouring at polar angle 52.9° in LIVE-L4

Figure 28 shows the crust thickness estimation during the test period. The result in LIVE-L4 implies that the crust thickness can be different for same power density but different heating history. Prompt increase of crust thickness occurred several times during the 5 kW heating period, as shown in Figure 29. These events were especially significant at the middle and the upper vessel wall (at 200mm and 300mm vessel height), as shown in Figure B- 13 and Figure B- 14. A possible explanation is hot melt penetration to the gap at the crust/wall interface as a result of crust cracking. Two facts support this explanation: a) the sudden arise of crust temperature before the improvement of cooling was evidence that the hot melt reached

the gap between the crust and wall; b) the cooling improvement took place firstly at the interface.

Such events occur most possibly during low power generation rate in which the crust became thick. The final crust thickness increased after these events to compensate the original thermal resistance. The gap formation between the crust and the test vessel implies also that the crust temperature at the wall was not the vessel wall inner surface temperature. The difference of these two temperatures was about 75 °C to 125 °C in this test. Without the gap formation the crust thickness should be thicker than the measured value.

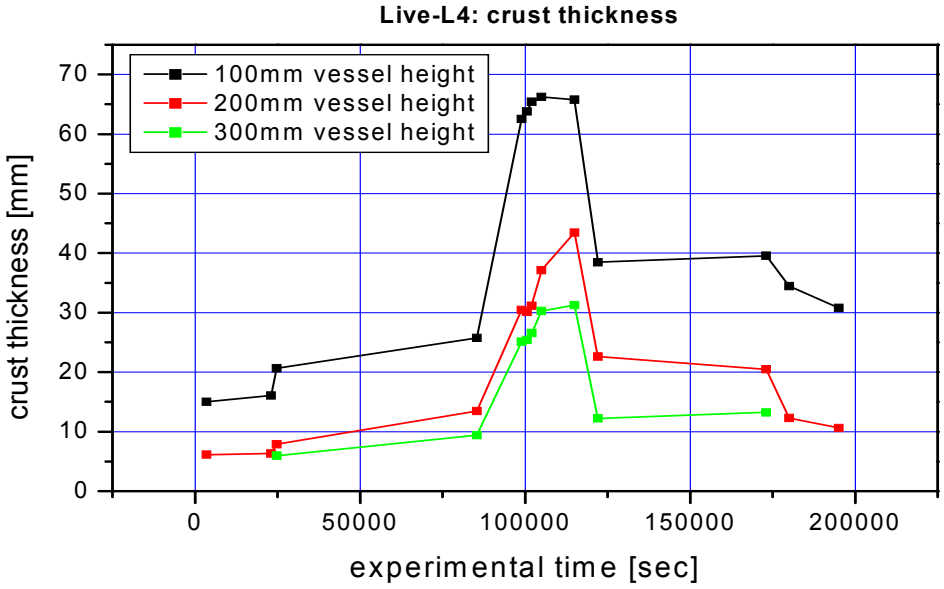

Figure 28: Crust thickness estimation based on CT measurements during LIVE-L4 test

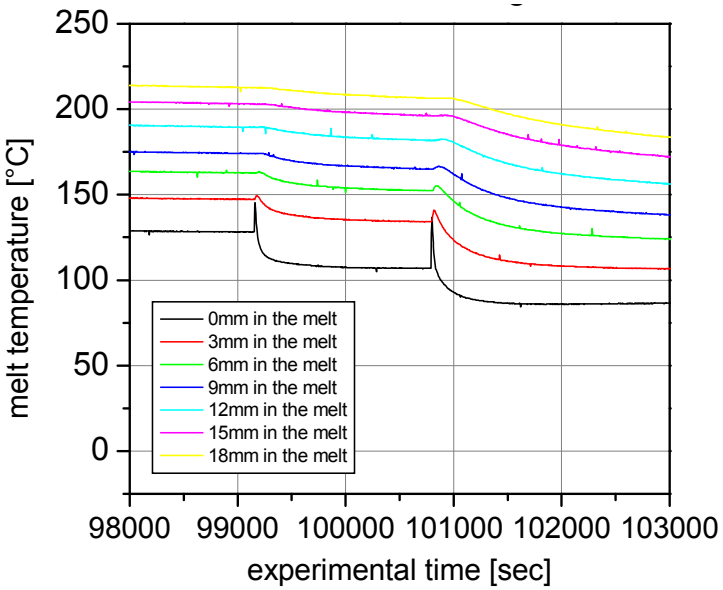

Figure 29: Prompt improvement of cooling at the wall/crust interface during the 5 kW period

The final crust thickness during the 15 kW heating period was shown in Figure 30. The crust grew horizontal symmetrically at the upper part of the vessel and was somewhat influenced by the local heating wires at the lower part and at the bottom of the wall.

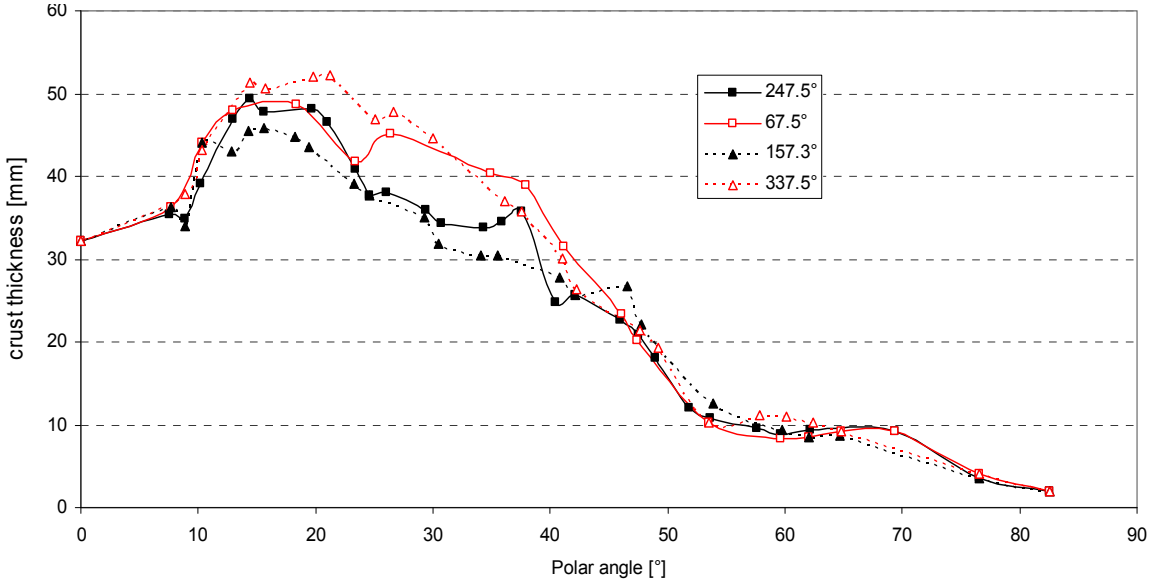

Figure 30: The final crust thickness in four azimuth angles after L4 test

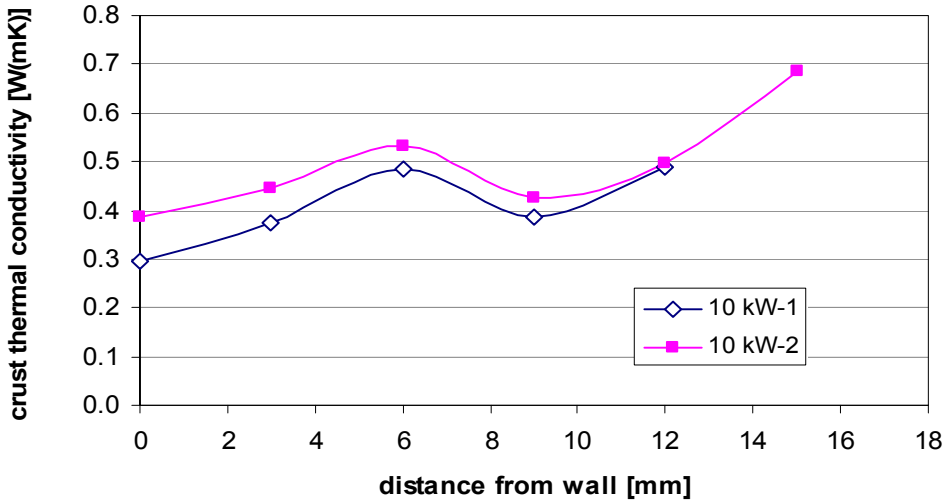

Figure 31: Crust thermal conductivity at 52.9° during 10 kW-1 and 10 kW-2 heating periods

The crust thermal conductivities during the steady states of 10 kW-I and 10 kW-2 periods at CT2 (52.9°) are shown in Figure 31. Two facts can be observed in this diagram: a melting crust has higher thermal conductivity than a growing crust; and the crust near melt has higher thermal conductivity than the crust near vessel wall. The crust in the 10 kW-2 period was the remaining of a partially molten crust, and it had higher thermal conductivity than the crust with a growing history, such as in 10kW-I period. The high conductivity of the remaining of a molten crust could be explained that the original porous structure and the composition in

the crust mushy zone was refined during melting process ([17]-[18]). The high thermal conductivity near the crust front is probably related with the crust growing rate. A slowly growing crust is expected to have high conductivity.

4.5.3 Crust liquidus temperature and crust composition in LIVE-L4

The liquidus temperature of a 20 mm thick crust layer was analysed with “Optimelt”, a melting temperature analyse device which detects the image change in three powder-loaded capillary tubes during controlled heat up period. Sampling materials was grounded and well mixed before loaded to the capillary tubes. The difference of the results between the heating-up method and the cool-down method is within 4 degrees. Eight locations across the crust layer in 3 mm distance between each other were analysed. Figure 32 shows the crust liquidus temperature from wall to crust/melt interface. Generally the liquidus temperature of a growing crust reaches its highest point at the at the end its growth. The decreasing value from 11 mm to 15 mm away from vessel wall implies that a second phase of fast growth took place when the heating power was reduced from 18 kW to 10 kW. There was still a third phase of crust fast growth when the power was reduced from 10 kW to 5 kW. However this part of the crust was molten again as the heating power increased from 5 kW to 10 kW and then further to 15 kW. The average composition of the crust at this position is 303.3 °C, corresponding to a crust composition of 87 mole % KNO_3.

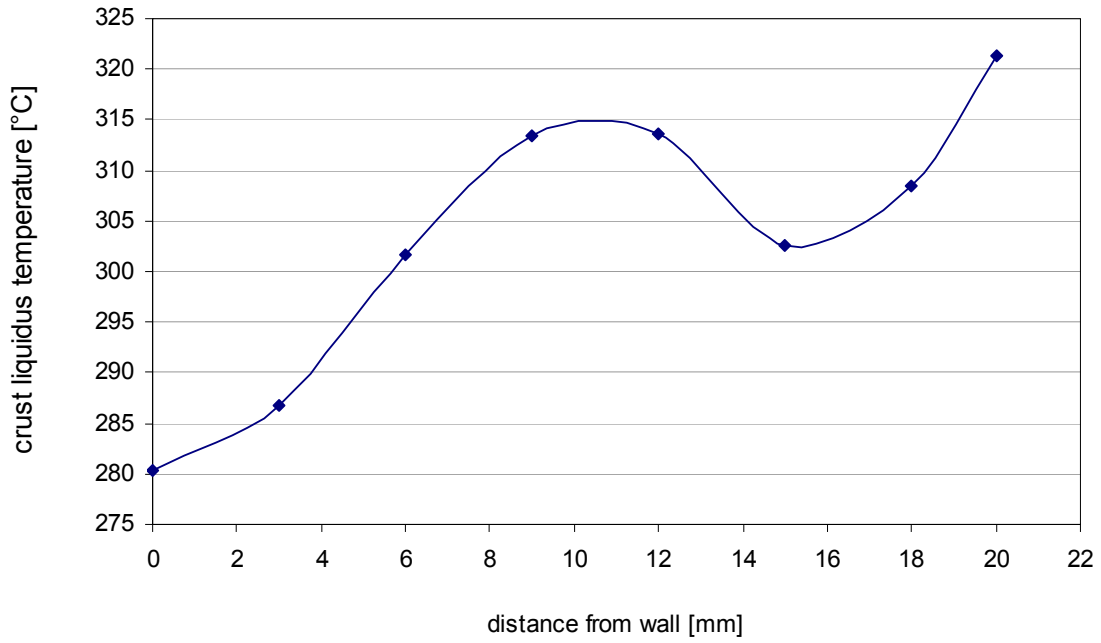

Figure 32: Liquidus temperature of a 20 mm-thick crust layer taken from L4 test

5 Preparation and test condition of LIVE-L5L

The experiment LIVE-L5L was successfully conducted on December 01-04 2008. The preparation of the test was similar to L4 test. The remaining salt in the heating furnace was 345 kg. 38.8 kg KNO_3 and 8.16 kg $NaNO_3$ new salts were filled in the furnace to obtain a total amount of 392 kg with the composition of 80 mole % KNO_3 and 20 mole % $NaNO_3$. The melt was heated to 350°C before pouring in the furnace. Two melt pours were performed: 120 l melt was poured firstly and was heated with 10 kW; the other pouring of 90 l melt was conducted when the melt pool reached its thermal hydraulically steady state after the first pouring, and the total heating power increased to 18 kW. The pouring position of the two pours was central. The total amount of melt after the second pouring 210 l corresponds to 100 % of the core inventory. Then the test plan was the same as in L4, in which the heating phases went through 18 kW-I, 10 kW-I, 5 kW, 10 kW-II and 18 kW-II. The cooling vessel was filled with water before test. External water cooling with the flow rate of 1.3 kg started before the first pouring, so that the test vessel wall outer surface was in a quasi isothermal condition. In Table 16 the main test parameters and the performed test phases of the experiment are summarised.

During the transient state and steady state of each heating period, Infrared camera images on the melt surface were recorded and the crust detection lance was used to measure the position of crust/melt boundary, the boundary layer temperature gradient and the pool temperature vertical profile. Melt samples were taken during the steady state of each heating period.

Table 16: Designed test parameter and test phases of the experiment LIVE-L5L

	LIVE-L5L **1-4.12.2008**	
Melt characteristics and preparation		
Type	$NaNO_3$	KNO_3
Mole %	20 %	80 %
Mass %	17.37 %	82.63 %
Mass	68 kg	324 kg
Total mass	392 kg	
Loading of the furnace	~210 l melt (for T=350°C)	
Poured Mass	1. pouring: 120 l (corresponds to ~31 cm melt height) 2. pouring 90 l (corresponds to ~43.5 cm melt height)	
Initial temperature	350 °C	
Flow rate of nitrogen covering	2 l/min	

Melt pour	
Position	central
Number of pours	2
Furnace tilting velocity	0.5 °/s for both pours
Furnace target angle	1. pouring 76°, 2. pouring 91°
Hold time	120 s for both pours
Trace heating pouring spout	360 °C
Phase 1: 1. pouring 120 l, 10 kW	
Start pouring	0 s
Start heating	80 s
Cooling conditions	Water, continuous cooling
Cooling water flow rate	~1.3 kg/s
Heating planes	All
Heating power	10 kW
Heat generation	Homogeneous for 31 cm melt height
Maximum melt temperature	370 °C
Phase 2: 2. pouring 90 l, 18 kW	
Start pouring	16248 s
Start heating	16374 s (4.55 hours)
Cooling conditions	Water, continuous cooling
Cooling water flow rate	~1.3 kg/s
Heating planes	All
Heating power	18 kW
Heat generation	Homogeneous for 31 cm melt height
Maximum melt temperature	370 °C
Phase 3: 10 kW-l heating phase	
Test conditions	Reaching of steady state conditions in Phase 2
Start time	83975 s (23.33 hours)
Boundary conditions	Water, continuous cooling
Cooling water flow rate	~1.3 kg/s
Heating planes	All
Heating power	10 kW
Heat generation	Homogeneous for 31 cm melt height
Maximum melt temperature	370 °C
Phase 4: 5 kW heating phase	
Test conditions	Reaching of steady state conditions in Phase 3

Start time	107989 s (30 hours)
Boundary conditions	Water, continuous cooling
Cooling water flow rate	~1.3 kg/s
Heating planes	All
Heating power	5 kW
Heat generation	Homogeneous for 31 cm melt height Homogeneous for 31 cm melt height
Maximum melt temperature	370 °C
Phase 5: 10 kW-II heating phase	
Test conditions	Reaching of steady state conditions in Phase 4
Start time	172805 s (48 hours)
Boundary conditions	Water, continuous cooling
Cooling water flow rate	~1.3 kg/s
Heating planes	All
Heating power	10 kW
Heat generation	Homogeneous for 31 cm melt height
Maximum melt temperature	370 °C
Phase 6: 18 kW-II heating Phase	
Test conditions	Reaching of steady state conditions in Phase 5
Start time	190809 s (53 hours)
Boundary conditions	Water, continuous cooling
Cooling water flow rate	~1.3 kg/s
Heating planes	All
Heating power	18 kW
Heat generation	Homogeneous for 31 cm melt height
Maximum melt temperature	370 °C
Phase 7: Test termination and melt extraction	
End time	263011 s (73 hours)
Test conditions	Reaching of steady state conditions in Phase 6
Heating power	0 kW

Table 17: Test performance in chronological order during LIVE-L5L test

Time of day	Event
1.12.2008	
8:01	Melt temperature in furnace 347 °C and 352 °C
8:30	PC data acquisition start
8:56	Outer vessel cooling start, ~1.3 l/s
8:58	Video record pouring start
8:58:30	Video record vessel vertical and lateral start
8:59	Weight of test vessel 2013 kg, with pouring spout
8:59	IR camera record start
1. Pouring, 10 kW	
9:00	Start of pouring program, poured mass 120 l, pouring position central
9:00-9:15	Infrared image recording
9:03	Heating system on, P = 10 kW homogeneous
9:03:45	End of pouring, the heating furnace was driven back
9:11:30	Weight of test vessel 2246 kg without pouring spout
9:20	Crust detection lance measurement during transient state
11:30	Crust detection lance measurement during steady state
13:00-13:05	Infrared image recording
13:15	Melt sampling
13:28	Video record pouring start
13:28:30	Video record vessel vertical and lateral start
2. Pouring, 18 kW-l	
13:30:00	2. Pouring start, central, 90 l
13:30-13:45	Infrared image recording
13:34:00	Heating power 18 kW, homogenous for 31 mm melt height
13: 35:05	End of 2. pouring
13:45:03	Weight of test vessel 2408 kg without pouring spout
13:50	Crust detection lance measurement during transient state
14:44	Pouring spout removed
15:30	Crust detection lance measurement during steady state
2.12.2008	
8:00-8:05	Infrared image recording
8:15	Melt sampling
10 kW-l	
8:20	Heating power reduction to 10 kW, homogenous for 31 mm melt height

8:40-8:45	Infrared image recording
14:00	Crust detection lance measurement during steady state
14.45	Infrared image recording
14:55	Melt sampling
5 kW	
15:00	Heating power reduction to 5 kW, homogenous for 31 mm melt height
15:05-15:10	Infrared image recording
15:15	Crust detection lance measurement during transient state
3.12.2008	
8:00	Crust detection lance measurement during steady state
8:40	Infrared image recording
8:47	Melt sampling
10 kW-II	
9:00	Heating power increase to 10 kW, homogenous for 31 mm melt height
9:05	Infrared image recording
9:15	Crust detection lance measurement during transient state
13:00	Crust detection lance measurement during steady state
13:45	Infrared image recording
13:55	Melt sampling
18 kW-II	
14:00	Heating power increase to 18 kW, homogenous for 31 mm melt height
14:05	Infrared image recording
14:10	Crust detection lance measurement during transient state
4.12.2008	
8:45	Crust detection lance measurement during steady state
9:30	Infrared image recording
9:41	Melt sampling
9:56	Weight of test vessel 2407 kg (without suction tube, with suction funnel)
10:03	Start extraction of residual melt
10:03	Heating power 0
10:20	Cooling water off
10:30	PC data acquisition stop

6 LIVE-L5L test results

6.1 Melt mass and cooling water

Two melt releases were performed during LIVE-L5. Both were released centrally. The temperature measured at the pouring spout were 342 °C at the first melt release and 336 °C at the second melt release. Figure 33 shows the change of vessel weight during the two melt releases: 225.5 kg of melt was released during the first pouring and 163.5 kg was released during the second pouring. So that after the second pouring the melt mass in the vessel was 389 kg. According to the density of the melt at its initial temperature, the volume of the melt after the first release was 120.5 l and after the second melt release was 208 l. The real melt mass agreed well with designed value of 210 l.

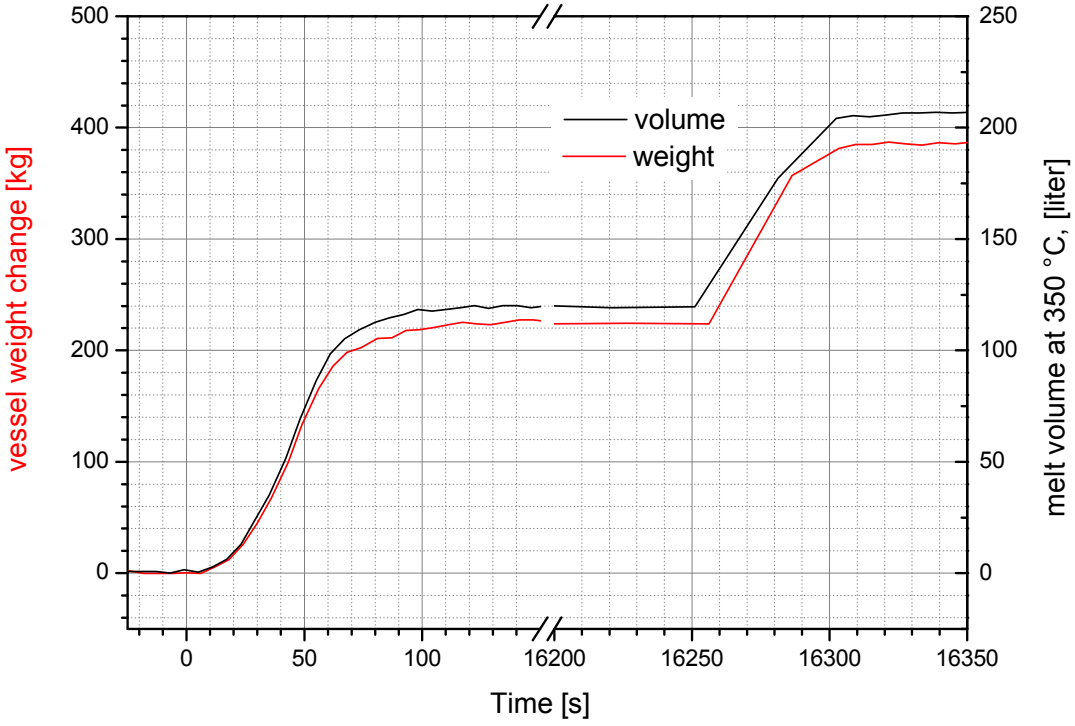

Figure 33: Weight change of vessel during the first pouring and second pouring

The inlet cooling water temperature was about 9.7 °C and the outlet temperature was dependent on the heating power and varied from 10 °C to 13 °C, as shown in Figure 34. The flow rate of the cooling water was between 1260 to 1300 kg/s with the mean value of 1288 g/s, as shown in Figure 35. The high flow rate and the correspondent minor variation in the cooling water temperature inside the cooling vessel created a quasi isothermal condition on the outer surface of the test vessel.

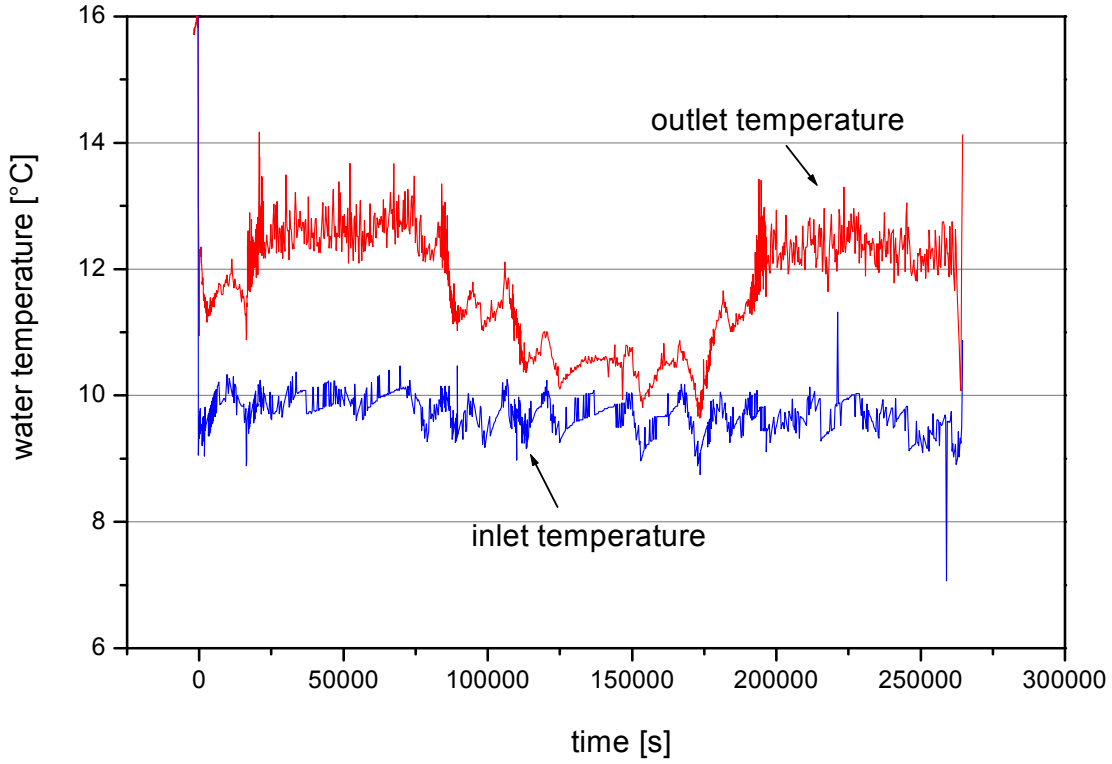

Figure 34: Cooling water temperature during LIVE-L5L

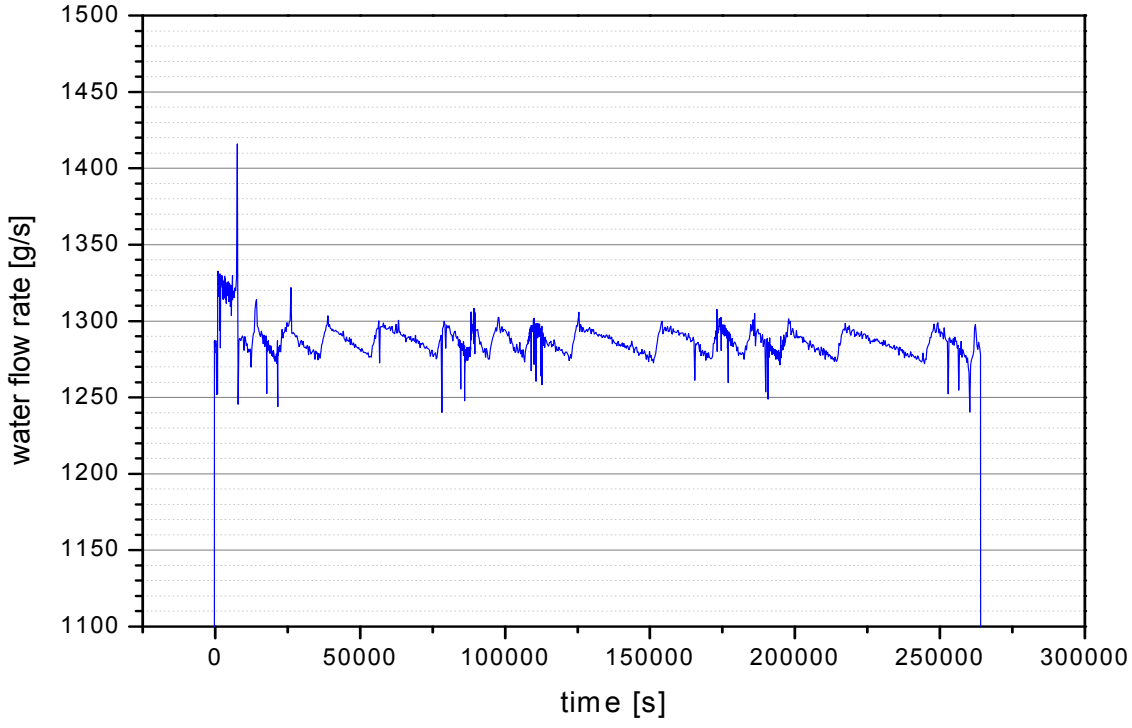

Figure 35: Cooling water flow rate during LIVE-L5L

6.2 Decay heat simulation in LIVE-L5L

The decay heat was simulated by 6 planes of heating wires. The heating system was described in detail in 2.3. The volumetric heating was performed from the vessel bottom to 31 cm of vessel height. During the L5L test, 10 kW was performed after the first pouring and 18 kW after the second pouring. After the second melt pouring the heating plateaus were scheduled as LIVE-L4, which were18 kW-I, 10 kW-I, 5 kW, 10 kW-II and 18 kW-II in chronological order. The height of melt surface was 314 mm after the first melt pouring and 430 mm after the second melt pouring. In Table 18 the heating periods, the heating power of each plane and the total heating power are given. The real heating power in each heating period was in gut agreement with the planed heating power.

Table 18: Heating power and heating periods during LIVE-L5L

		10 kW **1st. pouring** 80-16247 s	**18-kW-I** **2nd pouring** 16248-83974s	**10 kW-I** 83975-107988 s	**5 kW** 1087989-172804 s	**10 kW-II** 172805-190808 s	**18 kW-II** 190809-263011 s
	Height [mm]	[W]	[W]	[W]	[W]	[W]	[W]
HE1	36.4	2906	5223	2911	1493	2927	5206
HE2	90.4	2230	4043	2229	1115	2243	4041
HE3	135.4	1854	3425	1858	894	1869	3425
HE4	182.4	1431	2587	1432	723	1439	2587
HE5	233.4	1032	1884	1031	507	1036	1885
HE6	278.4	505	918	505	252	508	918
Total		9957	18081	9966	4984	10022	18062

6.3 Melt behaviour in LIVE-L5L

The transient melt temperatures after melt release and after power reductions were shown in Figure 36. The original melt temperature was cooled to about 330 °C when the first melt release was finished, then the melt pool underwent temperature stratification process, in which the pool lower part cooled down further whereas in the middle and the top part the melt temperature increased at first and then reduced to steady values. The melt temperature stratification process took about 2000 seconds. The stabilized melt temperature after the second melt release was 8°C higher at bottom and 4 °C higher at the melt surface comparing their corresponding values after the first pouring.

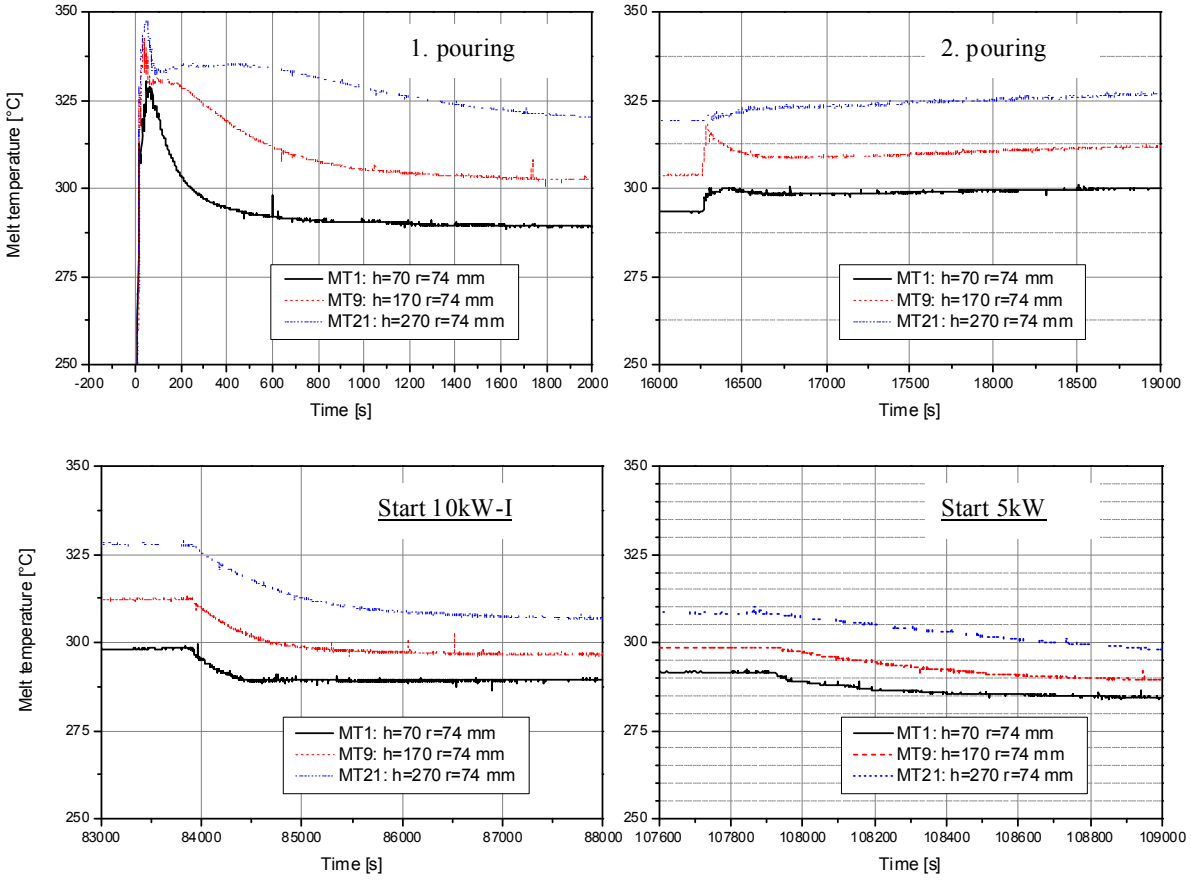

Figure 36: Melt temperature during transient states in LIVE-L5

Reducing the heating power from 18 kW to 10 kW and from 10 kW to 5 kW resulted in decrease of the melt pool global mean temperature of 17 °C and 6 °C respectively. During all the transient processes the lower part of the pool reached steady state quickly than the upper part of the pool.

An overview of the melt temperature during the whole test is given in Figure 37. The considerably low melt temperature at the position of MT5 indicates that the crust covered the thermocouple. In the top and the middle part of the pool the melt temperature was horizontally homogenous. The melt temperature vertical distribution were identical during the same power density but different heating periods, e.g. during 18kW-I and 18 kW-II, or during 10 kW-I and 10 kW-II. The melt temperature along the azimuths at 90°, 180° and 270° are similar to the temperature measurements along the azimuth at 0°, which are shown in Figure C-1 to Figure C- 3.

The melt temperature distribution during steady state periods is given in Table 19. The given values are the average of 25 measurements in 2 minute. The global mean melt temperatures (T_{mean}) are also given in Table 19. Figure 38 shows the melt temperature along vessel height at five heating periods. The vertical temperature gradient became greater with increasing heating power. The dimensionless melt temperature distribution in term of temperature difference between melt temperature and interface temperature $(T-T_{int})/(T_{mean}-T_{int})$ or $\Delta T/\Delta T_{mean}$

shows that the slopes of $\Delta T/\Delta T_{mean}$ were identical of all the heating powers except 5 kW, as shown in Figure 39.

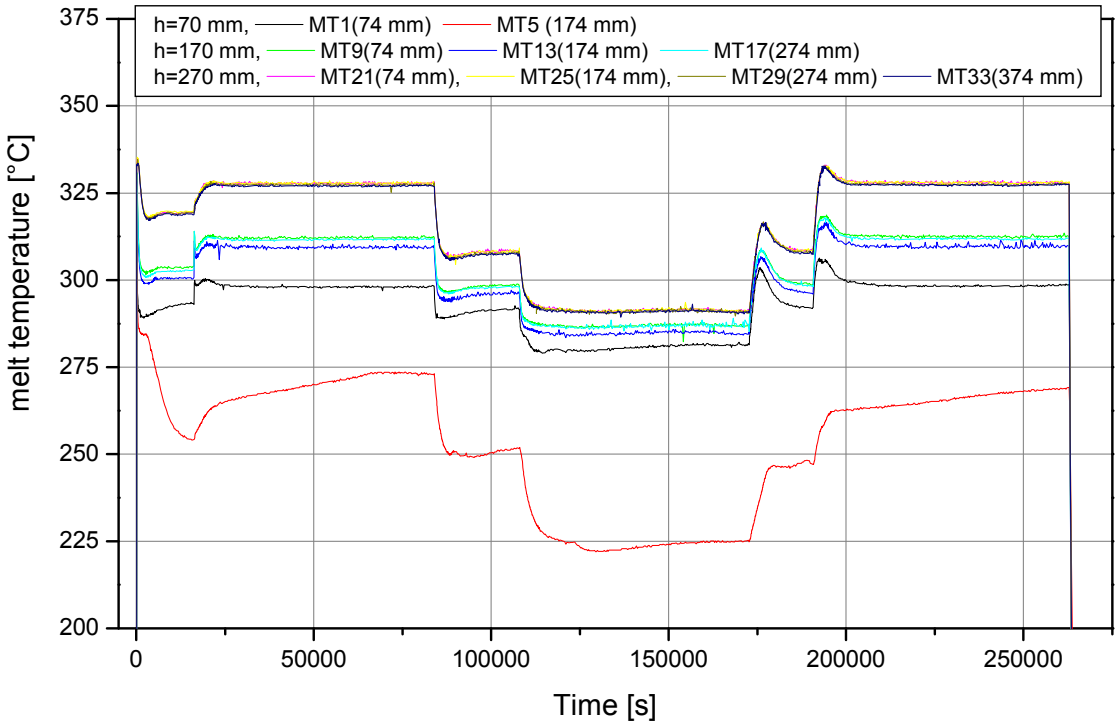

Figure 37: Melt pool temperatures at different height and radius along the azimuth 0° in LIVE-L5L

Table 19: 60 s mean melt temperature during the steady states of LIVE-L5L

Radius [mm]	Height [mm]	Azimuth angle				
		0°	90°	180°	270°	mean
Test phase 1:1. pouring, 10 kW, t = 15000 s						
74	70	289.5	287.1	290.7	288.2	288.9
	170	303.3	304.6	302.6	306.6	304.2
	270	322.8	325.4	324.3	323.0	323.9
174	70	284.5	288.8	288.0	288.4	287.4
	170	300.1	302.7	303.9	302.3	302.2
	270	323.1	324.6	323.4	324.7	323.9
274	170	302.2	303.6	303.4	303.2	303.1
	270	322.8	323.4	322.6	322.1	322.7
374	270	322.7	323.9	324.5	323.1	323.5
Global mean T_{mean}		310.6				
Test phase 2: 2. pouring, 18 kW-l, t = 80000 s						
74	70	298.1	295.6	298.9	295.7	297.1
	170	312.3	313.7	311.3	314.8	313.0
	270	327.8	329.8	328.9	327.7	328.5

174	70	273.0	258.3	295.7	241.0	267.0
	170	309.5	311.4	312.4	310.6	311.0
	270	327.9	328.7	327.7	328.8	328.2
274	170	311.8	312.3	311.8	312.8	312.2
	270	327.4	327.1	326.7	327.0	327.0
374	270	327.1	327.9	328.7	326.8	327.6
Global mean T_{mean}		323.2				
Test phase 3: 10 kW-I, t = 100000 s						
74	70	291.5	288.6	292.5	289.5	290.5
	170	298.4	299.8	297.3	301.4	299.2
	270	308.3	310.1	309.2	308.1	308.9
174	70	250.4	238.0	263.0	232.3	245.9
	170	295.9	297.6	298.8	297.1	297.3
	270	308.2	309.1	308.2	309.2	308.7
274	170	297.8	298.6	298.1	299.3	298.4
	270	307.7	307.6	307.2	307.4	307.5
374	270	307.5	308.0	309.1	306.8	307.9
Global mean T_{mean}		305.2				
Test phase 4: 5 kW, t = 175000 s						
74	70	281.4	282.9	285.6	280.3	282.5
	170	286.8	288.3	285.5	289.6	287.6
	270	291.1	293.0	292.4	291.1	291.9
174	70	225.0	214.3	251.8	208.3	224.8
	170	284.6	286.2	287.3	285.5	285.9
	270	291.2	292.1	291.1	292.6	291.7
274	170	286.8	287.7	275.2	287.5	284.3
	270	290.8	290.9	290.5	290.7	290.7
374	270	290.6	291.8	292.6	291.0	291.5
Global mean T_{mean}		289.8				
Test phase 5: 10 kW-II, t = 185000 s						
74	70	292.6	289.4	293.4	290.7	291.5
	170	299.5	300.9	298.3	302.1	300.2
	270	308.8	310.7	310.0	308.8	309.6
174	70	246.5	239.0	266.4	227.1	244.7
	170	297.1	298.6	299.9	297.9	298.4
	270	308.8	309.7	308.9	310.1	309.4
274	170	298.9	299.5	298.9	300.1	299.4
	270	308.3	308.4	307.8	308.1	308.1
374	270	308.0	308.7	309.4	309.0	308.8
Global mean T_{mean}		292.6				
Test phase 6: 18 kW-II, t = 250000 s						
74	70	298.4	296.2	299.2	295.9	297.4
	170	312.5	313.7	311.3	314.9	313.1

	270	327.9	329.7	329.0	327.6	328.6
174	70	268.0	263.2	296.3	240.7	267.1
	170	309.7	311.4	312.9	310.9	311.2
	270	328.0	328.7	327.8	328.7	328.3
274	170	311.9	312.5	311.8	312.9	312.3
	270	327.4	327.4	326.7	327.0	327.1
374	270	327.3	327.9	328.7	327.0	327.7
Global mean T_{mean}		323.1				

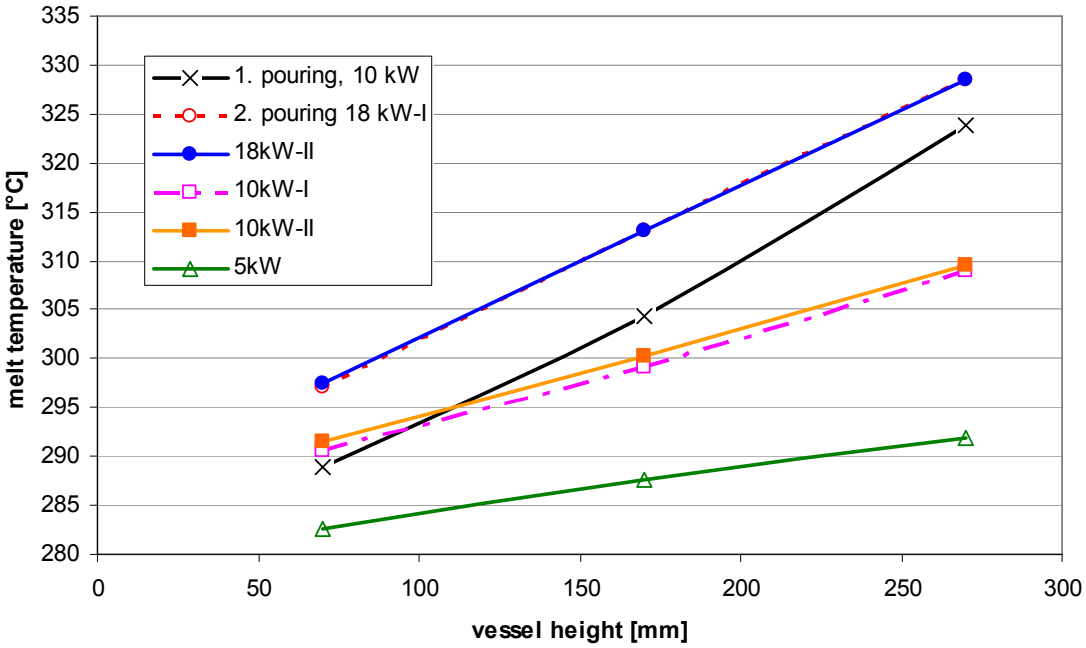

Figure 38: Steady state melt temperature at radius 74 mm during LIVE-L5L

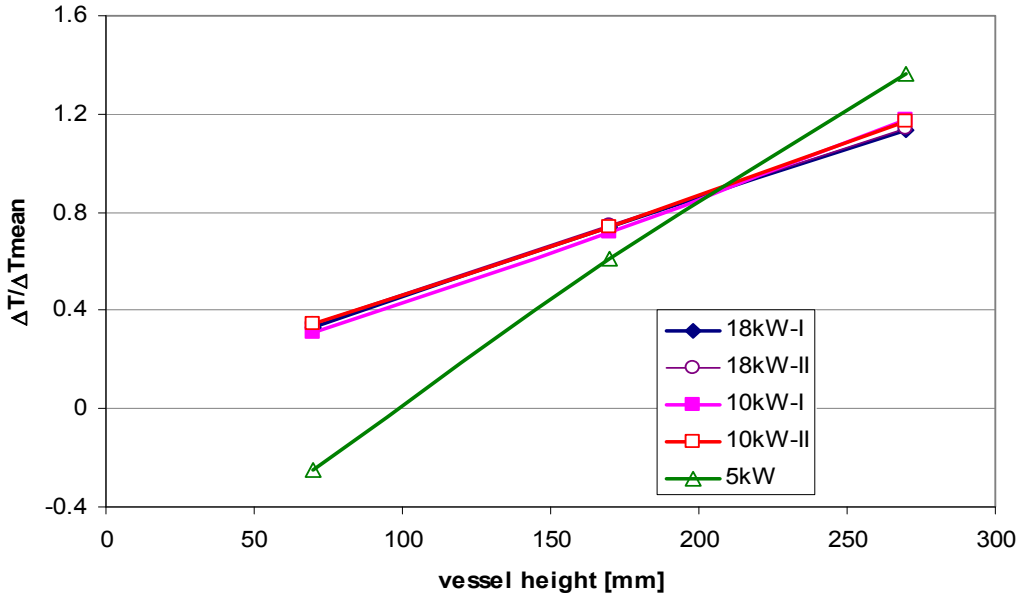

Figure 39: $\Delta T/\Delta T_{mean}$ $((T-T_{int})/(T_{mean}-T_{int}))$, at radius 74 mm in LIVE-L5L

The melt boundary at the melt /crust interface and the temperature and the melt temperature vertical profiles were measured with the crust detection lance during transient states and during the steady states of the 6 heating periods. Since the melt temperature horizontal distribution in the upper part of the pool was very homogenous, the values from MT thermocouples are therefore combined with the values of the crust detection lance, thus the whole melt pool vertical temperature profile can be obtained which is shown in Figure 40. The melt temperature in this diagram indicates that there was a temperature-stratified zone in the lower part and a homogenous zone up from 300 mm of the melt pool.

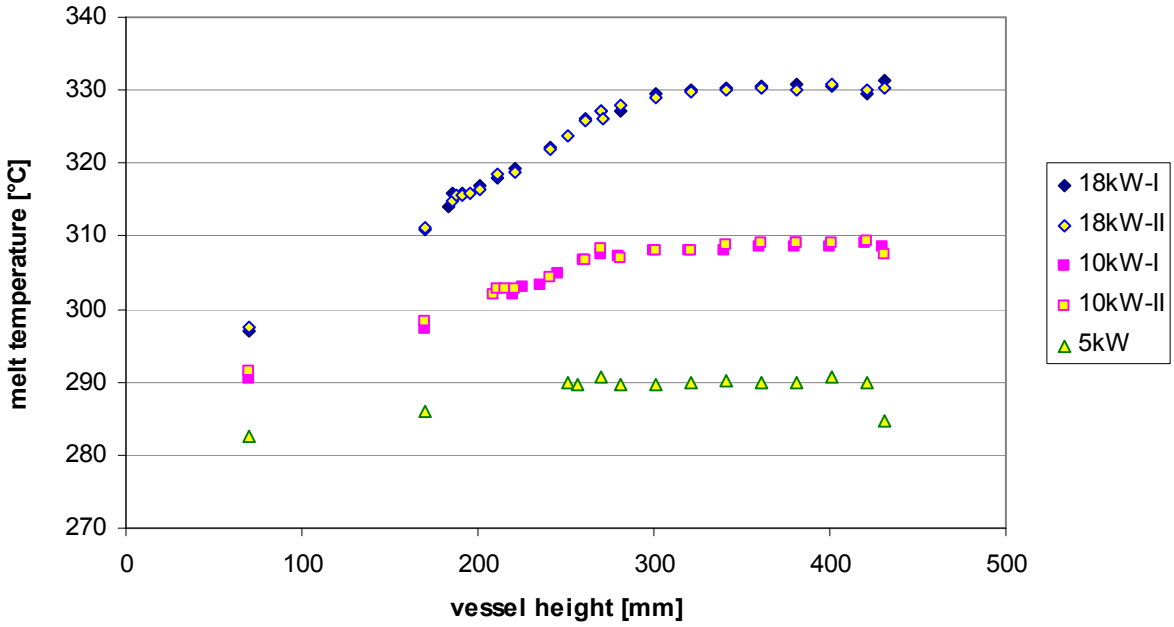

Figure 40: Melt pool temperature profiles during LIVE-L5L

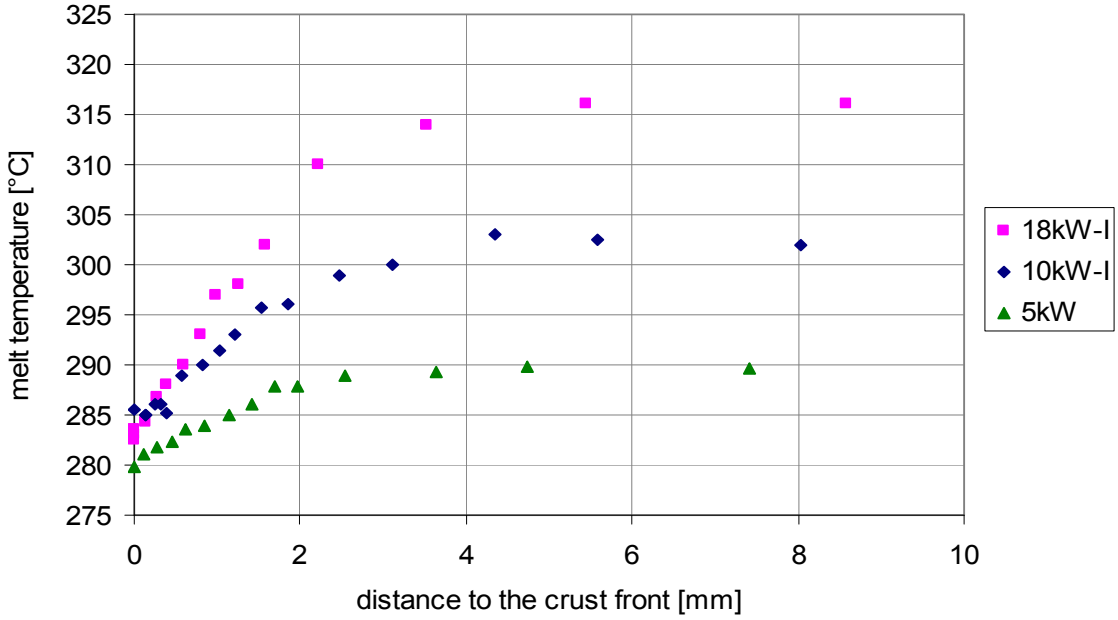

Figure 41: Melt temperature in boundary layer during LIVE-L5L

The boundary temperature ahead of the crust front is shown in Figure 41. The temperature boundary layer was about 4 mm thick. The temperature gradients within the boundary layer in 18 kW, 10 kW and 5 kW heating power were 12.4 °C/mm, 6.6 °C/mm and 4.3 °C/mm respectively. The crust/melt interface temperature was lowest during the 5 kW heating period (279.5 °C). This could be a result of the profound crust formation due to the low heating power.

6.4 Melt surface behaviour

As it is described in the section 2.4, an infrared (IR) camera is installed at the lid of the facility to observe the melt surface behaviour near to the vessel wall. The recorded thermograms are used to measure the temperature distribution on the surface of the molten pool and to identify the convection patterns in the fluid during different stages of experiments (Figure 42). The dark field in the middle of the image was a result of the reflection from the camera opening in the upper lid.

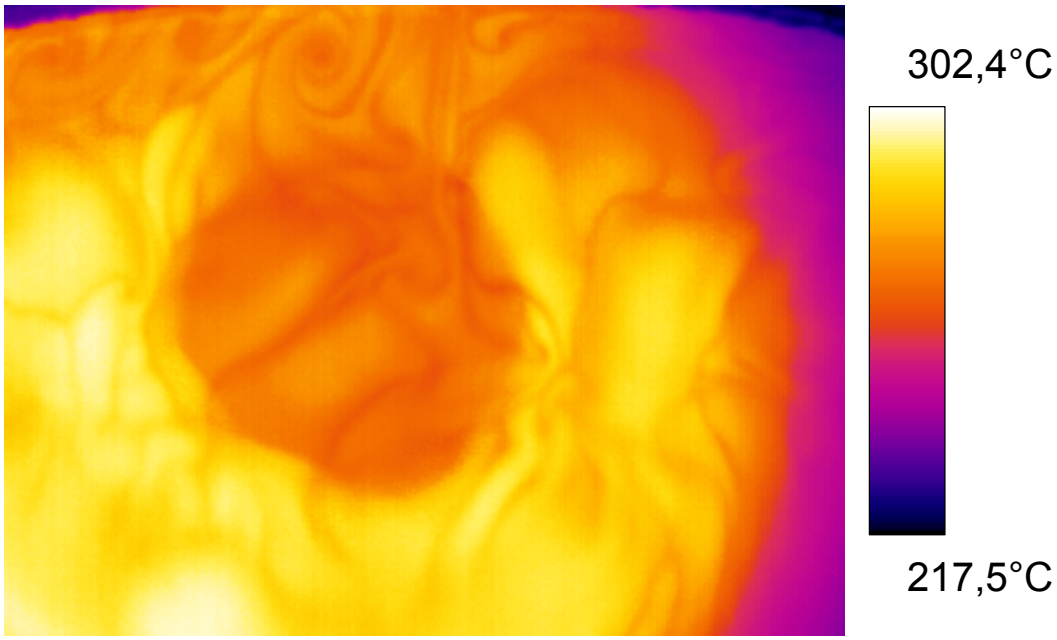

Figure 42: An infrared image taken during the steady state of 18kW-II in L5L test

The analysis of the recordings shows a complex picture of the fluid motion at the upper surface. The general trend is that the fluid is transported from the center to the vessel wall. To quantify the flow horizontal velocity at the melt surface, the IR pictures were analysed similarly to particle image velocimetry (PIV). Instead of seeds used in PIV, moving areas of the melt surface with distinctive patterns were used, assuming that they follow the flow dynamics. The displacement of the patterns after 1 second was determined and the flow velocity was calculated. In LIVE-L5L the flow velocity of the upper surface has been analysed during the transient phase and during the steady-state phase of all six heating periods.

The results of the measurements are presented in and the average value of the measurements is shown in Figure 44. The X-axis is given in the dimensionless term R/R_{ves} where R is the starting radial position of the analysed point and R_{ves} is the vessel radius (50 cm). The complex motion pattern leads to a large scatter of the results.

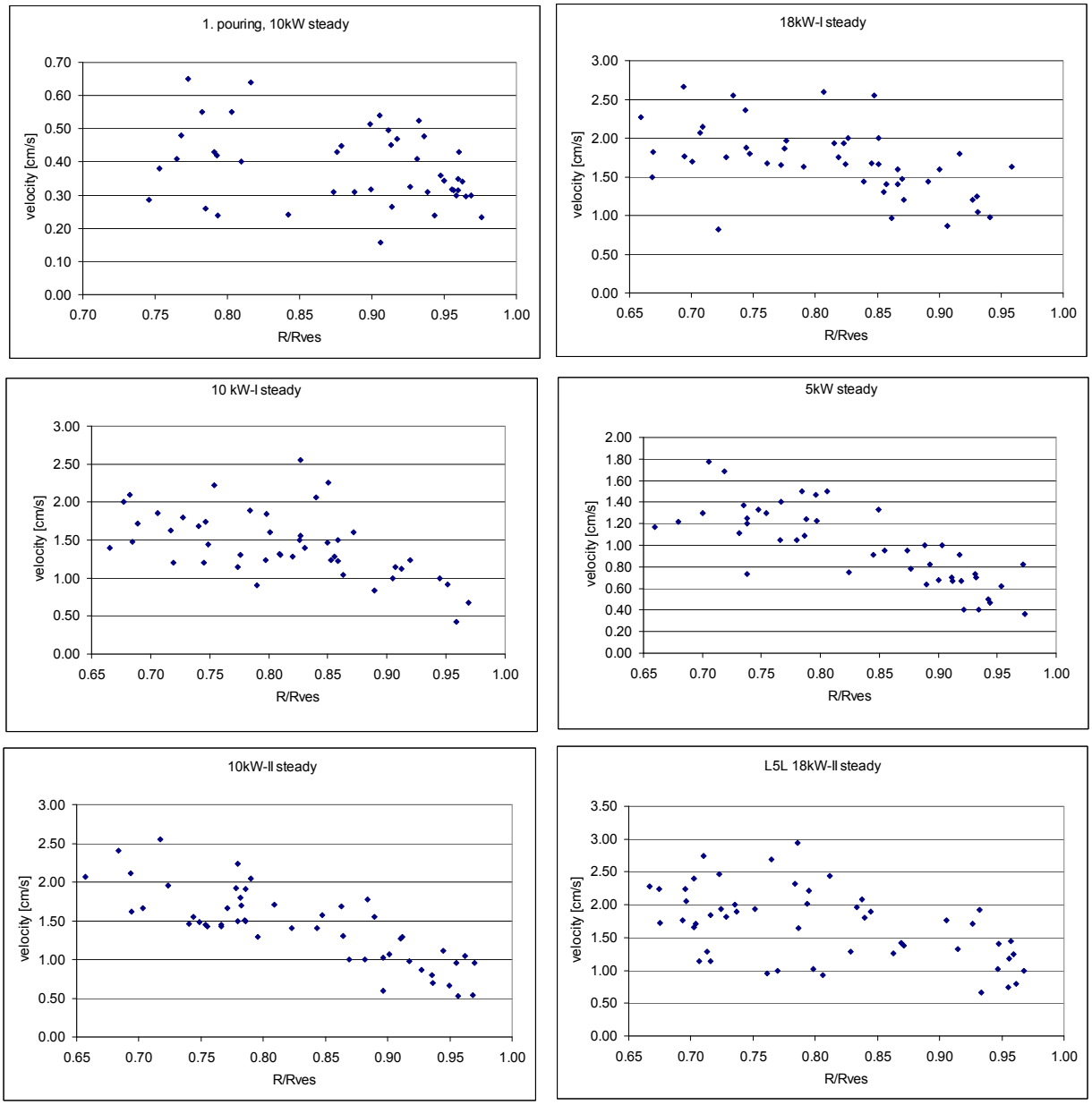

Figure 43: Flow horizontal velocities determined from Infrared images during L5L test

Nevertheless the average surface flow velocity shows some general trends:

- Hot melt moved upwards from the central area to the melt surface, drifting towards the wall and sunk near the wall area.

- Increasing the melt pool height results in an increase of the flow velocity. At vessel height of 310 mm, the maximum velocity was 0.65 cm/s, where at the vessel height of 413 mm, the maximum velocity at 18 kW-I heating period was 2.7 cm/s.

- Increasing power density leads to corresponding increase of melt flow velocity.

- The flow velocity at the central area was greater than the near-wall region.

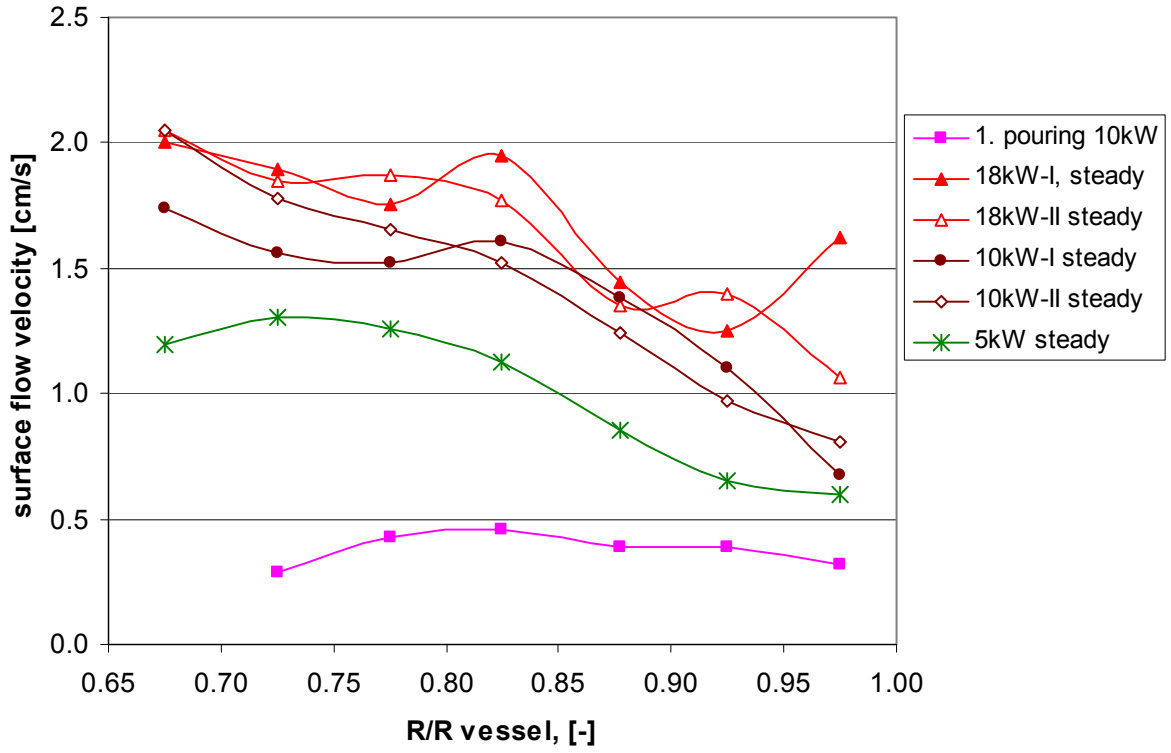

Figure 44: Average surface flow velocities during the steady states in LIVE-L5L

6.5 Heat flux and heat balance in LIVE-L5L

6.5.1 Steady state heat fluxes in LIVE-L5L

The method of heat flux calculation of LIVE-L5L is the same as the one in LIVE-L4 calculation described in 4.4. It is noticed that some IT thermocouples were disconnected with the wall during the test. IT3 and IT7 at azimuth angle 112.5° were loose from the wall at the beginning of the test, whereas IT6 at azimuth angle 22.5° was detached at the beginning of 5 kW heating period. The escalation values of IT6 and IT7 thermocouples after the detachment are shown in Figure 45. It is also observed that during the initial period of 5 kW a sudden increase of wall inner temperature took place also at other locations, indicating that hot melt penetrated through the crust and filled in the gap between the crust and vessel wall. After this event, IT7 thermocouple obtained good contact with the vessel wall. However a new gap formed at the beginning of 10 kW-II period and IT7 showed misleading value again. The crust was examined after the test which is shown in Figure 46. A thin crust layer was formed between the vessel wall and the bulk crust. This crust layer can be easily separated with the rest of the crust after the test, suggesting it came from the hot melt penetrating the crust and filling the gap. Due to the unreliable measurements of IT7 and IT6 their values are not counted in the calculation of the average heat flux at the corresponding level. The horizontal mean heat flux in these cases was calculated based on the measurements from the rest of the IT thermocouples. In Table 20 the wall inner temperatures and outer temperatures during the steady states of L5L are given. And in Table 21 the local heat flux through wall, the hori-

zontal mean heat flux and the global mean heat flux during the steady states of the six heating periods are given.

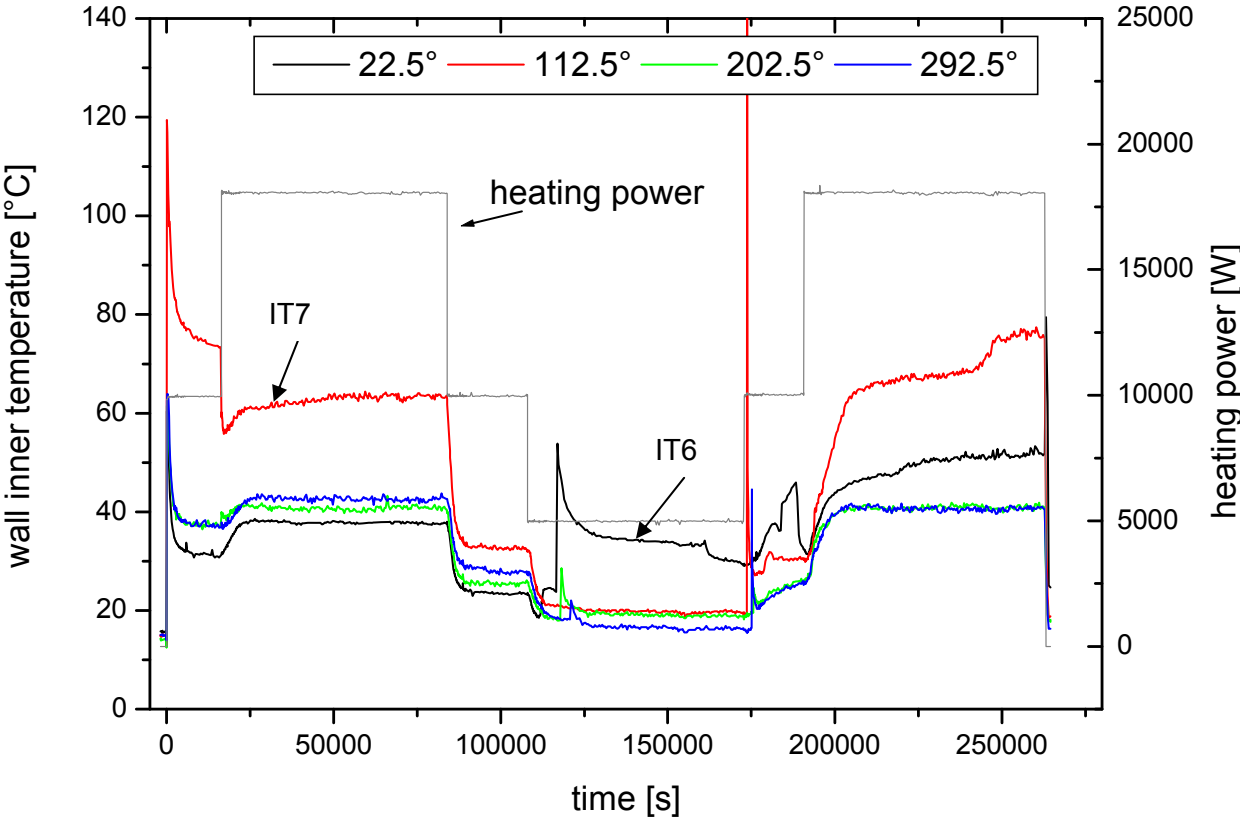

Figure 45: Temperature departure of IT7 and IT6, and gap formation during LIVE-L5L

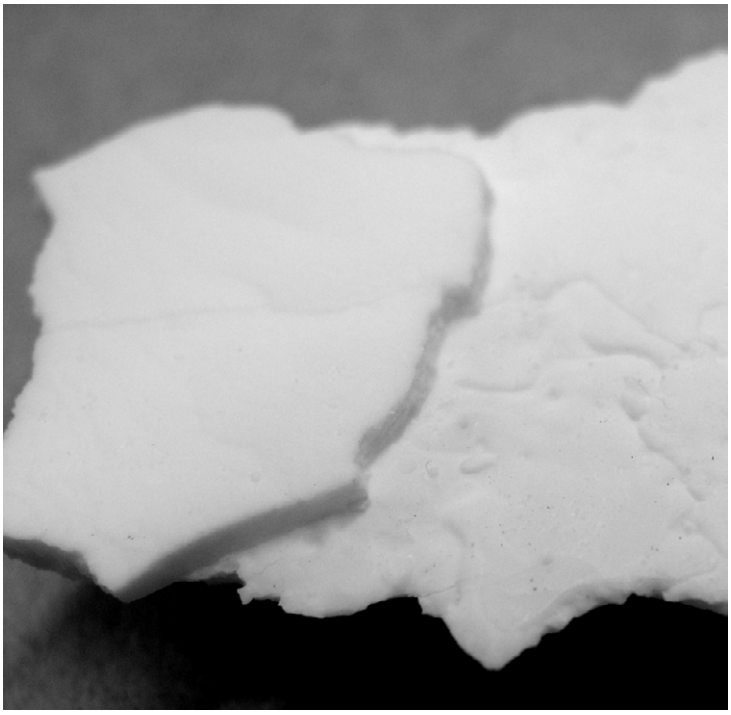

Figure 46: Post test examination: crust with an easily seperated layer at the vessel wall

Table 20: Wall inner temperatures and outer temperatures during the test in L5.

	IT				OT			
	azimuth angle [°]				azimuth angle [°]			
polar angle	22.5	112.5	202.5	292.5	22.5	112.5	202.5	292.5
	1. pouring, 10 kW, 15000 S							
0.0		15.8				11.0		
30.0	17.6	32.7[2]	18.8	15.8	11.5	11.5	12.6	12.1
51.0	31.0	**Defect[1]**	37.6	36.9	16.9	19.5	24.2	25.1
65.5	49.9	60.6	66.7	75.7	25.4	34.8	37.1	36.2
76.5	19.5	26.7	30.2	29.4	15.1	21.7	25.8	24.1
	2. pouring 18kW-I 80000 s							
0.0		16.5				11.2		
30.0	19.0	26.6[2]	20.2	17.4	11.9	11.6	13.2	12.5
51.0	37.6	**defect[1]**	40.8	42.5	18.9	20.5	26.5	26.7
65.5	50.2	58.2	66.0	73.6	27.3	34.2	38.4	37.9
76.5	68.3	75.6	79.3	73.3	37.9	41.0	45.1	44.8
	10kW-I 100000 s							
0.0		16.0				11.1		
30.0	16.3	23.4[2]	19.7	14.7	11.4	11.0	12.1	11.5
51.0	23.4	**Defect[1]**	24.6	28.5	14.8	16.4	17.8	21.3
65.5	31.7	38.5	41.4	41.5	19.2	25.8	27.2	26.2
76.5	40.1	47.4	48.2	45.3	25.0	29.0	32.1	31.7
	5kW 170000 s							
0.0		15.3				10.8		
30.0	15.0	20.8[2]	16.2	12.5	10.8	10.7	11.6	11.3
51.0	**Defect[1]**	**Defect[1]**	18.9	16.5	12.2	12.2	15.2	14.3
65.5	16.9	22.6	23.0	20.5	13.3	17.0	18.3	16.4
76.5	19.8	24.1	25.9	22.9	14.8	18.1	20.4	18.4
	10kW-II 185000s							
0.0		15.4				10.9		
30.0	15.4	22.0[2]	18.3	13.2	11.0	10.7	11.9	11.3
51.0	**Defect[1]**	**Defect[1]**	25.0	24.5	13.3	16.1	18.6	19.2
65.5	30.3	39.4	41.9	42.8	18.8	25.4	27.7	26.3
76.5	41.3	50.8	50.9	47.9	25.5	31.2	33.7	32.5
	18kW-II 250000s							
0.0		15.7				10.7		
30.0	18.6	23.1[2]	19.3	16.1	11.6	11.6	13.1	12.6
51.0	**Defect[1]**	**Defect[1]**	40.3	40.5	19.1	20.7	25.5	26.8
65.5	51.6	59.8	61.1	65.6	27.2	34.3	37.2	36.9
76.5	66.3	78.2	75.7	74.4	35.9	41.3	44.5	44.7

Note: [1]: thermocouples are defect during the test; [2]: thermocouples are detached.

Table 21: Steady state heat flux during LIVE-L5L

	Polar angle	Azimuth angle				Mean	Global mean value
		22.5	112.5	202.5	292.5		
1. Pouring 150003s	0	2680				2680	7928
	30	3464		3450	2016	2977	
	51	7978		7687	6863	7509	
	65.5	13958	14755	16961	22604	17070	
	76.5	2494	2767	2583	2860	2676	
2. Pouring 18kW-I 80000s	0	2963				2963	11038
	30	3968	3546	3936	2734	3456	
	51	10611	9329	8278	9099	9329	
	65.5	12943	15714	15761	20413	15714	
	76.5	17436	18116	19366	16180	18116	
10kW-I 100000s	0	2698				2698	5617
	30	2760		4182	1744	2895	
	51	4856		3663	4155	4225	
	65.5	6968	7046	7959	8624	7649	
	76.5	8378	9995	8922	7695	8748	
5kW 170000s	0	2486				2486	2188
	30	2327		2553	709	1863	
	51			1998	1126	1562	
	65.5	1973	2938	2655	2255	2455	
	76.5	2702	3284	2949	2485	28554	
10kW-II 185000s	0	2555				2555	5462
	30	2444		3458	1045	2316	
	51			3550	3020	3285	
	65.5	6512	7788	7881	9266	7862	
	76.5	9044	11039	9507	8542	9533	
18kW-II 250000s	0	2779				2741.1	10383
	30	3877		3468	1928	3091	
	51			8468	7983	8226	
	65.5	13977	14722	13602	16331	14658	
	76.5	16846	20908	17713	16731	18050	

The profiles of the level mean heat flux along vessel wall polar angle during the steady states are also illustrated in Figure 47 Following characteristics of heat flux distribution can be observed from this diagram:

- increasing power density increases the heat flux significantly upon polar angle 30° and has little influence on heat flux at the vessel bottom;

- heat fluxes in same heat generation rate but during different heating periods were well comparable, such as the heat flux during 18 kW-I and 18 kW-II periods, and during 10 kW-I and 10 kW-II periods;

- The focusing effect of heat flux near melt surface (q_{max}/q_{global}) in a small melt pool, e.g. the 120 l was more significant ($q_{max}/q_{global}=2$) than the large melt pool in which the value was between 1.64 to 1.75 (Figure 48). However, the absolute maximum heat flux in a large pool was higher than a small pool. There was almost no heat flux focusing at the upper surface when the power density was very low.
- The calculated local heat flux calculation has moderate deviation and the heat flux level mean values are subjected to larger uncertainties, which is affected by the measuring uncertainty of local IT as well as by the asymmetry of horizontal heat flux distribution. Especially large deviation was calculated at the lower part of the vessel wall and in low power density (Table D- 2).

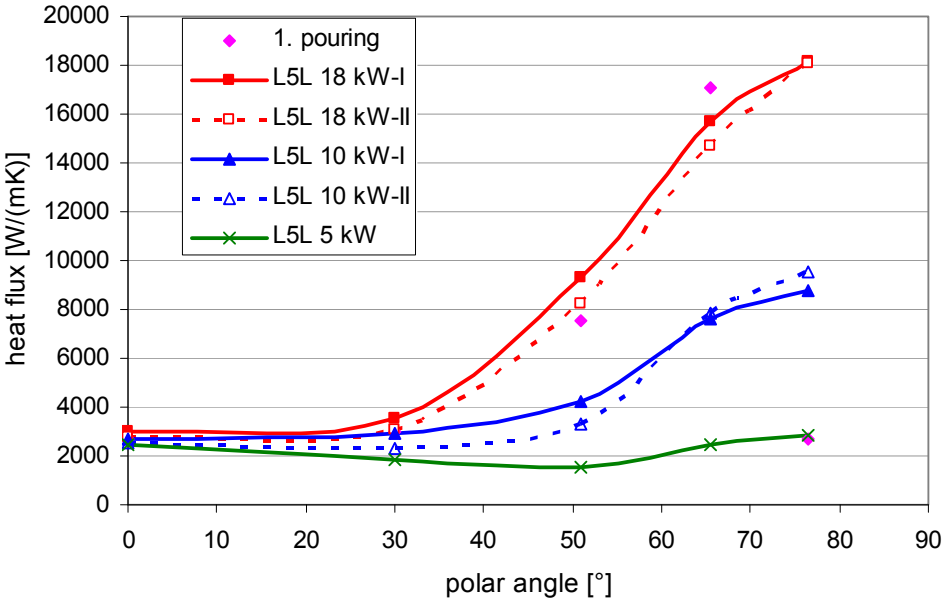

Figure 47: Heat flux profiles along vessel wall during different heating periods in LIVE-L5L

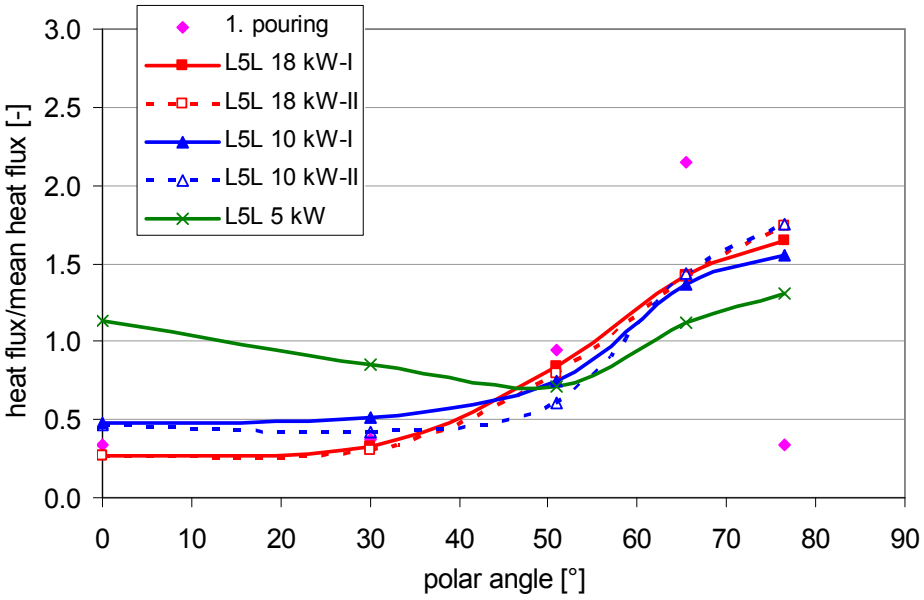

Figure 48: Heat flux /global heat flux in different heat generation rates in LIVE-L5L

6.5.2 Transient wall temperature and heat flux

The transient wall temperature and heat flux after the first melt pouring and the second melt pouring were examined. The transient wall temperature after the first melt pouring is shown in Figure 49. Depending on the location the maximum wall inner temperature was reached at different time. At the polar angle 30°, the maximum value was reached during the melt pouring period, whereas at 51° the maximum value appeared within the 4 minutes after the finishing of melt pouring, and at the uppermost part of the vessel wall the maximum appeared in 6-10 minutes after the finishing of melt pouring. Furthermore, the duration of the high temperature period was longer at the upper part of the melt pool. Above observation suggests that short thermal shock could take place in the lower part of vessel due to the contact with down-pouring melt jet whereas the upper part of the vessel wall could be subjected to a long period of high temperature during the melt pool stabilization process. In the LIVE-L5L case the duration of the high temperature period at 65.5° was about 20 minutes. The timing and the IT maximum are also given in Table 22.

The timing of transient heat flux reflected the IT temperature features, as shown in Figure 50. The highest transient heat flux located at polar angle 30°. However, the heat flux at this position decreased faster to the steady state value than at polar angle 65°. The maximum heat flux at 30° was about 10 times of its steady state value, whereas at 65° the maximum heat flux was only about 1.5 times of its steady state value.

Table 22: the maximum IT temperatures and their timing after the first pouring in L5L test

	Polar angle	Azimuth angle	Time of the IT_{max}	IT_{max}	IT_{ss}	IT_{max}/IT_{ss}
	°	°	s	°C	°C	-
IT1	0	0	63	47.6	15.8	3
IT2	30	22.5	10	90.9	17.6	5.2
IT3		112.5	17	86.7	32.7	2.7
IT4		202.5	9	114	18.8	6.1
IT5		292.5	5	52.8	15.8	3.3
IT6	51	22.5	126	60.7	31	2
IT8		202.5	182	62.5	37.6	1.7
IT9		292.5	332	64.3	36.9	1.7
IT10	65	22.5	496	72.1	49.9	1.4
IT11		112.5	538	83	60.6	1.4
IT12		202.5	636	90.3	66.7	1.4
IT13		292.5	559	104.6	75.5	1.4

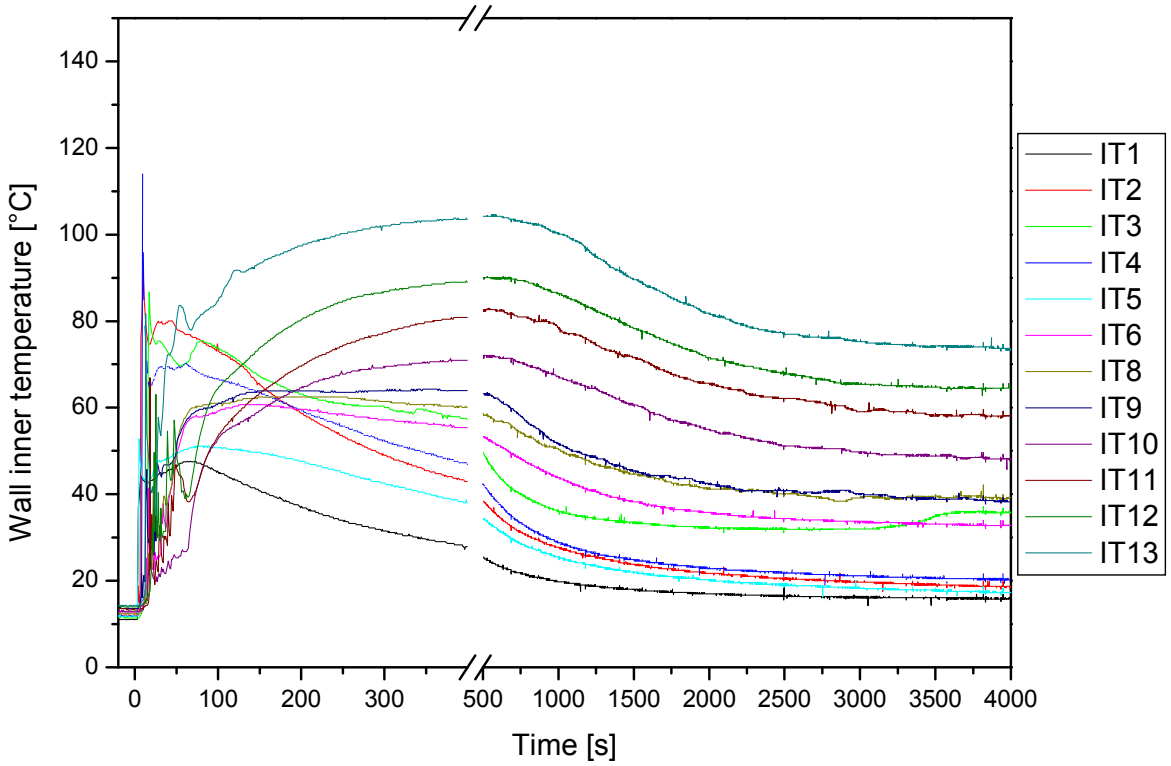

Figure 49: Transient wall inner temperature after the first pouring in L5L

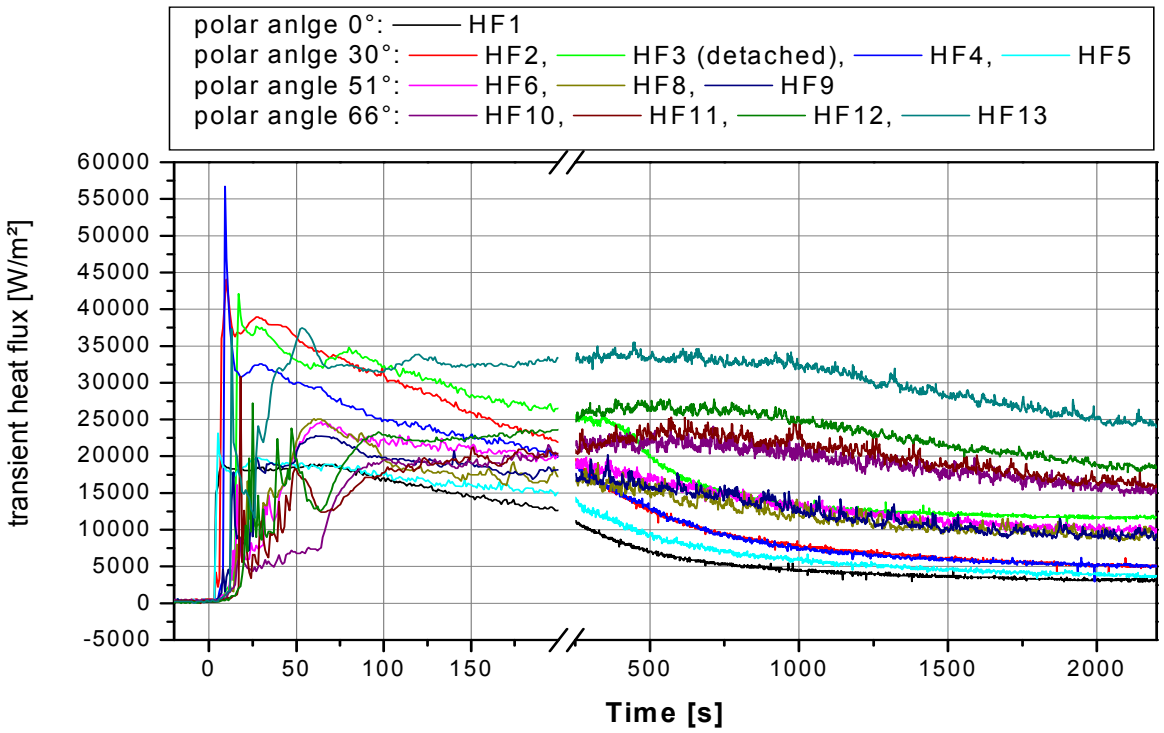

Figure 50: Transient heat flux after the first melt release

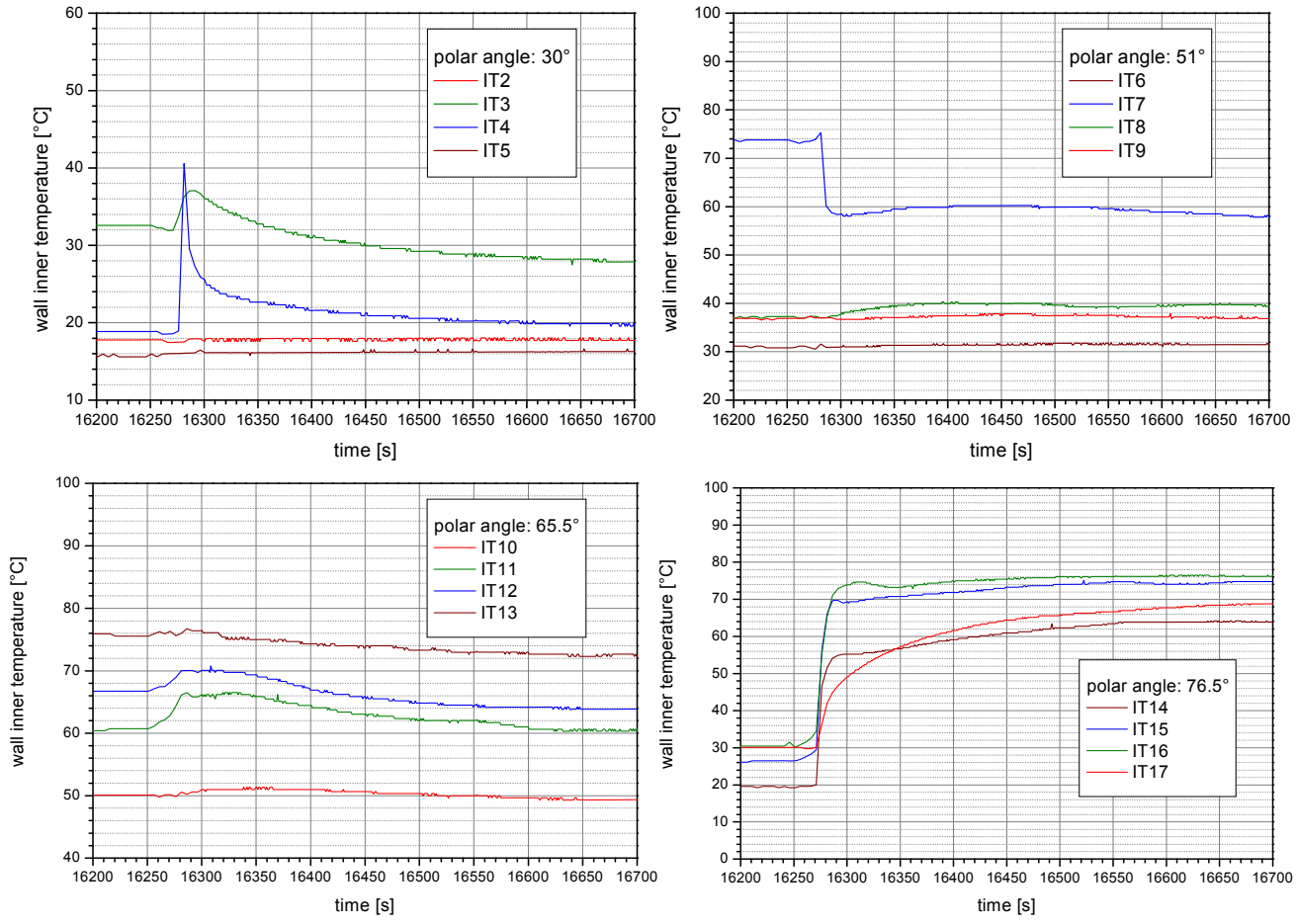

Figure 51: Wall inner temperatures after the second melt pouring at 16248 s in LIVE-L5L

The response of wall inner temperature from the beginning of the second melt release is shown in Figure 51. The strong responses of IT4 at 30° and IT7 at 51° implied the hot melt penetration to the crust/vessel interface. At the position without melt penetration, the vessel inner wall temperature under the original melt surface responded only slightly, whereas above the melt surface during the first pouring, the IT temperatures increased promptly and reached their steady temperature within 8 minutes.

6.5.3 Heat balance at steady state in LIVE-L5L

The calculation method of the heat flux through vessel wall under the melt surface Q_{wall} and the heat removed by water Q_{water} are described in Section 4.4. But the heat flux zone areas in L5L were different to L4 test and were also different during L5L test after the first melt pouring and the second melt pouring. The geometries of the melt pool after the first and the second pouring are given in Table 23.

The heat balance during L5L test is shown in Table 24.. During 18 kW, about 80 % of the heating power was transferred through the wall under the melt surface. This ratio decreased in low power density. During 5 kW heating power only about 60% of the heating power was transferred through the wall under the melt surface. The Q_{water} corresponded well with Q_{wall} in high power density and was higher than Q_{wall} in low power density. Since Q_{water} removed the heat through the wall both below and above the melt surface, the higher value of Q_{water} during low heat generation indicates that the fraction of heat through the wall above the melt surface increased in the low heat density. Some important heat transfer parameters in L5L tests are given in Table 24

Table 23: Geometries of melt pool after the first and the second melt pouring in L5L test

	IT/OT Nr.	**Zone upper surface to bottom [mm]**	**Height of zone [mm]**	**Zone inner surface area A_i [m²]**
After the 1. pouring				
Zone 1	1	32.5	32.5	0.1014
Zone 2	2-5	124	91.5	0.2855
Zone 3	6-9	236.5	112.5	0.3510
Zone 4	10-13	310	73.5	0.2293
Zone 5	14-17	496.6	186.6	0.5822
After the 2. pouring				
Zone 1	1	32.5	32.5	0.1014
Zone 2	2-5	124	91.5	0.2855
Zone 3	6-9	236.5	112.5	0.3510
Zone 4	10-13	335	98.5	0.3073
Zone 5	14-17	431	96	0.2995

Table 24: L5L heat transfer parameters

heating power, kW	1. pou-ring 10 kW.	2. pouring 18 kW-I	10 kW-I	5 kW	10 kW-II	18 kW-II
T_{mean}, °C	310.6	323.2	305.2	289.8	305.8	323.1
T_{max}, °C	320.8	331.3	309	290.7	309	330.7
T_{int}, °C	283.2	282.8	281.2	279.2	280.7	283.4
$Q_{heating}$, W	9959	18088	9967	4999	10013	18066
$Q_{wall,}$ W	7701	14661	7425	2971	7412	14061
$Q_{wall}/Q_{heating}$, -	0.77	0.81	0.73	0.59	0.74	0.78
Power density, W/m³	84008	87970	48384	27267	48608	87701
$q_{dn\ mean}$, W/m²	7960	10900	5514	2206	5504	10442
α, m²/s	1.67E-06	1.56E-06	1.71E-06	1.83E-06	1.70E-06	1.57E-06
Pr	9.9	9.3	10.1	10.1	10.1	9.3
Nu and Ra, L=vessel height						
Nu_{dn}	154	227	196	187	192	221
Ra_i	7.34E+12	4.29E+13	2.14E+13	9.91E+12	2.16E+13	4.30E+13

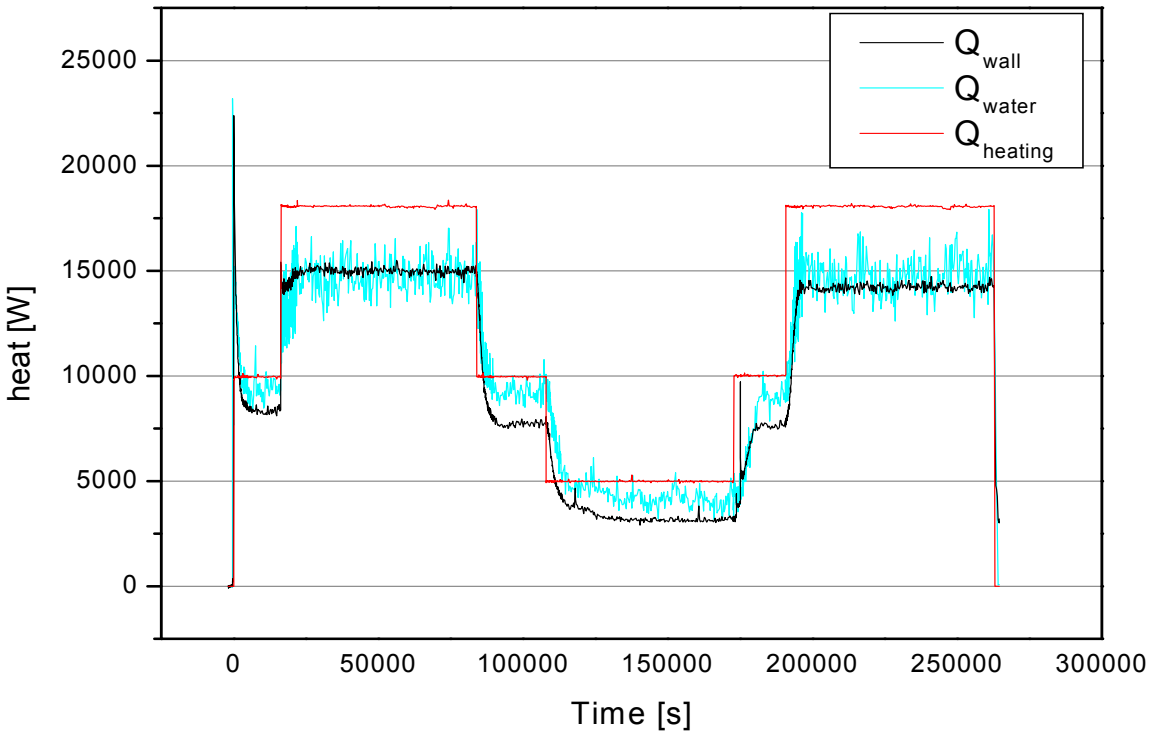

Figure 52: Heat balance among heat transfer through wall under melt surface, heat removal of cooling water and heating power in LIVE-L5L test

6.6 Post test analysis of LIVE-L5L

After the extraction of the melt and after the cool down of the test facility, the upper lid was disassembled. In Figure 53 a view of the test vessel after removing of the top lid is shown. 225.5 kg of melt was released during the first melt pouring and 163.5 kg was released during the second melt pouring. At the end of the test 351 kg of melt was extracted back into the heating furnace. Thus the crust formed on the vessel wall at the end of the test was 38 kg, which corresponds to 9.7 % of the total melt mass in the test vessel.

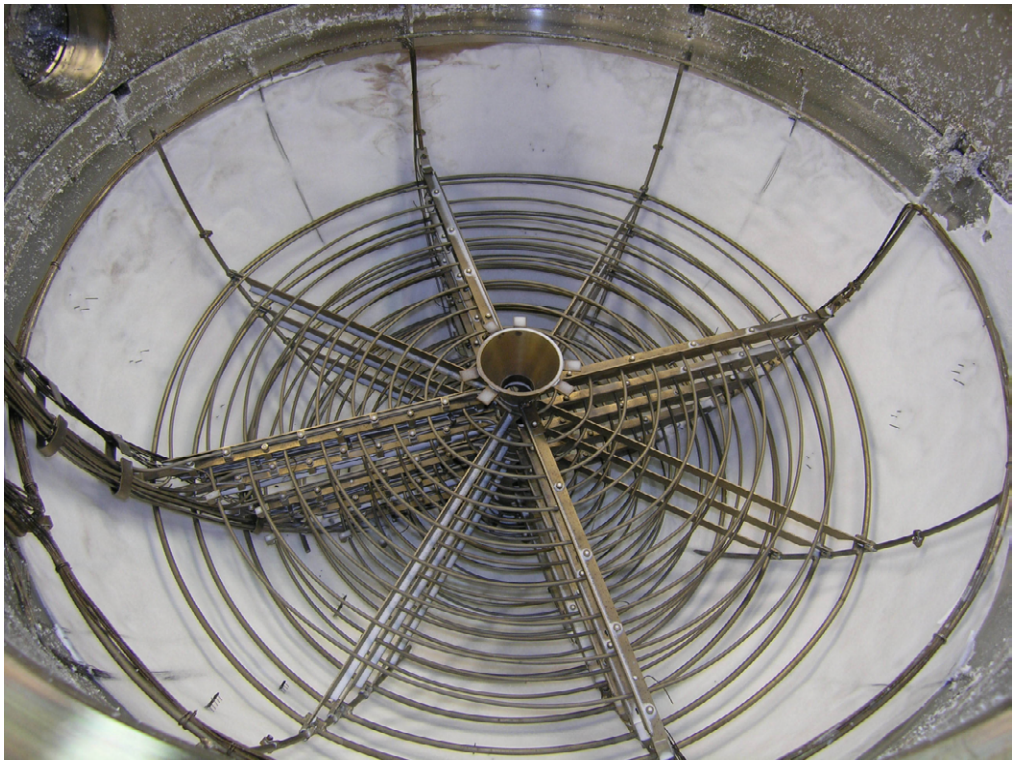

Figure 53: A view of the vessel after disassembly of the lid in LIVE-L5L

6.6.1 Bulk melt composition in LIVE-L5L

Melt samples were taken from the original melt, from the melt pool during the steady states of 6 heat generation rates and from the different location of the crust on the vessel wall after the test. The liquidus temperatures of the melt samples were analysed with melt temperature testing facility “Optimelt” [14]. The liquidus temperatures and the KNO_3 concentration of the melt samples are given in Table 25. The melt liquidus temperature is a parameter of melt composition. A decreasing liquidus temperature implies the decrease of KNO_3 concentration due to the substantive growth of crust. The melt liquidus temperature is also the crust/melt interface temperature during the steady states, thus the melt/crust interface temperature decreased about 5°C from 18 kW to 5 kW heating power.

Table 25: Melt pool liquidus temperature and composition during the steady states in L5L

Melt sample	**Heating period**	**$T_{\_liquidus}$, °C**	**KNO_3-mole %**
Nr. 0	Original melt, before the pouring	284.6	80.08
Nr. 1	1.pouring, 10 kW, steady state	283.2	79.83
Nr. 2	2. pouring, 18 kW-I	282.8	79.78
Nr. 3	10 kW-I	281.2	79.65
Nr. 4	5 kW	279.2	79.29
Nr. 5	10 kW-II	280.7	79.50
Nr.6	18 kW-II	283.4	79.90
Nr.8	Post test, top part of crust	288.0	crust: 81.3 melt pool: 79.8
Nr. 9	Post test, middle part of crust	288.0	crust: 81.3 melt pool: 79.8

6.6.2 Crust growth characters

The crust growth characters (crust thickness development, crust growth rate and temperature gradient in the crust) at polar angle 37.5°(CT1/CT4) and 52.9° (CT2) after melt pouring was determined based on the crust temperature measurement (section 2.4) The temperatures in the crust layer and in the melt near the crust front at the position of 37.6°, 52.9° and 66.9° are shown in Figure C- 7 to Figure C- 9. Crust thickness progression is determined by the method described in [14].

Table 26 givens crust thickness, crust growth rate and crust temperature gradient G at the position of 52.9° and 37.6°. The crust thickness development and crust growth rate are also shown in Figure 54 and Figure 55. According to the criterion of the consititional supercooling condition of this simulant material: $G/R<96800$ K·s/mm^2 [14], the time points of the end of the constitutional supercooling were between 3000 s and 4000 s at 52.9° and 5000 s at 37.6°. At these times, the crust thickness was at least 93% of the final thickness at 52.9° and 98% at 37.6°. The time period of the constitutional supercooling at polar angle of 66.9° (CT3) can not be exactly calculated. From the crust temperature shown in Figure 56, this time period was about 2000 s. At this position the solidification condition was strongly influenced by the stabilization of local melt temperature after melt pouring or changing of heating density. As shown in the Figure 36, the upper part of the melt need longer time to reach stable temperature as the lower part of melt pool does. In addition, large difference between wall inner temperature and crust outer temperature is observed at CT3 (Figure 56). This implies the existence of a gap between the crust and vessel inner wall surface.

The strong variation of the crust growth rate at the initial period is noticeable (Figure 55). This phenomenon could be a result of the varying concentration of low-melting component $NaNO_3$ in the local melt ahead of the crust front. A periodically fast solidification led to the accumulation of $NaNO_3$ in the local melt. When the enriched $NaNO_3$ can not be efficient transported to the bulk melt pool, the local melt liquidus temperature become consequently lower and the

crust growth slows down. An oscillation of crust growth rate could be established due to the interaction among cooling, crust growth and the outwards transport of $NaNO_3$.

Table 26: Crust thickness z, crust growth rate R and crust temperature gradient G after melt pouring at polar angle 52.9° and 37.6° in L5L test

Position: CT2, polar angle 52.9°				
Time	Crust thickness, [1] Z_{min}, mm	Crust growth rate R, µm/s	Temperature gradient G, °C/mm	G/R K·s/mm^2
56	1.06	20.54	27.40	1334
142	2.83	3.38	28.22	8340
400	3.70	3.12	25.66	8233
600	4.33	6.10	23.57	3862
800	4.81	2.86	20.49	7154
960	5.95	0.78	21.71	27979
1500	6.57	0.56	21.44	38181
2000	7.88	0.46	19.53	42555
3000[1]	8.02	0.24	17.39	**72967[1]**
4000[1]	8.36	0.12	16.42	**142044[1]**
5000	8.55	0.02	15.83	949804
6000	8.58		15.59	
Position: CT1, polar angle 37.6°				
Time	Crust thickness, 1 Zmin, mm	Crust growth rate R, µm/s	Temperature gradient G, °C/mm	G/R
50	2.58	13.10	20.00	1527
250	5.20	6.72	21.50	3199
400	6.20	17.32	18.21	1051
620	10.02	6.53	24.37	3735
800	11.19	8.14	21.47	2637
1000	12.82	12.24	6.98	570
1200	15.27	3.50	6.23	1779
2000	18.07	3.33	6.30	1895
2500	19.73	1.29	6.02	4672
3000	20.38	0.80	6.05	7581
4000	21.17	0.32	9.79	30766
5000[1]	21.49	0.09	9.55	**103368[1]**
6000	21.59		9.42	

Note: [1]: time point and G/R values at which the equilibrium crust growth was reached.

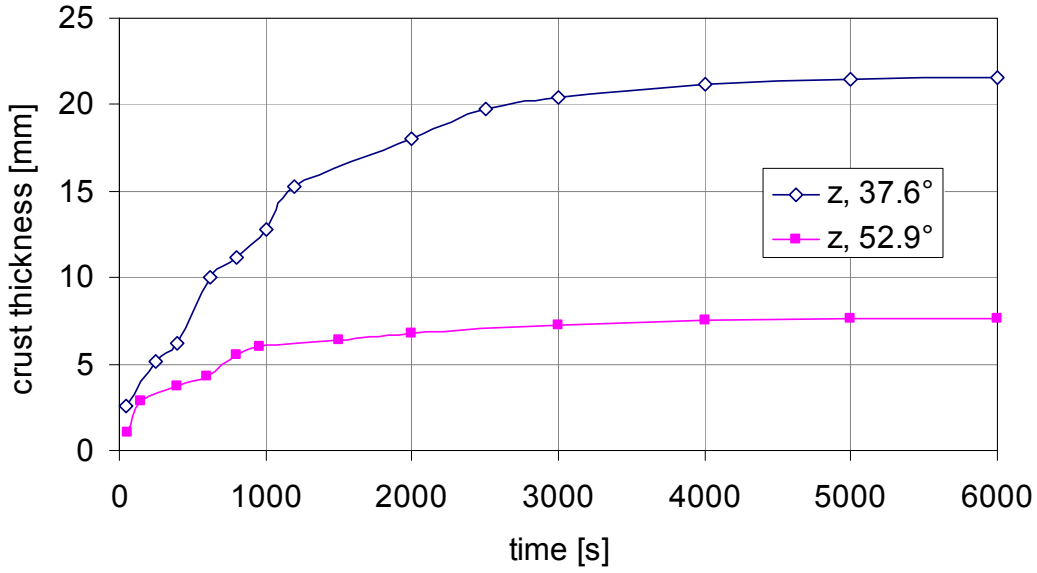

Figure 54: L5L crust thickness development at polar angle 37.6° and 52.9°

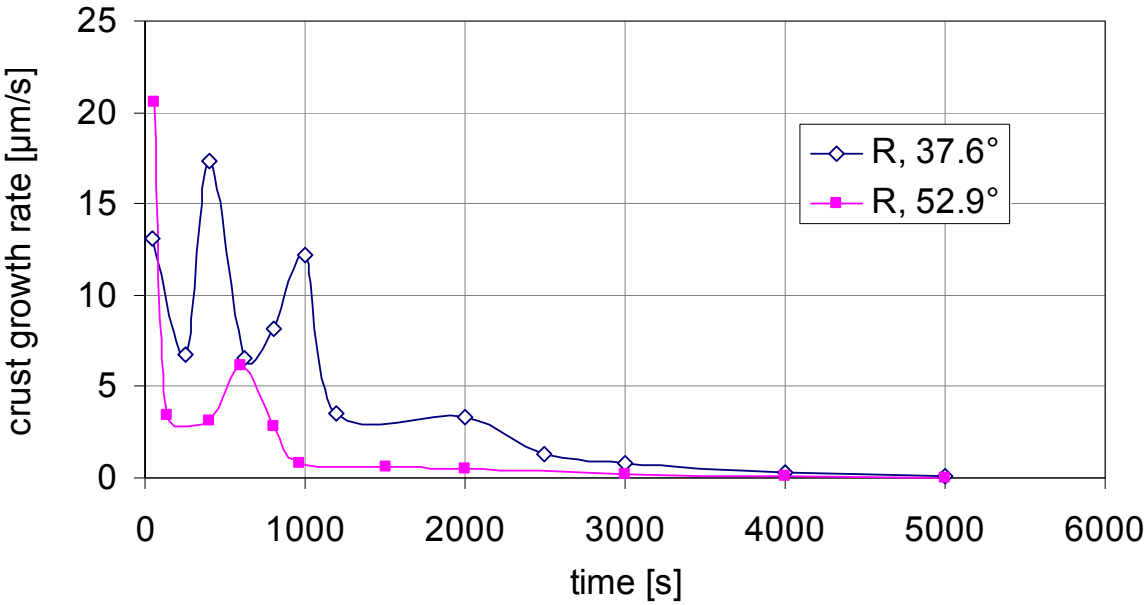

Figure 55: L5L crust growth rate at polar angle 37.6° and 52.9°

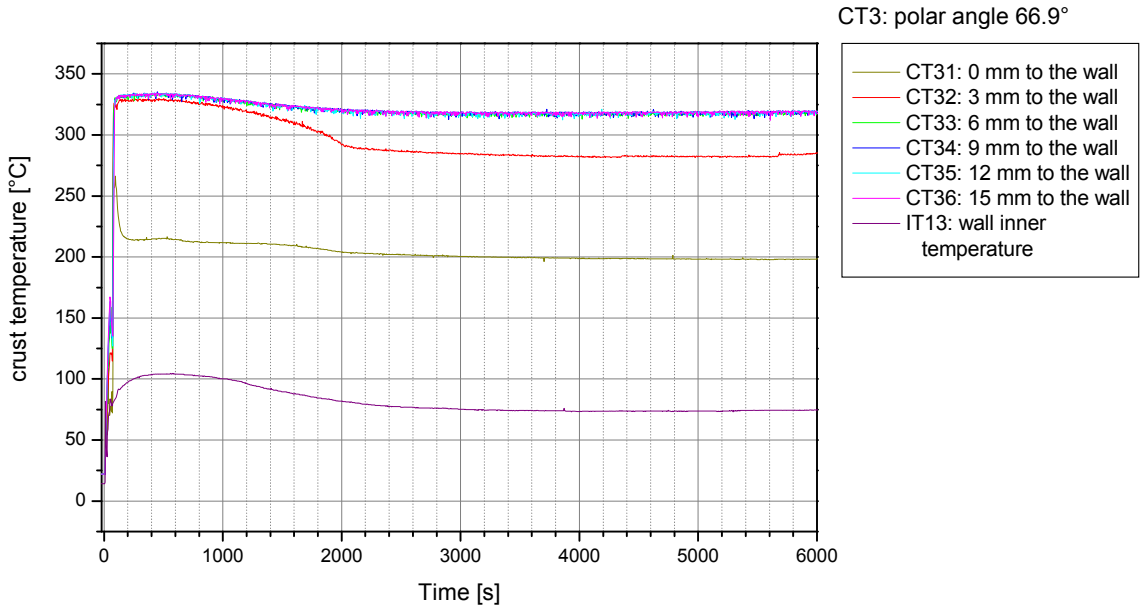

Figure 56: L5L crust temperature at the beginning of test at position of CT3, 66.9°

6.6.3 Crust thickness and crust thermal conductivity

The crust thickness correpsonding to the 18kW-II steady states was measured after the test at four azimuth angles and are given in Table 27. Figure 57 shows the crust profile at the section of 157.5°-337.5°. The increase of crust thickness during the melt extraction period was negligible. The crust was the thinnest at polar angle 60° and grew thicker from this position downwards. The pit at the vessel bottom was probably resulted by the heating plane 6, which was covered in the crust (Figure A- 10). The buildup of the crust was rather symmetric at the upper part and locally asysmetrically at the lower part, as shown in Figure 58. which was resulted by the local heating wires near or covered by the crust.

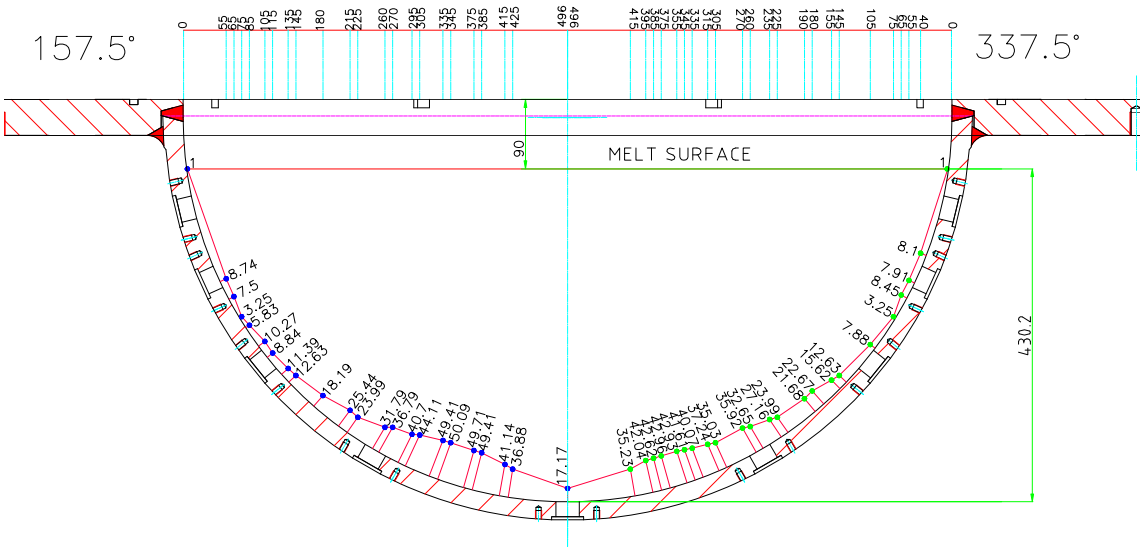

Figure 57: Post-test measurement of crust thickness of LIVE-L5L test

Table 27: LIVE-L5L crust thickness measured after the test

247.5°		67.5°		157.5°		337.5°	
Polar angle	Thickness [mm]	Polar angle	Thickness [mm]	Polar angle	Thickness [mm]	Polar angle	Thickness [mm]
82.34	1	82.34	1	82.34	1	82.34	1
68.98	8.1	68.65	7.02	64.73	8.74	68.98	8.1
64.94	9.57	64.52	7.91	61.79	7.5	64.52	7.91
62	8.54	61.38	5.6	58.58	3.25	62	8.45
59.08	5.84	59.28	6.86	56.87	5.83	58.58	3.25
56.97	6.38	53.32	9.08	53.51	10.27	53.13	7.88
53.42	9.67	48.43	14.06	51.4	8.84	46.49	12.63
48.34	13.39	45.15	15.62	48.07	11.39	45.15	15.62
46.58	13.32	36.98	29.44	46.49	12.63	41.82	22.67
45.24	16.33	34.12	31.3	41.34	18.19	40.11	21.68
41.82	22.67	26.38	44.29	36.61	25.44	34.99	23.99
40.11	21.68	23.55	43.66	34.99	23.99	33.78	27.16
37.05	30.24	20.96	46.61	30.53	31.79	30.59	32.65
34.92	23.17	18.27	46.73	29.45	36.79	29.39	35.92
33.78	27.16	15.61	46.82	26.16	40.7	24.44	35.03
30.59	32.65	12.92	44.96	24.97	44.11	23.21	37.24
29.45	36.79	10.2	39.17	21.1	49.41	20.65	40.07
26.22	41.6	0	17.17	19.77	50.09	19.38	41.61
25.02	45.02			15.71	49.71	18.11	42.93
21.1	49.41			14.37	49.41	15.47	42.96
19.77	50.09			10.24	41.14	14.15	42.62
15.74	50.67			8.88	36.88	12.84	42.04
14.34	48.44			0	17.17	10.11	35.23
13.01	47.89					0	17.17
10.22	40.16						
0	17.17						

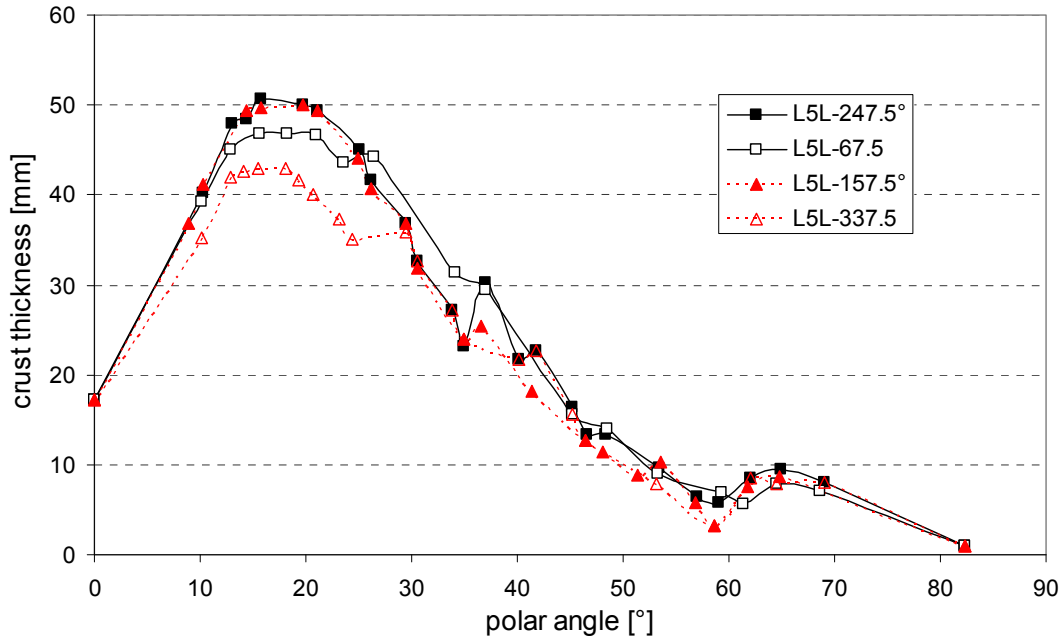

Figure 58: L5L crust thickness profiles measured after the test

The crust thickness during the test can be roughly determined at polar angles 37.6°, 52.9° and 66.9°. The determation is based on the crust temperature across the crust layer. As shown in Figure 59, the crust thickness was not always identical under some power denisty, e.g. during 18 kW-I and 18 kW-II periods. In 18 kW-II period, the decrease of crust tempreature at 0 mm at positions of 37.6° and 66.9° after crust failure (Figure C- 7 and Figure C- 9) indicates improved cooling of crust. As response the crust grew further to compensate the missing heat resistance.

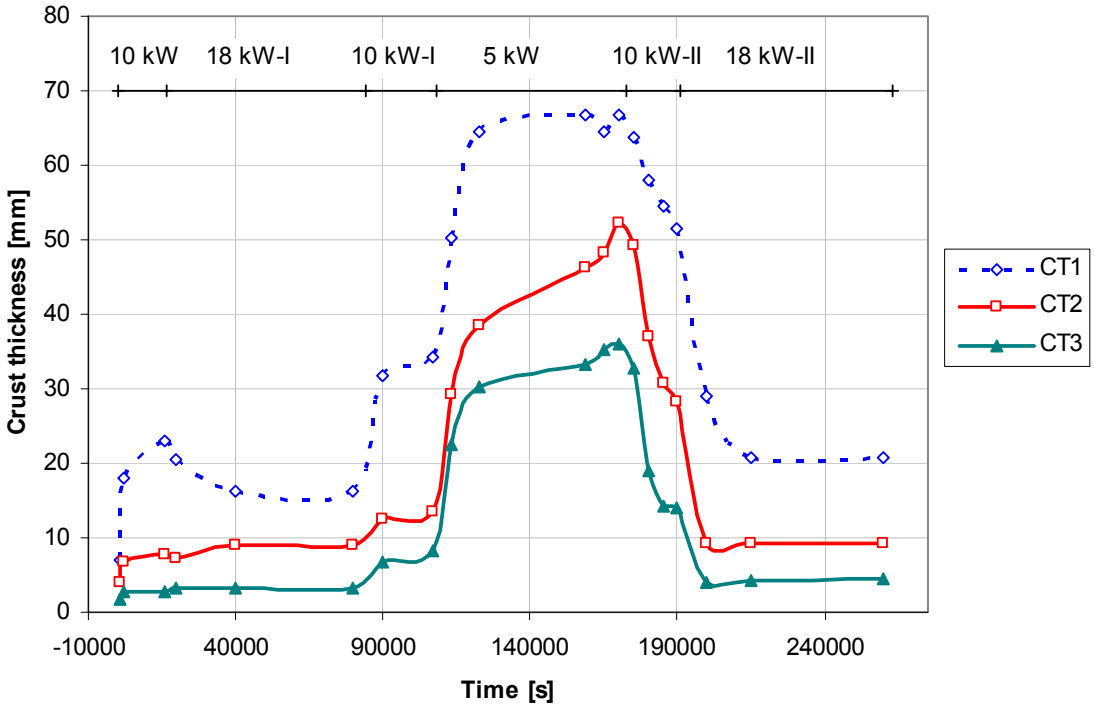

Figure 59: L5L crust thickness development during the whole test period

The crust development at CT1 and CT2 positions was not finished during the first heating period and the 10 kW-II period, implying that the thermal hydraulic steady state of the melt pool was not really reached.

The crust thermal conductivity during different heating periods was calculated according to crust temperature and local heat flux through vessel wall at the positions of CT1, CT2 and CT3. The calculated crust thermoconductivity varied during different heating periods. Also the thermoconductivity across the crust layer was not constant at the same heating power. The value ranged from 0.4 to 0.8 W/(mK). The mean value through the crust layer lied from 0.43 to 0.7 W/(mK). The lowerst heat conductivity was located at polar angle 52.9°. Figure 60 shows the crust thermal conductivity at CT1 during different power density and Figure 61 shows the value at different heights.

The accuracy of the calculated crust thermal conductivity was subjected to the deivation of heat flux level mean value (HF_{lev}), seeTable D- 2. The values during 10 kW-II are also uncertain since the thermal hydraulic steady state was not finally reached during this period. Table 28 gives some of the mean crust thermal conductivities during L5L test.

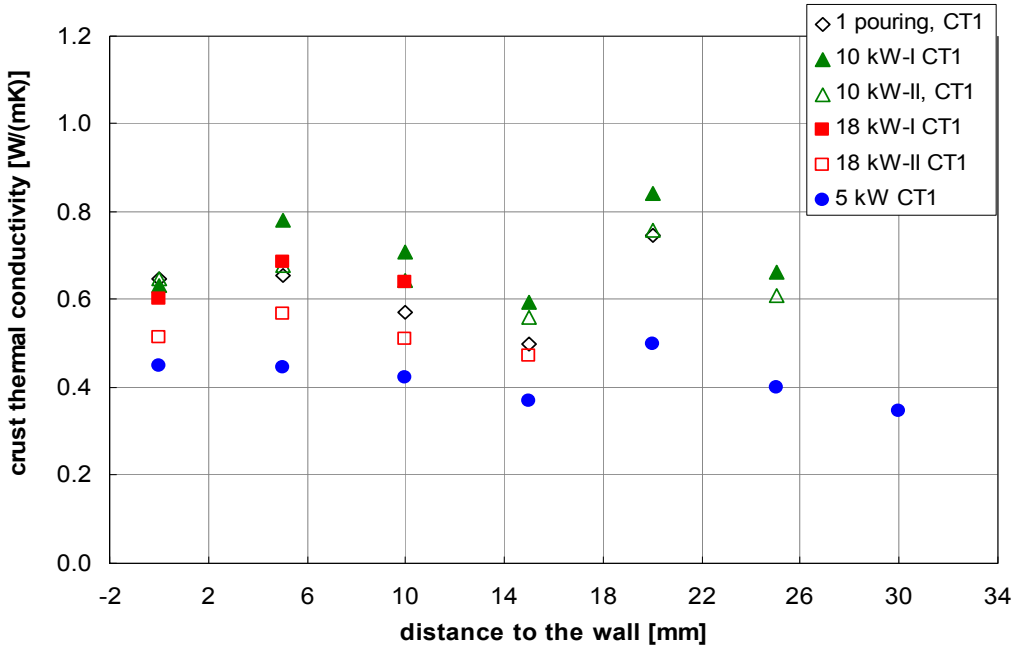

Figure 60: Crust thermal conductivity at CT1, polar angle 30° during L5L test

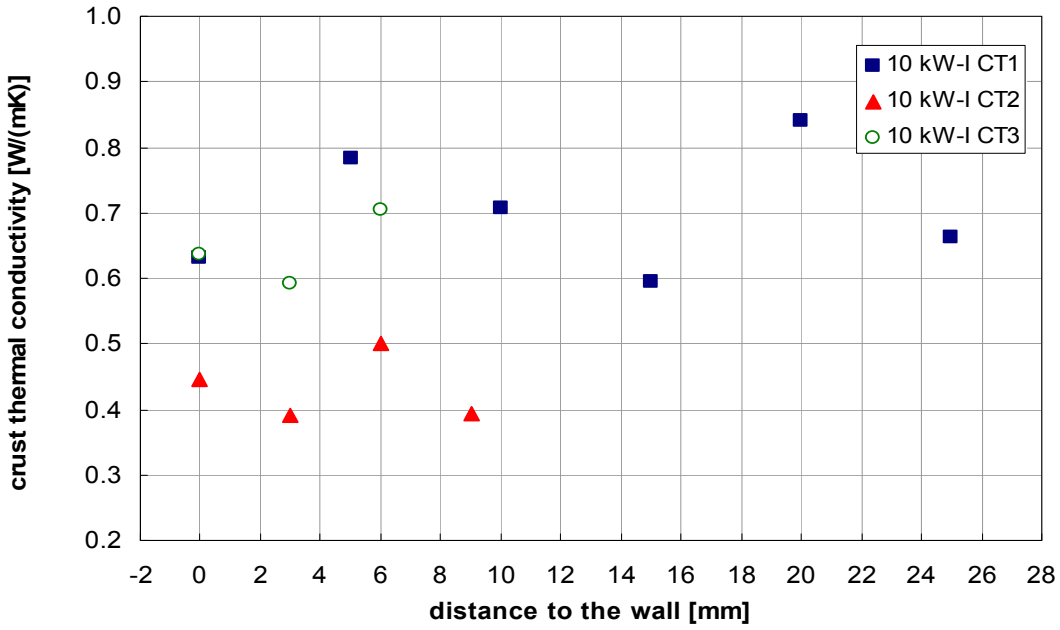

Figure 61: Crust thermal conductivity at CT1/CT4 CT2 and CT3 in L5L test

Table 28: Mean thermal conductivity through crust during L5L test

	Polar angle	1. pouring	18 kW-I	10 kW-I	18 kW-II
CT1	37.6°	0.585	0.693	0.640	0.513
CT2	52.9°	0.523	0.428	0.563	0.463
CT3	66.9°	0.583	0.641	0.626	0.540

6.6.4 Crust liquidus temperature and crust composition

A piece of crust at the vessel wall was taken out after the test. There is a separable layer in 1 to 2 mm thickness between the bulk crust and the vessel wall suggesting its origin from the penetrating hot melt after the crust failure (Figure 46). Crust liquidus temperature was determined cross a 9.4 mm-thick bulk crust layer, the thickest position of the crust which can be sampled. The separable 2 mm- thick crust layer was analysed as whole. Table 29 gives the crust liquidus temperature and corresponding KNO_3 concentration according to data in Table 1. For the bulk crust the distance of 0 mm to the wall is the crust surface to the vessel wall, 9.4 mm is the crust surface to the melt. The crust liquidus temperature increases from the wall/crust interface to the crust/melt interface, implying the solidification began from strong sub-cooling condition and ended at the equilibrium solidification. The liquidus temperature of the separable layer agreed well with the liquid melt liquidus temperature, which is also evidence that this crust layer originated from the hot melt penetration.

Table 29: L5L crust liquidus temperature measured by Optimelt

Samples	Distance to the wall	T_{liq}	KNO_3 concentration
9.4 mm crust	**mm**	**°C**	**mol%**
2 mm separable layer	Whole layer	283	79.6
Bulk crust layer	0	282.4	79.4
	3	292.1	82.5
	6	311.4	90.6
	9.4	319	94.0

7 Comparison of test results of LIVE 4 and LIVE-L5L

LIVE 4 and LIVE L5L tests were performed under similar test conditions: in both tests there were heating periods in the order of 18 kW, 10 kW, 5 kW and 10 kW, and the melt volume and cooling water flow rate during these heating periods were comparable. Therefore the melt temperature, heat flux distribution and crust behavior are compared during these heating periods. The main difference of LIVE L5L to LIVE L4 test is that in L5L test the melt was poured in two charges. 70% of the total melt amount (120 l) was discharged during the first pouring and 30% of the melt (90 l) was discharged during the second pouring. In L4 test the total amount of 210 l was discharged only in one melt pour performance. Besides in L4 test the heating power in the last period was 15 kW due to the failure of one heating plane.

7.1 Melt temperature

The melt temperature distribution and the global mean temperature during same heating power generation was identical during one test and also between the two tests. These cases are 18 kW and 10 kW heating periods in the two tests. Table 30 gives the melt temperatures at three heights and the global mean temperature. In L5L test melt temperatures above 270 mm were obtained by the crust detection lance and some of these values are also shown in Table 30. Some deviations are shown during 5 kW heating period. The heating power was so low that the melt pool temperatures were only slightly above the melt/crust interface temperature 284°C. Therefore the heat transfer regime in 5 kW was different as in higher heating power generation rate.

Table 30: Comparison of melt temperature in L4 and L5L test

	Height	Power				
	[mm]	18kW-I	10kW-I	5kW	10kW-II	18kW-II
L4	70	298.1	292.6	285.0	292.6	
	170	314.3	300.8	288.1	300.7	
	270	329.8	310.1	292.6	309.9	
	mean	323.7	306.5	290.8	306.4	
L5L	70	297.1	290.5	282.5	291.5	297.4
	170	313.0	299.2	287.6	300.2	313.1
	270	328.5	308.9	291.9	309.6	328.6
	301	329.5	308.0	289.6	308.0	329.0
	431	331.3	308.6	284.7	307.6	330.4
	mean	323.2	305.2	289.8	305.8	323.1

The good agreement of the melt temperature distribution in same power density allows reliable prediction of the melt temperature in dependence of power density. Table 31 shows the dimensionless melt temperature in terms of $(T-T_{int})/(T_{mean}-T_{int})$, whereas the T_{int} is the interface temperature at crust/melt boundary and T_{mean} is the melt pool global mean temperature. Figure 62 shows that the dimensionless melt temperature is comparable and independent on the power desity. In the lower part of the pool the temperature was stratified and in the upper part the melt the temperature was homogenous. The transition of the two parts locates at the height of about 270 mm, also 0.54 of the vessel radius. The maximum melt temperature locates In the upper part of the pool and is about 1.1 to 1.2 times of the global mean temperature.

Table 31: Dimensionless melt temperature distribution $(T-T_{int})/(T_{mean}-T_{int})$ in L4 and L5L

	$(T-T_{int})/(T_{mean}-T_{int})$			
Height/Vessel radius	18kW-I	10kW-I	10kW-II	18kW-II
	LIVE L4			
0.14	0.35	0.38	0.38	
0.34	0.76	0.75	0.74	
0.54	1.15	1.16	1.16	
	LIVE L5L			
0.14	0.33	0.31	0.35	0.34
0.34	0.74	0.72	0.74	0.74
0.54	1.14	1.18	1.17	1.14
0.61	1.16	1.13	1.10	1.15
0.87	1.21	1.16	1.08	1.19

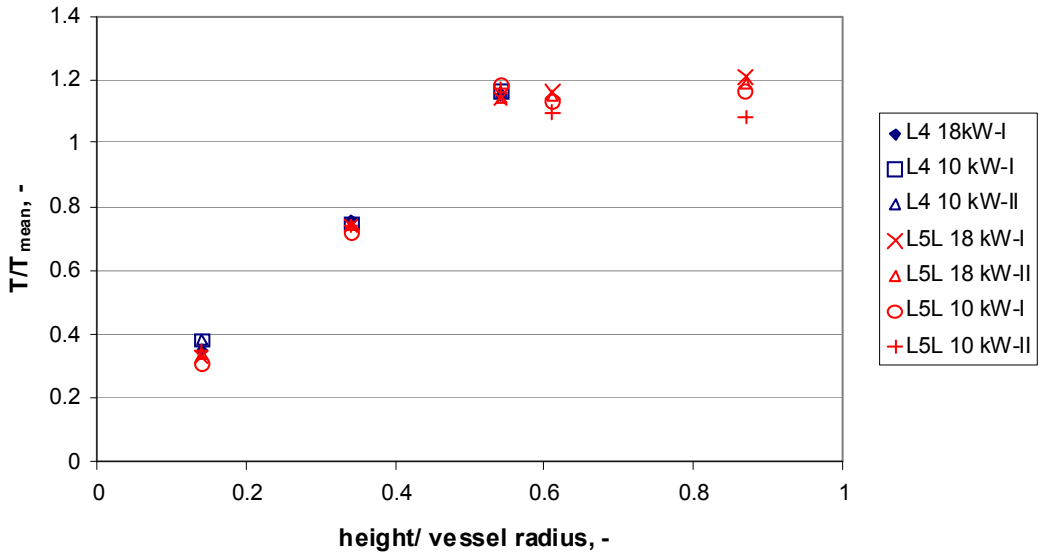

Figure 62: Dimensionless melt temperature distribution in L4 and L5L tests

7.2 Heat transfer through the wall

The heat flux through the vessel wall during heating periods of 18 kW and 10 kW in the two tests are compared in Table 32. The normalized (the ratio of local heat flux to global mean heat fluxes, q/q_{mean}) are also given. The values of q/q_{mean} of 18 kW and 10 kW heating periods agree very well at polar angle 65.5° and 76.5° The deviation turns larger from 51° to the vessel bottom (polar angle 0°).

Table 32: Vertical heat flux in LIVE L4 and LIVE L5L

Polar angle °	L4 18kW-I	L4 10kW-I	L4 10kW-II	L5 18kW-I	L5 18kW-II	L5 10kW-I	L5 10kW-II
	q [W/m²]						
0	3748	3637	3437	2963	2779	2698	2555
30	2366	1360	1612	3546	3091	2895	2316
51	8718	3875	3915	9329	8226	4225	3285
65.5	16031	8232	7114	15714	14658	7649	7862
76.5	18485	9458	9480	18116	18050	8748	9533
q_{mean}	10759	5528	5403	11038	10383	5617	5462
	q/q_{mean} [-]						
0	0.348	0.658	0.636	0.268	0.268	0.480	0.468
30	0.220	0.246	0.298	0.321	0.298	0.515	0.424
51	0.810	0.701	0.725	0.845	0.792	0.752	0.601
65.5	1.490	1.489	1.317	1.424	1.412	1.362	1.439
76.5	1.718	1.711	1.754	1.641	1.738	1.557	1.745

The heat flux creases significantly from polar angle 30° upwards to the melt top surface. The maximum heat flux during the steady states locates near the melt top surface and is about 1.7 times of its global mean value.

The highest transient IT temperature and heat flux occurs at polar angle 30° during the melt pouring, however it disappears also quickly. A long sustaining high melt temperature and heat flux occurs at polar angle 65.5° during melt pouring and the period short after. At this position, the heat flux reaches its maximum value at 500 to 800 seconds after the initiation of melt pouring and the transient value is about twice of its steady state value.

7.3 Crust behaviour

The crust behaviour in concern of crust thickness and the general thermal conductivity cross a crust layer are compared between some heating periods in L4 and L5L tests. As described in the single test results of L4 and L5L, the crust thickness was strongly influenced by events of hot melt penetration and the gap formation between crust and vessel wall. If the gap is filled with solidified melt after the event, the total heat transfer through the crust and vessel

wall is improved. As consequence the crust grows further to compensate the loss of the total thermal resistance. This can be the main reason that the crust layer in L4 test 10kW-II period was much thicker than the 10kW-I period in the same test. The same case applies also to the crust layer in 18kW-I and 18kW-II during L5L test. Bearing this effect on the changing crust thickness, the crust thickness was comparable between L4 and L5L test.

Table 33: Comparison of crust thickness and crust thermal conductivity in L4 and L5L

Polar angle	L4				L5L			
	18kW-I	10kW-I	10kW-II	5kW	18kW-I	18kW-II	10kW-I	5kW
	Crust thickness [mm]							
37	16.09	25.74	39.56	65.8	16.3	20.83	34.13	66.83
52.9	6.3	13.48	20.47	43.45	8.96	9.14	13.44	52.17
66.9	-	9.3	12.22	31.26	3.29	4.51	8.28	35.98
	Crust thermal conductivity [W/(m·K)]							
37		0.416	0.561		0.640	0.513	0.693	
52.9		0.392	0.479		0.563	0.463	0.428	
66.9		0.575	0.450		0.626	0.540	0.641	

The crust thermal conductivity of the two tests are in the range of 0.4-0.7 W/(m·K). The accuracy of the crust thermal conductivity is subjected to the deviation of heat flux level mean value, which became considerably large during low power generation (Table D- 2). In spite of the possible errors, the crust thermal conductivities at the bottom and at uppermost part were higher than the middle part of the crust layer (polar angle 52.9°).

8 Measurement uncertainties

The great part of the measurement signals in the L4 and L5L tests is temperatures. All the temperature signals given in this report were measured with Type-K NiCr/Ni thermocouples. The other directly measured signals were weight of vessel and water flow rate. The system errors of the signals including deviation of the device and deviation of the signal transmission are given in Table 34. The system error of the thermocouples lies within ±1.5 °C in the temperature range of -40 °C to 375 °C [19]. The following systematic errors the temperatures are critical for the determination of correlated parameters and were calibrated:

• the difference between the systematic errors of water inlet temperature (ZT) and water outlet temperature (AT) for the calculation of $Q_{water,}$ ZT and AT were calibrated with a Type-A PT100 resistance thermometer whose tolerance is ±0.17 °C in the working temperature [17]. The calibration equations were given in Eq(6) and Eq(7).

• the difference between the systematic errors of wall inner temperatures (IT) and wall outer temperature (OT) for the calculation of local heat transfer through vessel wall (HF). The offset of IT and OT was calculated in a pretest under isothermal condition and was compensated during the calculation of heat flux.

Besides the system error, standard deviation of standard error during the measurement according to DIN 1319-3 [20] in L4 and L5L tests are analyzed in Table D- 1 and Table D- 2 respectively. The directly measured signals are the average of 25 measurements within 2 minutes during the thermal hydraulic steady states except the ones from the crust detection lance. The mean of MT, CT, IT and OT is the mean deviation or error of the thermocouples with the same designations, e.g. “MT mean” implies the mean value of the 36 thermocouples from MT1 to MT36. Low deviation and error was detected in MT. In addition of the generous CT mean, which includes the thermocouples in the crust as well as in the melt near the crust/melt interface, the deviation of the CT thermocouples in the crust in also calculated. The heat flux of a horizontal heating zone is the average of a number of local measurements; their standard errors are also listed in the table.

The signals with little variation (relative variation < 1% and relative error <0.1%) are MT, CT, IT and heating power. The signals with moderate deviation (relative variation < 5% and relative error <1%) and error are OT, AT, ZT and DF. The heat flux at a local position has considerable deviation due to the large deviation of (IT-OT) in comparison with IT. Even larger deviation is found in the HF_{lev}, the horizontally averaged value at certain vessel height. However, this large deviation is not only a sign of measurement uncertainty, but also an implication of the asymmetric distribution of heat flux at one horizontal level.

The crust thickness measured after the test is the total thickness of the crust layer and the gap at the wall/crust interface. The deviation of the measurement lies < ±0.2 mm. More uncertainty of the crust thickness could lie in the varying thickness of the gap during test and after test, for which no suitable measuring method can obtain exact value at present.

Table 34: system errors of the signal measured in L4 and L5L tests

Signal designation	**Type**	**Device (±)**	**Transmission (±)**
Thermocouples: MT, LT, CT, IT, OT	Type-K NiCr/Ni	1.5 °C	0.50%
Resistance thermometer PT	Type A	0.17 °C	0.50%
Weight cell	MVD2510	<0.2 %	0.10%
Water flow meter , DF	IFM 1080	1.00%	0.05%
IT-OT [1]		0	0.00%
water outlet temperature AT[1]	Type-K NiCr/Ni Thermocouple	0	0.00%
water inlet temperature ZT[1]	Type-K NiCr/Ni Thermocouple	0	0.00%

Note: 1. The system errors were either calibrated or be compensated in the calculation.

9 Simulation of the LIVE-L4 with the CONV code

9.1 The CONV code

CONV is 2D/3D thermohydraulic CFD code [22],[23] for the simulation of heat transfer due to conduction and convection in complex geometry, crust formation, etc. It was developed at IBRAE (Nuclear Safety Institute of Russian Academy of Sciences, Moscow) within the framework of the International RASPLAV project [24] to validate the concept of melt confinement in reactor pressure vessel. Thereupon it was additionally improved within the ISTC #2936 Project (Modelling of Reactor Core Behavior under Severe Accident Conditions. Melt Formation, Relocation and Evolution of Molten Pool) and validated on numerous thermohydraulic tests. Currently CONV code is under further development within on-going ISTC #3876 Project (Thermo-Hydraulics of Oxidising Melt in Severe Accidents).

For the modelling of heat generating viscous liquid in a gravity field with consideration of the buoyancy force in a Bousinesque approximation the efficient difference scheme is applied to solve unsteady 2D/3D Navier-Stokes equations in natural "velocity-pressure" variables on fully staggered orthogonal grids for Cartesian coordinates. For the modeling of turbulence the algebraic turbulent models were implemented in the code.

The CONV code has been qualified against the available analytical solutions [25][26] and well-instrumented and well-defined experiments [27]. Recently CONV code was successfully applied to the simulation of the FSt4 LIVE test with water as the working liquid [28]-[30].

9.2 Calculations

9.2.1 Task formulation

One of the objectives of the calculations was to check if the LIVE circular volumetric heating systems adequately represents the homogeneous heat generation in the liquid pool. Since it cannot be demonstrated experimentally, one of the possible ways is to use the advanced computer tools, like CONV. Therefore, two calculations were performed with CONV code:

a) assuming the homogeneous heat generation in the whole pool volume and

b) with heat generation using the spiral heaters.

Another objective was to consider the ability of the CONV code to describe crust formation process during different phases of the test.

9.2.2 Nodalization scheme

Due to axial symmetry of the facility the 2D CONV version with orthogonal curvi-linear grid was used in the calculations. The grid was condensed near the liquid/solid boundary and near the upper surface of the liquid (Figure E- 1). In the calculation with homogeneous heat generation the nodalization 101×101 was applied; in the calculation with accounting for the

heaters the nodalization 201×201 was used in order to describe in more details the liquid flow and heat exchange in the vicinity of the heaters.

9.2.3 Boundary conditions

Temperatures measured at the outside vessel surface were used as the boundary conditions for this part of the considered calculation domain surface. The values of the outside temperature lied in the interval 17º - 45 ºC depending on the polar angle and the phase of the test.

As for the upper surface, here the estimated upward heat flux was used as the boundary condition. The hemispherical vessel was covered with a massive metal plate; during the test the space between the upper melt surface and the plate was filled with nitrogen thus providing rather effective heat isolation. The heat flux through the nitrogen layer was estimated on the basis of the temperature difference between lower metal plate surface and melt bulk temperature assuming the conditions of Rayleigh-Bernard convection. The obtained value appeared to be rather low: 70-100 W/m^2. On the other hand the openings in the upper lid and shortcuts from the frenge may result in more heat flux and heat removal from the melt surface. This may be the reason of the overestimation of CONV-melt temperature in the case of heaters.

9.2.4 Temperature evolution

In Figure E- 2 to Figure E- 5 the comparison of measured and calculated temperature evolution at the designated location (polar coordinates counted out from the geometrical centre of the considered hemisphere: R = 35.8 cm, height 27 cm, φ = 50º in the bulk of liquid is given (the experimental values correspond to the average of MT29, MT30; MT31 and MT32 thermocouples readings). Generally, the calculated temperature curves look similar to the experimental one. At the designated position the calculated melt temperature in the case of the homogeneous heating is lower than the experimental value, whereas in the case of heating by the heaters the calculation overestimates the temperature (Figure E- 2and Figure E- 3).

This difference between two calculations can be explained in the following way. The total heating power in the two cases is the same, but the heat volumetric distribution is different. In the case of heating with the heaters the heat is generated only below the level of 29 cm, thus the heating density under the level of 29 cm is higher in comparison with the homogenous heating case. Consequently the melt temperature in the melt pool lower part is higher in the case of heating by heaters.

Besides difference in the generated heat distribution the heaters represent on the one hand the heat source giving rise the buoyancy driven motion of liquid in the vicinity of a heater, and on the other hand they represent a kind of obstacle to the large-scale motion of liquid. All these factors lead to the difference in the two cases.

As for the temperature evolution curves in the third phase of the test (Figure E- 4), the described tendency takes place here as well. However, both calculated curves lie above the experimental one. The overestimation of the two cases was more apparent since the fraction of heat loss during the 5 kW heating period of the experiment was more significant than the

value assumed in the calculation (see Table 13). Moreover the underestimation of crust thickness also leads to higher melt temperature in the calculation (see below).

9.2.5 Heat flux to the side vessel wall distribution

The comparison of the measured (at four locations) and calculated heat flux to the vessel wall at three phases of the test is given in Figure E- 6 to Figure E- 8. There is acceptable agreement between experimental data and calculation results at the first (18 kW) and the second (10 kW) phases of the test. At the same time the noticeable disagreement takes place between the measured and calculated heat fluxes at the third (5 kW) phase of the test. In the vicinity of 0º angle the experimental value is much higher than the calculated one, and at the positions between 30º and 60º the calculation results exceed the experimental values. It should be noted that the same tendency takes place also at the mentioned above first and second phases of the test, but there it does not go beyond the accepted calculation and experimental uncertainties.

Important point here is that according to the results of previously performed simulation of the LIVE FSt4 test [29], one could expect gradual increase of the heat flux to the vessel wall with the polar angle increase. In the present calculations the similar result was obtained, in obvious contradiction with the experimental data, at least at the third phase of the test in the area adjacent to the 0º angle. This discrepancy may be the result of the measurement errors of IT at the vessel lower part (see Table D- 1).

The difference between the two calculation results is quite comparable. At the lower pool angles the first (homogeneous calculation) curve exceeds the second (heaters). At the pool angle range from 20º-35º (depending on the test phase) to 65º the second calculation result exceeds the first one; at the angles above 65º one has once again opposite picture. Such heat flux distribution corresponds to the difference in heat release distribution considered in the two calculations.

Generally, the obtained results show that there is no critical difference in the heat flux distribution at the vessel wall for these two cases, indicating that the LIVE facility adequately represents thermal conditions of the homogeneously heated liquid.

9.2.6 Crust thickness

In Figure E- 9 the comparison of the calculated crust thickness at the first and third phase of the test and the experimental data is presented. One can see rather high underestimation of the crust thickness value especially at the third (5 kW) phase of the test. Obviously, this fact is directly connected with the discrepancy between the measured and calculated heat fluxes at the corresponding pool angles (Figure E- 8): the lower the heat flux, the lower the temperature of the melt and consequently, the higher the crust thickness at the considered location. From the formal point of view the crust thickness h_{cr} and the heat flux through the crust Q_{cr} are connected by the following relation:

$$Q_{cr} = \lambda_{cr} \frac{T_{cr,in} - T_{cr,out}}{h_{cr}} \quad (10)$$

where

λ_{cr} = thermal conductivity of the crust [W/m·s],

$T_{cr,in}$ = temperature of the inner surface of the crust which is in contact with the melt [K],

$T_{cr,out}$ = temperature of the outer surface of the crust which is in contact with the vessel [K].

The possible gap between the crust and vessel wall is not considered and it may affect the accuracy of the above estimation.

One can say that the calculation results with respect to heat flux distribution and crust thickness are in good correspondence with each other; the analogous experimental data also well correlate. At the same time, there is substantial disagreement between the calculation results and experimental data especially concerning crust thickness.

Due to dependence of the crust structure and porosity on cooling conditions and temperature, the thermal conductivity of the crust changes during the test (Figure 31) The original calculations were performed assuming crust thermal conductivity equal to 0.15 W/m·s. Additional calculation has been performed with crust thermal conductivity equal to 0.42 W/m·s. The calculated crust thickness curve (blue line in Figure E- 9) is located higher, but still much lower than the experimental points. So, the uncertainty in the crust thermal conductivity value cannot completely explain the disagreement between the calculation and experiment results.

Among possible reasons leading to this disagreement may be the fact that current CONV version is able to consider only eutectic composition of the melt. Thus, the effect of two-phase zone between the crust and the melt is not accounted for.

Coming back to Figure E- 9 one should pay attention to the parts of the blue curve marked with the arrows: these bents are due to the heaters presence.

In Figure E- 10 the comparison between the crust thicknesses measured at the first phase of the test and at the end of the test as well as the calculated crust thickness. At the end of the test, when the power was turned off the melt was extracted out of the vessel by the vacuum pump rather fast – during 90 seconds. Thus, post-test measurements of the crust thickness correspond to last phase of the test, when the power was close to the one in the first phase. The calculated curve lies lower the results of the measurements in correspondence with the previously discussed Figure E- 9. Noticeable is rather high difference between two experimental data sets. The different crust thickness during same heating power is mainly a result from the filling of gap at crust/vessel interface, as discussed in section 4.5.2.

10 Conclusion

LIVE-L4 and LIVE L5L were performed under similar test conditions. In both tests the melt was externally isothermally cooled by water, the top of the vessel was insulated. Non-eutectic melt in the composition of 80% KNO_3-20% $NaNO_3$ was used. The melt pool was volumetrically heated from vessel bottom to 310 mm height. The height of the melt was about 430 mm, and there were heating periods in the order of 18 kW, 10 kW, 5 kW and 10 kW. The main difference of LIVE L5L to LIVE L4 test is that in L5L test the melt was poured in two charges. 70% of the total melt amount (120 l) was discharged during the first pouring and 30% of the melt (90 l) was discharged during the second pouring. In L4 test the total amount of 210 l was discharged only in one melt pour performance. Besides in L4 test the heating power in the last period was 15 kW due to the failure of one heating plane.

The aim of the experiments is to investigate melt temperature distribution, heat flux through the wall and crust behaviors during transient states as well as steady state. In following the findings from the two experiments are generalized.

Melt transient behavior

- The melt was cooled from 342 °C to 330°C during the melt pouring period. Then the melt temperature underwent stratification in that the lower part of the melt was cooled down quickly where as at upper pool temperature arose slightly at first and then decreased to a steady value. The process of melt temperature stratification took about 2000 seconds.

- After power reduction the lower part of melt reach faster to stable temperature than the upper part of the melt.

- The highest heat flux took place during melt pouring period at the lower part of the vessel wall. The peak value at this location reduced quickly to stable one after melt pouring. In contrast high transient heat flux at the upper part of vessel wall appeared in 4 minutes after the melt pouring and it lasted longer time (2 to 5 minutes) before it decreased again.

- When melt pouring took place more than one time, the crust was strongly subjected to thermal shock with the response of gap formation at crust/wall interface and crust cracking. The consequences are hot melt penetration to the gap and the increase of crust thickness.

Steady state behavior

- Within the melt height of 430 mm, there was a stratified zone up to 270 mm height and above it a homogenous melt layer.

- Expect very lower heating power, in the both test it was 5 kW, the vertical melt temperature distribution described as $(T-T_{int})/(T_{mean}-T_{int})$ was identical between independent of power density. The maximum value was about 1.2 and located near the melt surface,

- The normalized heat flux distribution q/q_{mean}, through vessel wall was also well comparable among different power densities. The maximum heat flux located near melt top surface and was about 1.7 times of its global mean heat flux q_{mean}.

- Higher power density leads to a high fraction of the internal heat removed through vessel wall under the melt surface.

- The error of heat flux at vessel bottom till polar angle 30° was noticeable large, whereas the heat flux at the upper part of the vessel cam be more precisely determined.

- The internal Ra was ranged from 1.0 E+13 to 4.2 E+13 from 5 kW to 18 kW with the melt height of 430 mm as the characteristic length. The Nu of the heat transfer through the spherical vessel wall was about 230 at 18 kW.

- At the melt surface the hot melt rose up in the middle area, drifted to the wall and sunk downwards alone vessel wall. The motion velocity of the melt surface was about 2.0 cm/s at the radius 70 mm and reduced slightly to 1.3 near the vessel wall.

Crust behavior

- The crust formed at the vessel wall was symmetric at the upper part and partially asymmetric at the lower part due to the local influence of heating wires

- Gap formation at the crust/wall interface was generally observed. Without the gap the crust should be thicker.

- More times of melt pouring and heating power transition facilitate crust cracking and hot melt penetration to the at crust/melt interface. As consequence the crust become thicker after the events.

- The time periods of the constitutional supercooling condition, in which the mushy zone exists, was about 3000-4000 s at polar angle 53° and about 5000 s at 37.6°. These time periods were strongly influenced by the local melt temperature progression after melt pouring.

- The crust composition and liquidus temperature varied considerately cross the crust layer, which is a result of the interaction among cooling, solidification rate and $NaNO_3$ diffusion rate.

- The crust thermal conductivity reflects the solidification process of the melt and the value is ranged from 0.4 to 0.7 W/(mK).

LIVE L-4 test simulation with CONV

The calculations for the LIVE L-4 experiment were carried out with the CFD code CONV. Two calculations have been performed:

i) with assuming homogeneous heat generation in the liquid and

ii) with accounting for wire heaters.

- The melt temperature at the location near the up-most heating plane was calculated. Though the results of calculations demonstrate satisfactory agreement with the experimental measurements, in the first case the temperature were underestimated. In the second case the code tends to overestimate the temperatures. This may be explained by the difference of the generated heat distribution in the two cases.

- The calculated values of the heat flux through the vessel wall are higher in the case with heaters in the angle range 25-65° and lower at the angles above 65° compared to the case with homogeneous heating due to the difference of the generated heat distribution in the two cases. However, taking into account the experimental uncertainties in determination of the heat flux, it can be concluded that the LIVE facility adequately represents thermal conditions of the homogeneously heated liquid.

- The obtained discrepancy between calculated and measured heat fluxes at the 5 kW phase of the test in the area adjacent to the 0º angle may be the result of the measurement errors of IT at the vessel lower part.

- The code substantially underestimated the crust thickness in comparison with the experimental data. Due to dependence of the crust structure and porosity on cooling conditions and temperature, the thermal conductivity of the crust changes during the test and that can affect the results. Among other reasons leading to this disagreement may be the fact that current CONV version is able to consider only eutectic composition of the melt. Thus, an effect of two-phase zone between the crust and the melt is not accounted for.

11 References

[1] O. Kymäläinen. H. Tuomisto. T.G. Theofanous. “In-vessel retention of corium at the Loviisa plant”. Nuclear Engineering and Design 169 (1997) pp.109-130.

[2] S. Abalin. I. Gnidoi. V. Semenov. V. Strizhov. A. Surenkov. “The Results and Analysis of the RASPLAV Salt Tests“. Rasplav Seminar 2000. Munich. Germany. 14-15 November 2000.

[3] T. G.Theofanous. S. Angelini. "Natural Convection for In-Vessel Retention at Prototypic Rayleigh Numbers". Nuclear Engineering and Design. 200 (2001). pp. 1-9.

[4] V. Asmolov. et al.. "Challenges Left in the Area of In-Vessel Melt Retention”. Nuclear Engineering and Design. 209 (2001). pp. 87-96.

[5] B. Fluhrer, A. Miassoedov, T. Cron, J. Foit, X. Gaus-Liu, S. Schmidt-Stiefel, T. Wenz, I. Ivanov, D. Popov, "The LIVE-L1 and LIVE-L3 Experiments on Melt Behaviour in RPV Lower Head", FZKA-7419, September 2008.

[6] A. Miassoedov, et al., “Results of the LIVE-L1 Experiment on Melt Behaviour in RPV Lower Head Performed within the LACOMERA project at the Forschungszentrum Karlsruhe”, 2007, Proc. 15th International Conference on Nuclear Engineering (ICONE15), Nagoya, Japan, April 22-26, 2007, Paper 10227.

[7] B. Fluhrer. et al.. “The Experimental Programme LIVE to investigate In-Vessel Core Melt Behaviour in the Late Phase”. Jahrestagung Kerntechnik 2005. Nürnberg. INFORUM GmbH. 2005. pp. 198-201.

[8] Deutsche Risikostudie Kernkraftwerke, Phase B-: eine Untersuchung / Ges. für Reaktorsicherheit. Im Auftr. d. Bundesministers für Forschung u. Technologie. - Köln: Verl. TÜV Rheinland, 1990, ISBN 3-88585-809-6.

[9] R.W. Berg et al., 2004, “The $NaNO_3/KNO_3$ system: the position of the solidus and subsolidus”, Dalton Trans., pp. 2224-2229.

[10] H.M. Goodwin, and R.D. Mailey, ”On the Density. Electrical Conductivity and Viscosity of Fused Salts and Their Mixtures”, The Physical Review - American Physical Society, January, 1980, pp. 40.

[11] Rogers D.J., Janz G. J., “Melting-crystallization and premelting properties of NaNO3-KNO3. Enthalpies and heat capacities”, J. chem. Eng. Data 27, 1982, pp. 424-428.

[12] Kenisarin, M., “High-temperature phase change materials for thermal energy storage”, Renewable and Sustainable Energy Reviews 14, 2010, pp. 955-970

[13] F.P. Incropera, D.P. Dewitt, “Introduction to heat transfer“, ISBN0-471-38649-9, pp. 820.

[14] X. Gaus-Liu, B. Fluhrer, A. Miassoedov, T. Cron, J. Foit, S. Schmidt-Stiefel, T. Wenz; Results f the LIVE-L3A Experiment, KIT Scientific reports 7542, ISBN 978-3-86644-505-5, pp. 40.

[15] Flemmings, “Solidification Processing”, Materials Science and Engineering Series, ISBN 0-07-021283-x, pp.59-66.

[16] B.R. Sehgal, Z.L. Yang, "Ex-vessel Core Melt Stabilization Research; On the Experments with Simulant Materials at KTH“, SAM-ECOSTAR-P11/001, KTH, Stockholm, Sweden, January 2001.

[17] R.P. Tye, “Thermal conductivity”, Ed. by R.P. Tye, Vol. 1, London: Academic Pr., 1969, ISBN 12-705401-4, pp.17.

[18] G.J. Janz, and C.B. Allen, “Physical Properties Data Compilations, Relevant to Storage, II. Molten Salts: Data on Single and Multi-Component Salt Systems”, U Energy.S. Department of Commerce, National Bureau of Standards, NSRDS-NBS 61, Part II, April 1979, pp161+pp148.

[19] DIN EN 60584-2: Thermopaare - Teil 2: Grenzabweichungen der Thermospannungen (IEC 60584-2:1982 + A1:1989); Deutsche Fassung EN 60584-2:1993, 1994

[20] DIN 1319-3, Grundlagen der Meßtechnik, Teile 3: Auswertung von Messungen einer einzeln meßgröße Meßunsicherheit, 1996

[21] DIN EN 60751, Industrielle Platin-Widerstandsthermometer und Platin-Temperatursensoren (IEC 60751:2008); Deutsche Fassung EN 60751:2008, actualised: 2009.

[22] A.E. Aksenova, V.V. Chudanov, V.A. Pervichko, V.N. Semenov, V.F. Strizhov "Development and application of the CONV Codes". *Proceedings of RASPLAV seminar 2000,* Munich, November 14-15 (2000).

[23] A. Aksenova, V. Chudanov, A. Churbanov, V. Pervishko, A. Popkov, V. Strizhov, P. Vabishchevich, V. Varenkov, *CONV2D:* An Integrated Computer Code for Numerical Modelling of Convection/Diffusion Processes with regard for Melting, Nuclear Safety Institute (IBRAE), Moscow (1997).

[24] V. Asmolov, "RASPLAV Project: Major Activities and Results", Proceedings of RASPLAV seminar 2000*,* Munich, Germany, November 14-15 (2000).

[25] L.A. Bolshov, P.S. Kondratenko, V.F. Strizhov, “A semi-quantitative theory of convective heat transfer in a heat generating fluid”, Int. J. Heat and Mass Transfer, Vol. 41, № 10 (1997) pp.1223-1227.

[26] L.A. Bolshov, P.S. Kondratenko, “Limiting angular characteristics of heat transfer and stratification in a heat-generating fluid”, International Journal of Heat and Mass Transfer, Vol. 43, № 20 (2000) pp.3897-3905.

[27] J.M.J. den Toonder and F.T.M. Nieuwstadt, J. Phys. Fluids, Vol. 9, № 11 (1997) pp. 3398-3409.

[28] M. Buck, M. Bürger, A. Miassoedov, X. Gaus-Liu, A. Palagin, L. Godin-Jacqmin, C.T. Tran, W.M .Ma, V. Chudanov, “The LIVE program: tests and joint interpretation within SARNET and ISTC”, The 3rd European Review Meeting on Severe Accident Research (ERMSAR-2008), Nesseber, Bulgaria, 23-25 September 2008.

[29] A. Palagin, F. Kretzschmar, V. Chudanov, “LIVE test FSt4: experimental results and simulation by CONV code”, The 13th International Topical Meeting on Nuclear Reactor Thermal Hydraulics (NURETH-13), Kanazawa City, Japan, September 27-October 2, 2009.

[30] M. Buck, M. Bürger, A. Miassoedov, X. Gaus-Liu, A. Palagin, L. Godin-Jacqmin, C.T. Tran, W.M. Ma, V. Chudanov, “The LIVE program – Results of test L1 and joint analyses on transient molten pool thermal hydraulics”, Progress in Nuclear Energy, 52 (2010) pp. 46–60.

Annex A Data Acquisition and Instrumentation

Annex .A.1 LIVE-L4 and LIVE-L5L channel assignments

Table A- 1 lists all signals that were registered on the PC data acquisition system for the experiments LIVE-L4. All signal cables are attached to a control cabinet, which is positioned near the LIVE test vessel. The temperature signals are all single-ended signals. The reference junctions of thermocouples are traditionally maintained at 0°C. This is assumed in thermocouple calibration tables. In the LIVE experiments, the reference junction is situated in the control cabinet and has ambient temperature. To overcome this error of a non-zero thermocouple reference junction, the temperature of the reference point is measured by three PT-100 sensors (named RT) that are attached at the connector blocks of the thermocouples. This temperature is then used to correct the temperature measured by the thermocouples.

The most designed channels in L5L test were same as in L4. The changes of channel designation in L5L were the additional thermocouple tree CT46 and CT47, which are given in Table A- 2.

Table A- 1: Instrumentation list of LIVE-L4

Nr.	Desig-nation	Category	Sensor	Position			Remarks
				Angle φ	**Radius [mm]**	**Depth [mm]**	**Angle 0= Instrumentation axis; Radius 0 = vertical axis of the vessel Depth 0 = Center of the vessel sphere**
1	ST1	Spout temperature	NiCr/Ni		TE inside lower spout aligner		ST = Spout Temperature
2	MT1	Melt temperature	NiCr/Ni	0	74	426.2	MT = Melt Temperature
3	MT2	Melt temperature	NiCr/Ni	90	74	426.2	
4	MT3	Melt temperature	NiCr/Ni	180	74	426.2	
5	MT4	Melt temperature	NiCr/Ni	270	74	426.2	
6	MT5	Melt temperature	NiCr/Ni	0	174	426.2	
7	MT6	Melt temperature	NiCr/Ni	90	174	426.2	
8	MT7	Melt temperature	NiCr/Ni	180	174	426.2	
9	MT8	Melt temperature	NiCr/Ni	270	174	426.2	
10	MT9	Melt temperature	NiCr/Ni	0	74	326.2	
11	MT10	Melt temperature	NiCr/Ni	90	74	326.2	
12	MT11	Melt temperature	NiCr/Ni	180	74	326.2	
13	MT12	Melt temperature	NiCr/Ni	270	74	326.2	
14	MT13	Melt temperature	NiCr/Ni	0	174	326.2	
15	MT14	Melt temperature	NiCr/Ni	90	174	326.2	
16	MT15	Melt temperature	NiCr/Ni	180	174	326.2	
17	MT16	Melt temperature	NiCr/Ni	270	174	326.2	
18	MT17	Melt temperature	NiCr/Ni	0	274	326.2	
19	MT18	Melt temperature	NiCr/Ni	90	274	326.2	
20	MT19	Melt temperature	NiCr/Ni	180	274	326.2	
21	MT20	Melt temperature	NiCr/Ni	270	274	326.2	
22	MT21	Melt temperature	NiCr/Ni	0	74	226.2	
23	MT22	Melt temperature	NiCr/Ni	90	74	226.2	
24	MT23	Melt temperature	NiCr/Ni	180	74	226.2	
25	MT24	Melt temperature	NiCr/Ni	270	74	226.2	
26	MT25	Melt temperature	NiCr/Ni	0	174	226.2	
27	MT26	Melt temperature	NiCr/Ni	90	174	226.2	
28	MT27	Melt temperature	NiCr/Ni	180	174	226.2	
29	MT28	Melt temperature	NiCr/Ni	270	174	226.2	
30	MT29	Melt temperature	NiCr/Ni	0	274	226.2	
31	MT30	Melt temperature	NiCr/Ni	90	274	226.2	
32	MT31	Melt temperature	NiCr/Ni	180	274	226.2	
33	MT32	Melt temperature	NiCr/Ni	270	274	226.2	
34	MT33	Melt temperature	NiCr/Ni	0	374	226.2	
35	MT34	Melt temperature	NiCr/Ni	90	374	226.2	
36	MT35	Melt temperature	NiCr/Ni	180	374	226.2	
37	MT36	Melt temperature	NiCr/Ni	270	374	226.2	
38	MT37	Temp. above melt	NiCr/Ni	0	60	26.2	
39							free

40							free
41	LT1	Temp of lance	NiCr/Ni	340	365	variable	TE of crust detection lance
42	LT2	Temp of lance	NiCr/Ni	340	365	variable	
43	LT3	Temp of lance	NiCr/Ni	340	365	variable	
44	LT4	Temp of lance	NiCr/Ni	340	365	variable	
45	LT5	Temp of lance	NiCr/Ni	340	365	variable	
46	OOT1	Outer temperature cooling tank	NiCr/Ni	300	38	706.2	OOT = Temperature of the cooling tank outer surface
47	OOT2	Outer temperature cooling tank	NiCr/Ni	300	428	563.2	
48	OOT3	Outer temperature cooling tank	NiCr/Ni	300	670	226.2	
49	IT1	Wall inner temp.	NiCr/Ni	292.5	35	496.2	IT = Temperature of the test vessel inner surface
50	IT2	Wall inner temp.	NiCr/Ni	22.5	249	431.2	
51	IT3	Wall inner temp.	NiCr/Ni	112.5	249	431.2	
52	IT4	Wall inner temp.	NiCr/Ni	202.5	249	431.2	
53	IT5	Wall inner temp.	NiCr/Ni	292.5	249	431.2	
54	IT6	Wall inner temp.	NiCr/Ni	22.5	387	313.2	
55	IT7	Wall inner temp.	NiCr/Ni	112.5	387	313.2	
56	IT8	Wall inner temp.	NiCr/Ni	202.5	387	313.2	
57	IT9	Wall inner temp.	NiCr/Ni	292.5	387	313.2	
58	IT10	Wall inner temp.	NiCr/Ni	22.5	453	206.2	
59	IT11	Wall inner temp.	NiCr/Ni	112.5	453	206.2	
60	IT12	Wall inner temp.	NiCr/Ni	202.5	453	206.2	
61	IT13	Wall inner temp.	NiCr/Ni	292.5	453	206.2	
62	IT14	Wall inner temp.	NiCr/Ni	22.5	484	116.2	
63	IT15	Wall inner temp.	NiCr/Ni	112.5	484	116.2	
64	IT16	Wall inner temp.	NiCr/Ni	202.5	484	116.2	
65	IT17	Wall inner temp.	NiCr/Ni	292.5	484	116.2	
66	-	-	NiCr/Ni	-	-		free
67	HFT1	Temp.of sensor 1	NiCr/Ni	0	0	496.2	HFT = Heat Flux Temperature PT = Plug Temperature Designation of last number: length of the thermocouple from the inner vessel wall into the melt: 1 = 0 mm 2 = 5 mm 3 = 10 mm 4 = 15 mm 5 = 20 mm
68	PT11	Temp of plug 1	NiCr/Ni	0	0	496.2	
69	PT12	Temp of plug 1	NiCr/Ni	0	0	496.2	
70	PT13	Temp. of plug 1	NiCr/Ni	0	0	496.2	
71	PT14	Temp of plug 1	NiCr/Ni	0	0	496.2	
72	PT15	Temp of plug 1	NiCr/Ni	0	0	496.2	
73	HFT5	Temp of sensor 5	NiCr/Ni	337.5	248.18	430.2	
74	PT51	Temp of plug 5	NiCr/Ni	337.5	248.18	430.2	
75	PT52	Temp of plug 5	NiCr/Ni	337.5	248.18	430.2	
76	PT53	Temp of plug 5	NiCr/Ni	337.5	248.18	430.2	
77	PT54	Temp of plug 5	NiCr/Ni	337.5	248.18	430.2	
78	PT55	Temp of plug 5	NiCr/Ni	337.5	248.18	430.2	
79	HFT9	Temp. of sensor 9	NiCr/Ni	337.5	385.75	313.2	
80	PT91	Temp of plug 9	NiCr/Ni	337.5	385.75	313.2	
81	PT92	Temp of plug 9	NiCr/Ni	337.5	385.75	313.2	
82	PT93	Temp of plug 9	NiCr/Ni	337.5	385.75	313.2	
83	PT94	Temp of plug 9	NiCr/Ni	337.5	385.75	313.2	
84	PT95	Temp of plug 9	NiCr/Ni	337.5	385.75	313.2	
85	HFT13	Temp.of sensor 13	NiCr/Ni	337.5	451.69	206.2	
86	PT131	Temp.of plug 13	NiCr/Ni	337.5	451.69	206.2	
87	PT132	Temp.of plug 13	NiCr/Ni	337.5	451.69	206.2	
88	PT133	Temp.of plug 13	NiCr/Ni	337.5	451.69	206.2	

89	PT134	Temp.of plug 13	NiCr/Ni	337.5	451.69	206.2	
90	PT135	Temp.of plug 13	NiCr/Ni	337.5	451.69	206.2	
91	HFT17	Temp. of sensor 17	NiCr/Ni	337.5	482.66	116.2	
92	PT171	Temp. of plug 17	NiCr/Ni	337.5	482.66	116.2	
93	PT172	Temp. of plug 17	NiCr/Ni	337.5	482.66	116.2	
94	PT173	Temp. of plug 17	NiCr/Ni	337.5	482.66	116.2	
95	PT174	Temp. of plug 17	NiCr/Ni	337.5	482.66	116.2	
96	PT175	Temp. of plug 17	NiCr/Ni	337.5	482.66	116.2	
97	HFT4	Temp. of sensor 4	NiCr/Ni	247.5	248.18	430.2	
98	PT41	Temp. of plug 4	NiCr/Ni	247.5	248.18	430.2	
99	PT42	Temp. of plug 4	NiCr/Ni	247.5	248.18	430.2	
100	PT43	Temp. of plug 4	NiCr/Ni	247.5	248.18	430.2	
101	PT44	Temp. of plug 4	NiCr/Ni	247.5	248.18	430.2	
102	PT45	Temp. of plug 4	NiCr/Ni	247.5	248.18	430.2	
103	HFT8	Temp. of sensor 8	NiCr/Ni	247.5	385.75	313.2	
104	PT81	Temp. of plug 8	NiCr/Ni	247.5	385.75	313.2	
105	PT82	Temp. of plug 8	NiCr/Ni	247.5	385.75	313.2	
106	PT83	Temp. of plug 8	NiCr/Ni	247.5	385.75	313.2	
107	PT84	Temp. of plug 8	NiCr/Ni	247.5	385.75	313.2	
108	PT85	Temp. of plug 8	NiCr/Ni	247.5	385.75	313.2	
109	HFT12	Temp of sensor 12	NiCr/Ni	247.5	451.69	206.2	
110	PT121	Temp.of plug 12	NiCr/Ni	247.5	451.69	206.2	
111	PT122	Temp. of plug 12	NiCr/Ni	247.5	451.69	206.2	
112	PT123	Temp. of plug 12	NiCr/Ni	247.5	451.69	206.2	
113	PT124	Temp. of plug 12	NiCr/Ni	247.5	451.69	206.2	
114	PT125	Temp. of plug 12	NiCr/Ni	247.5	451.69	206.2	
115	HFT16	Temp. of sensor 16	NiCr/Ni	247.5	482.66	116.2	
116	PT161	Temp. of plug 16	NiCr/Ni	247.5	482.66	116.2	
117	PT162	Temp. of plug 16	NiCr/Ni	247.5	482.66	116.2	
118	PT163	Temp. of plug 16	NiCr/Ni	247.5	482.66	116.2	
119	PT164	Temp. of plug 16	NiCr/Ni	247.5	482.66	116.2	
120	PT165	Temp. of plug 16	NiCr/Ni	247.5	482.66	116.2	
121	HFT3	Temp. of sensor 3	NiCr/Ni	157.5	248.18	430.2	
122	PT31	Temp. of plug 3	NiCr/Ni	157.5	248.18	430.2	
123	PT32	Temp. of plug 3	NiCr/Ni	157.5	248.18	430.2	
124	PT33	Temp. of plug 3	NiCr/Ni	157.5	248.18	430.2	
125	PT34	Temp. of plug 3	NiCr/Ni	157.5	248.18	430.2	
126	PT35	Temp. of plug 3	NiCr/Ni	157.5	248.18	430.2	
127	HFT7	Temp. of sensor 7	NiCr/Ni	157.5	385.75	313.2	
128	PT71	Temp. of plug 7	NiCr/Ni	157.5	385.75	313.2	
129	PT72	Temp. of plug 7	NiCr/Ni	157.5	385.75	313.2	
130	PT73	Temp. of plug 7	NiCr/Ni	157.5	385.75	313.2	
131	PT74	Temp. of plug 7	NiCr/Ni	157.5	385.75	313.2	
132	PT75	Temp. of plug 7	NiCr/Ni	157.5	385.75	313.2	
133	HFT11	Temp. of sensor 11	NiCr/Ni	157.5	451.69	206.2	
134	PT111	Temp. of plug 11	NiCr/Ni	157.5	451.69	206.2	
135	PT112	Temp. of plug 11	NiCr/Ni	157.5	451.69	206.2	
136	PT113	Temp. of plug 11	NiCr/Ni	157.5	451.69	206.2	
137	PT114	Temp. of plug 11	NiCr/Ni	157.5	451.69	206.2	
138	PT115	Temp. of plug 11	NiCr/Ni	157.5	451.69	206.2	
139	HFT15	Temp. of sensor 15	NiCr/Ni	157.5	482.66	116.2	

140	PT151	Temp. of sensor 15	NiCr/Ni	157.5	482.66	116.2	
141	PT152	Temp. of sensor 15	NiCr/Ni	157.5	482.66	116.2	
142	PT153	Temp. of sensor 15	NiCr/Ni	157.5	482.66	116.2	
143	PT154	Temp. of sensor 15	NiCr/Ni	157.5	482.66	116.2	
144	PT155	Temp. of sensor 15	NiCr/Ni	157.5	482.66	116.2	
145	HFT2	Temp of sensor 2	NiCr/Ni	67.5	248.18	430.2	
146	PT21	Temp. of plug 2	NiCr/Ni	67.5	248.18	430.2	
147	PT22	Temp. of plug 2	NiCr/Ni	67.5	248.18	430.2	
148	PT23	Temp. of plug 2	NiCr/Ni	67.5	248.18	430.2	
149	PT24	Temp. of plug 2	NiCr/Ni	67.5	248.18	430.2	
150	PT25	Temp. of plug 2	NiCr/Ni	67.5	248.18	430.2	
151	HFT6	Temp of sensor 6	NiCr/Ni	67.5	385.75	313.2	
152	PT61	Temp of plug 6	NiCr/Ni	67.5	385.75	313.2	
153	PT62	Temp of plug 6	NiCr/Ni	67.5	385.75	313.2	
154	PT63	Temp of plug 6	NiCr/Ni	67.5	385.75	313.2	
155	PT64	Temp of plug 6	NiCr/Ni	67.5	385.75	313.2	
156	PT65	Temp of plug 6	NiCr/Ni	67.5	385.75	313.2	
157	HFT10	Temp of sensor 10	NiCr/Ni	67.5	451.69	206.2	
158	PT101	Temp of plug 10	NiCr/Ni	67.5	451.69	206.2	
159	PT102	Temp of plug 10	NiCr/Ni	67.5	451.69	206.2	
160	PT103	Temp of plug 10	NiCr/Ni	67.5	451.69	206.2	
161	PT104	Temp of plug 10	NiCr/Ni	67.5	451.69	206.2	
162	PT105	Temp of plug 10	NiCr/Ni	67.5	451.69	206.2	
163	HFT14	Temp. of sensor 14	NiCr/Ni	67.5	482.66	116.2	
164	PT141	Temp of plug 14	NiCr/Ni	67.5	482.66	116.2	
165	PT142	Temp of plug 14	NiCr/Ni	67.5	482.66	116.2	
166	PT143	Temp of plug 14	NiCr/Ni	67.5	482.66	116.2	
167	PT144	Temp of plug 14	NiCr/Ni	67.5	482.66	116.2	
168	PT145	Temp of plug 14	NiCr/Ni	67.5	482.66	116.2	
169	HF1	Heat flux sensor 1	WFS	0	0	496.2	
170	HF2	Heat flux sensor 2	WFS	67.5	248.18	430.2	
171	HF3	Heat flux sensor 3	WFS	157.5	248.18	430.2	
172	HF4	Heat flux sensor 4	WFS	247.5	248.18	430.2	
173	HF5	Heat flux sensor 5	WFS	337.5	248.18	430.2	
174	HF6	Heat flux sensor 6	WFS	67.5	385.75	313.2	
175	HF7	Heat flux sensor 7	WFS	157.5	385.75	313.2	
176	HF8	Heat flux sensor 8	WFS	247.5	385.75	313.2	
177	HF9	Heat flux sensor 9	WFS	337.5	385.75	313.2	
178	HF10	Heat flux sensor 10	WFS	67.5	451.69	206.2	
179	HF11	Heat flux sensor 11	WFS	157.5	451.69	206.2	
180	HF12	Heat flux sensor 12	WFS	247.5	451.69	206.2	
181	HF13	Heat flux sensor 13	WFS	337.5	451.69	206.2	
182	HF14	Heat flux sensor 14	WFS	67.5	482.66	116.2	
183	HF15	Heat flux sensor 15	WFS	157.5	482.66	116.2	
184	HF16	Heat flux sensor 16	WFS	247.5	482.66	116.2	
185	HF17	Heat flux sensor 17	WFS	337.5	482.66	116.2	
186	Res.	-	-	-	-		free
187	Res.	-	-	-	-		free
188	RT1	Resistance Ther-mometer		Temperature Control Cabinet - -			RT = Resistance Thermometer
189	RT2	Resistance Ther-mometer		Temperature Control Cabinet - -			

190	RT3	Resistance Thermometer		Temperature Control Cabinet			
191	OT1	wall outer temp.	NiCr/Ni	292.5	36.35	518.2	OT = wall outer suface temperature
192	OT2	wall outer temp.	NiCr/Ni	22.5	260	449.2	
193	OT3	wall outer temp.	NiCr/Ni	112.5	260	449.2	
194	OT4	wall outer temp.	NiCr/Ni	202.5	260	449.2	
195	OT5	wall outer temp.	NiCr/Ni	292.5	260	449.2	
196	OT6	wall outer temp.	NiCr/Ni	22.5	404	326.2	
197	OT7	wall outer temp.	NiCr/Ni	112.5	404	326.2	
198	OT8	wall outer temp.	NiCr/Ni	205.5	404	326.2	
199	OT9	wall outer temp.	NiCr/Ni	292.5	404	326.2	
200	OT10	wall outer temp.	NiCr/Ni	22.5	474	215.2	
201	OT11	wall outer temp.	NiCr/Ni	112.5	474	215.2	
202	OT12	wall outer temp.	NiCr/Ni	202.5	474	215.2	
203	OT13	wall outer temp.	NiCr/Ni	292.5	474	215.2	
204	OT14	wall outer temp.	NiCr/Ni	22.5	506	121.2	
205	OT15	wall outer temp.	NiCr/Ni	112.5	506	121.2	
206	OT16	wall outer temp.	NiCr/Ni	202.5	506	121.2	
207	OT17	wall outer temp.	NiCr/Ni	292.5	506	121.2	
208	CT41	Crust temp. tree 1	NiCr/Ni	35	299	396.6	CT = Crust Temperature Designation of the number "b" in CT4b: length of the thermocouple from the inner vessel wall into the melt 1 = 0 mm 2 = 9 mm 3 = 18 mm 4 = 27 mm 5 = 36 mm 6 = 45 mm 7 = 54 mm the number "b" in CT2b and CT3b: 1= 0 mm 2 = 3 mm 3 = 6 mm 4 = 9 mm 5 = 12 mm 6 =15 mm 7 = 18 mm
209	CT42	Crust temp. tree 1	NiCr/Ni	35	299	396.6	
210	CT43	Crust temp. tree 1	NiCr/Ni	35	299	396.6	
211	CT44	Crust temp. tree 1	NiCr/Ni	35	299	396.6	
212	CT45	Crust temp. tree 1	NiCr/Ni	35	299	396.6	
213	CT46	Crust temp. tree 1	NiCr/Ni	35	299	396.6	
214	CT47	Crust temp. tree 1	NiCr/Ni	35	299	396.6	
215	CT21	Crust temp. tree 2	NiCr/Ni	35	398	296.6	
216	CT22	Crust temp. tree 2	NiCr/Ni	35	398	296.6	
217	CT23	Crust temp. tree 2	NiCr/Ni	35	398	296.6	
218	CT24	Crust temp. tree 2	NiCr/Ni	35	398	296.6	
219	CT25	Crust temp. tree 2	NiCr/Ni	35	398	296.6	
220	CT26	Crust temp. tree 2	NiCr/Ni	35	398	296.6	
221	CT27	Crust temp. tree 2	NiCr/Ni	35	398	296.6	
222	CT31	Crust temp. tree 3	NiCr/Ni	35	456	196.6	
223	CT32	Crust temp. tree 3	NiCr/Ni	defect			
224	CT33	Crust temp. tree 3	NiCr/Ni	35	456	196.6	
225	CT34	Crust temp. tree 3	NiCr/Ni	35	456	196.6	
226	CT35	Crust temp. tree 3	NiCr/Ni	35	456	196.6	
227	CT36	Crust temp. tree 3	NiCr/Ni	35	456	196.6	
228	CT37	Crust temp. tree 3	NiCr/Ni	35	456	196.6	
229	AT2	Temp. cooling water outflow	NiCr/Ni	inside below of overflow rod			(Redundanz)
230	AT1	Temp. cooling water outflow	NiCr/Ni	inside below of overflow rod			
231	ZT1	Temp. cooling water inflow	NiCr/Ni	behind flowmeter			
232	KT1	Temp. condensate outflow	NiCr/Ni	behind condensator			
233	W1	Weight of vessel	W. cells	-			
234	DF1	cooling water flow rate	Krohne	inside cooling water inlet (By-pass)			flowmeter 0-2 l/s (DN25)

235	DF2	Flow rate cooling water	Krohne	inside cooling water inlet	flowmeter 0-416.7 ml/s (25 l/min) (DN10)
	DTI1	insulation lid downside temp	NiCr/Ni	67.5	60
	DTI2	insulation lid downside temp	NiCr/Ni	67.5	450
	DTA1	insulation lid upside temp	NiCr/Ni	67.5	75
	DTA2	insulation lid upside temp	NiCr/Ni	67.5	450

Table A- 2: Changes of channel designation in LIVE-L5L comparing with LIVE –L4.

Nr.	**Desig-nation**	**Category**	**Sensor**	**Position**			**Remarks**
				Angle φ	**Radius [mm]**	**Depth [mm]**	**Angle 0 = In-strumentation axis;** **Radius 0 = verti-cal axis of the vessel** **Depth 0 = Center of the vessel sphere**
208	CT11	Temp.of TE-tree 1	NiCr/Ni	35	299	396.6	CT = Crust Tem-perature Designation of the "b" number of CT"1b" 1 = 0 mm 2 = 5 mm 3 = 10 mm 4 = 15 mm 5 = 20 mm (6 = 25 mm 7 = 30 mm from the inner vessel wall into the melt
209	CT12	Temp.of TE tree 1	NiCr/Ni	35	299	396.6	
210	CT13	Temp.of TE tree 1	NiCr/Ni	35	299	396.6	
211	CT14	Temp.of TE tree 1	NiCr/Ni	35	299	396.6	
212	CT15	Temp.of TE tree 1	NiCr/Ni	35	299	396.6	
213	CT16	Temp.of TE tree 1	NiCr/Ni	35	299	396.6	
214	CT17	Temp.of TE tree 1	NiCr/Ni	35	299	396.6	
39	CT46	Temp of TE-Tree 4	NiCr/Ni	25	299	396.6	45 mm in the melt
40	CT47	Temp of TE-Tree 4	NiCr/Ni	25	299	396.6	54 mm in the melt

Annex .A.2 Drawings of the instrumentation of the LIVE test vessel

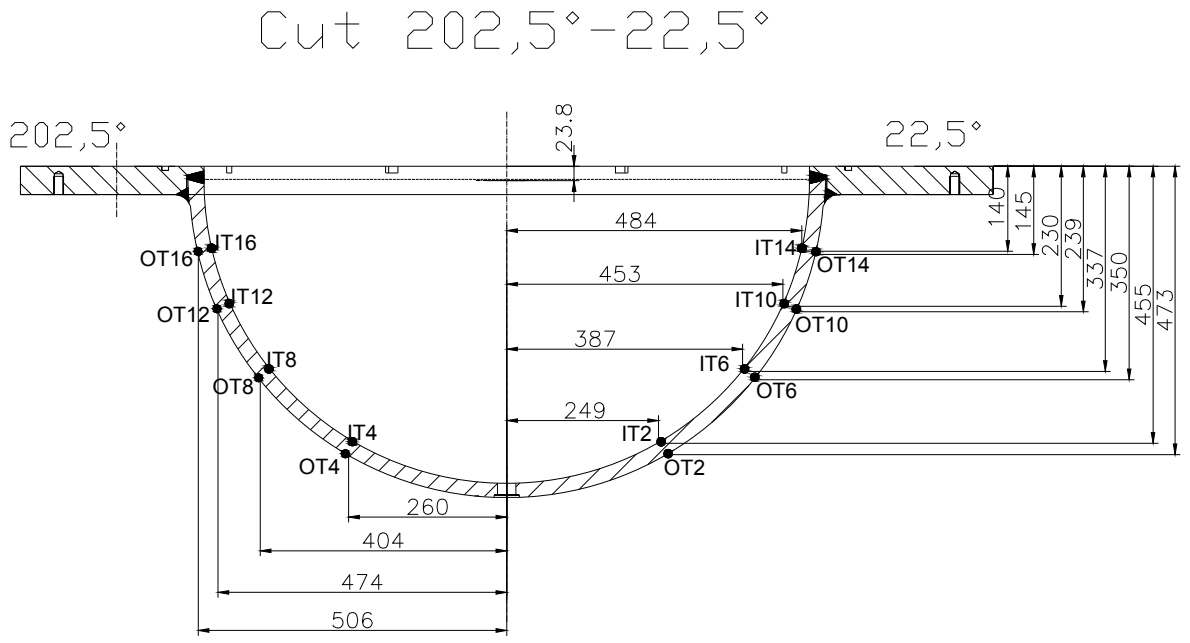

Figure A- 1: IT and OT thermocouple poistions along the azimuth 22.5° and 202.5°

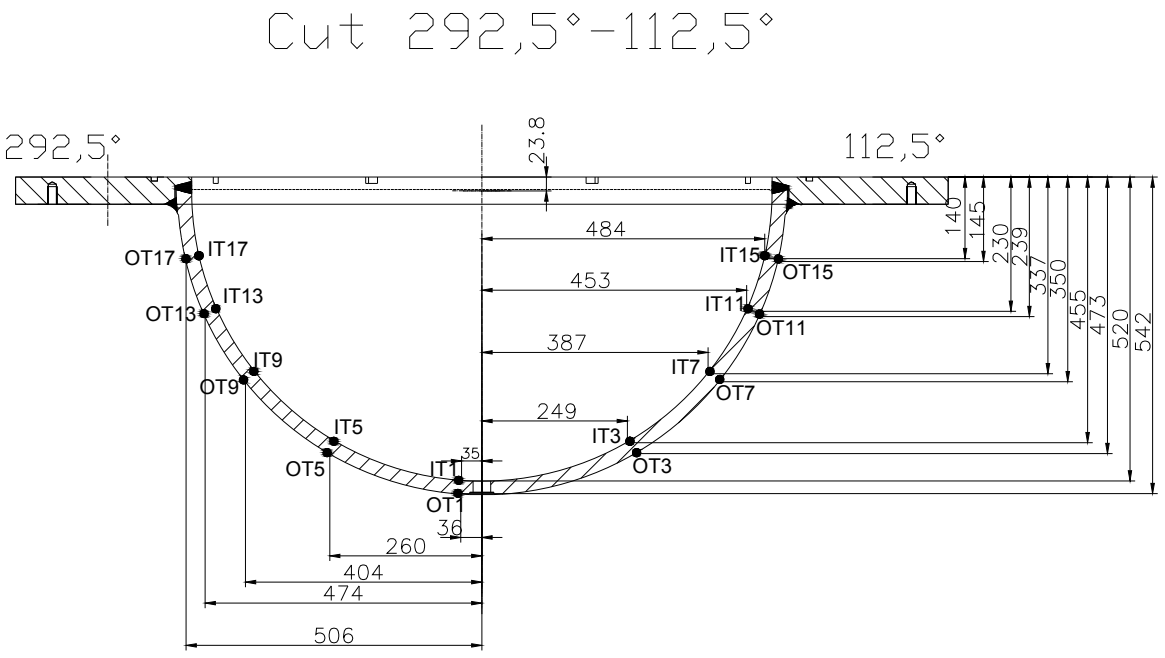

Figure A- 2: IT and OT thermocouples positions along azimuth 112.5° and 292.5°

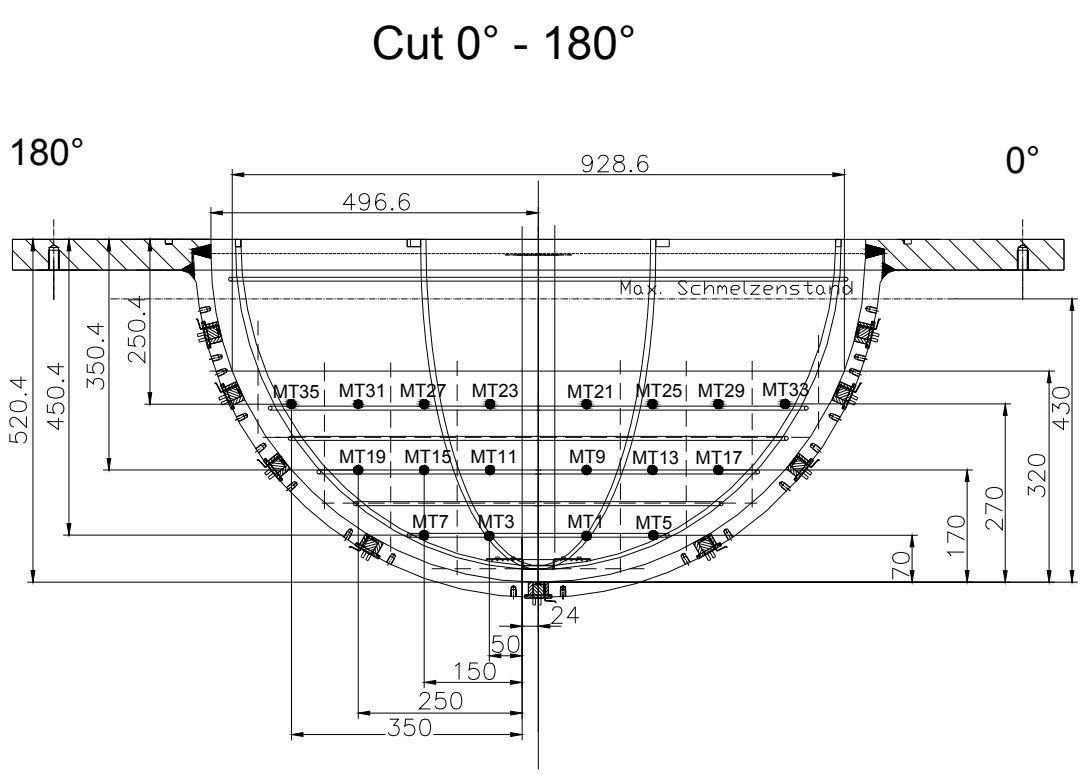

Figure A- 3: MT thermocouple positions in the section 0° - 180°

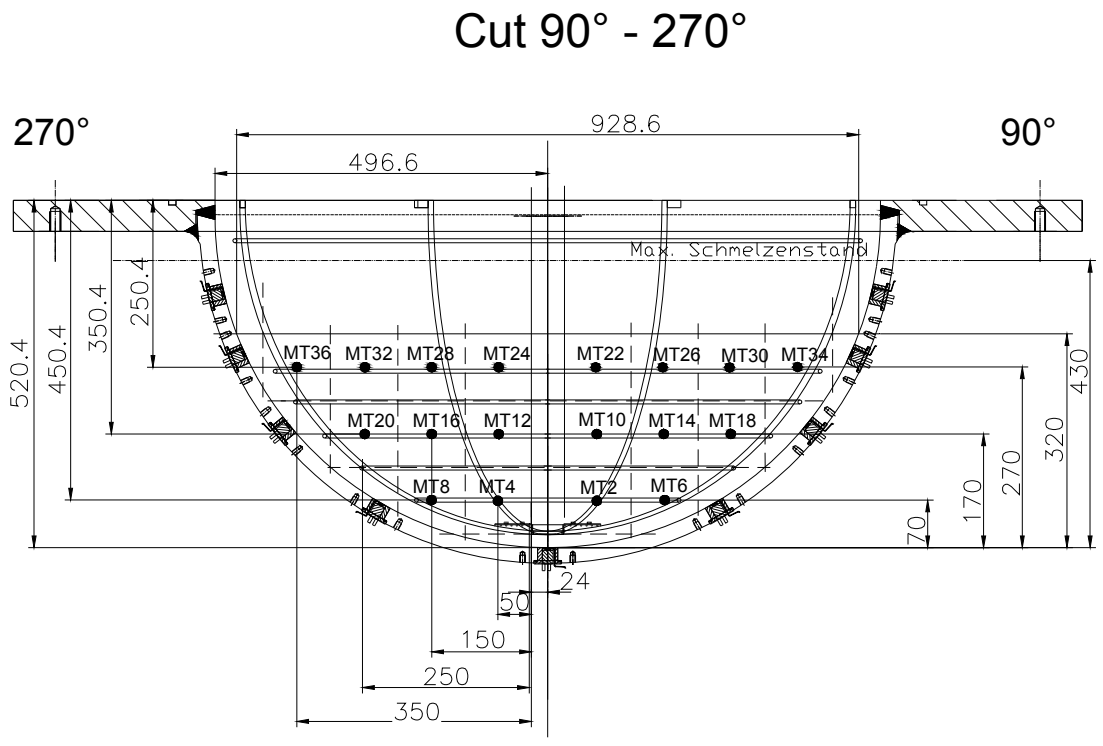

Figure A- 4: MT thermocouple positions in the section 90° - 270°

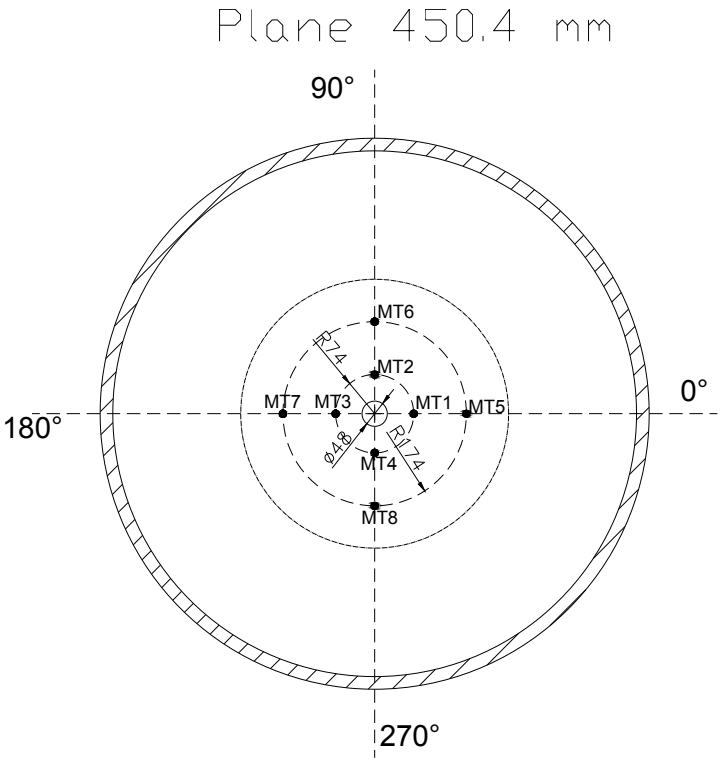

Figure A- 5: MT thermocouples at 450.4 mm from the vessel upper edge (70 mm height)

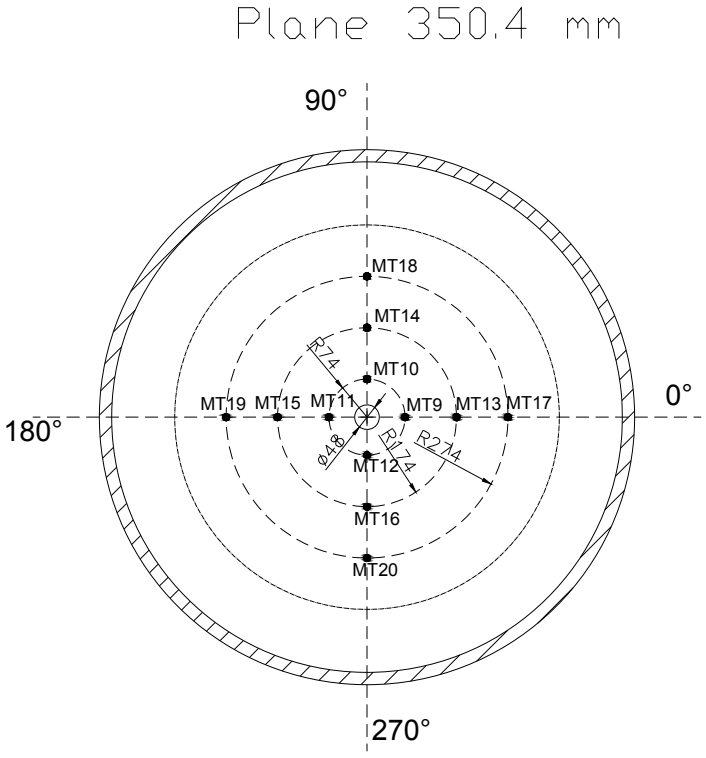

Figure A- 6: MT thermocouples at 350.4 mm. from vessel upper edge (170 mm height)

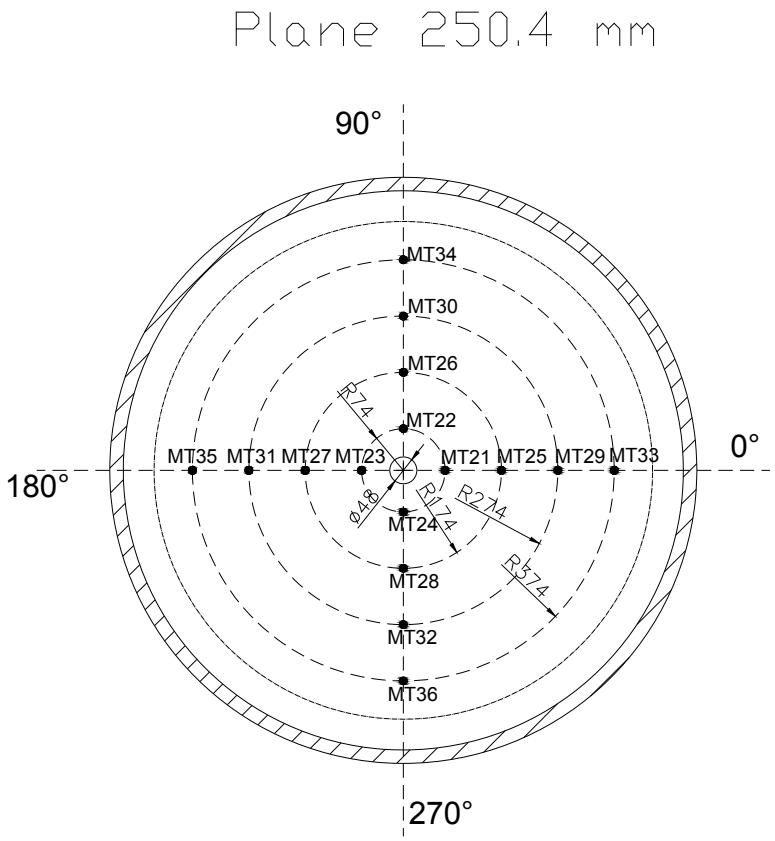

Figure A- 7: MT thermocouples at 250.4 mm from vessel upper edge (270 mm height)

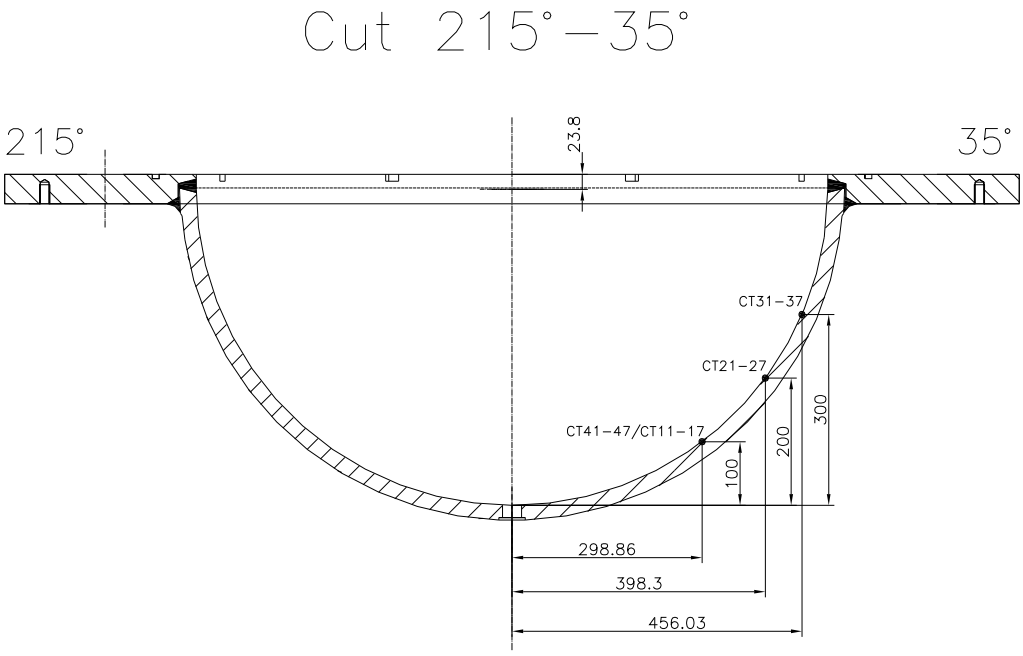

Figure A- 8: Thermocouple trees along the azimuth 25° and 35°

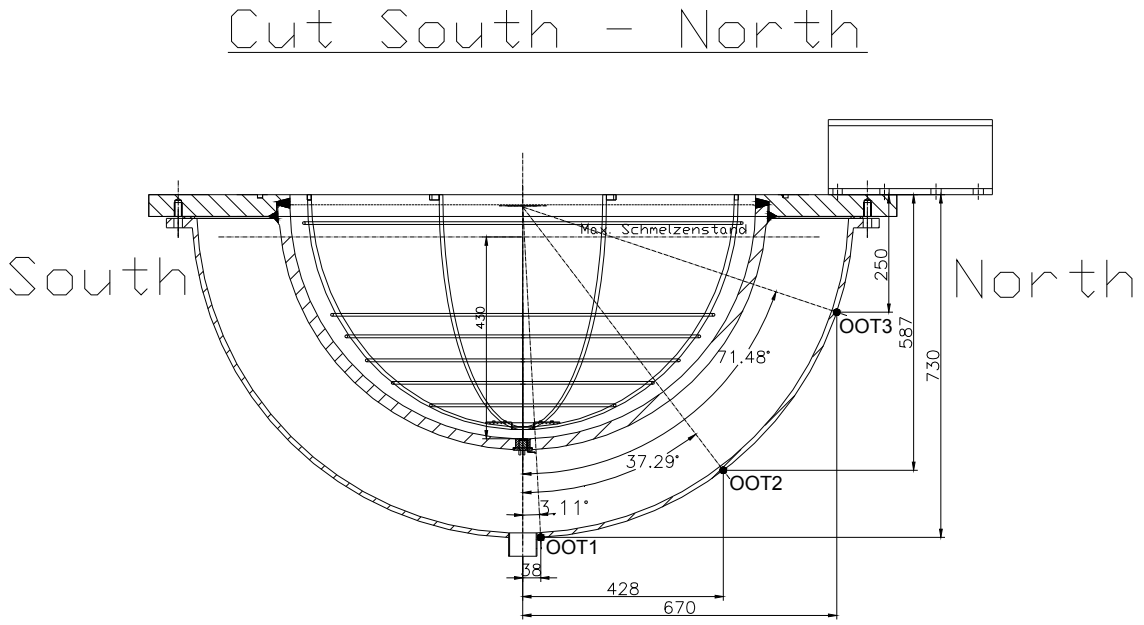

Figure A- 9: OOT Thermocouples at the outer surface of the cooling tank

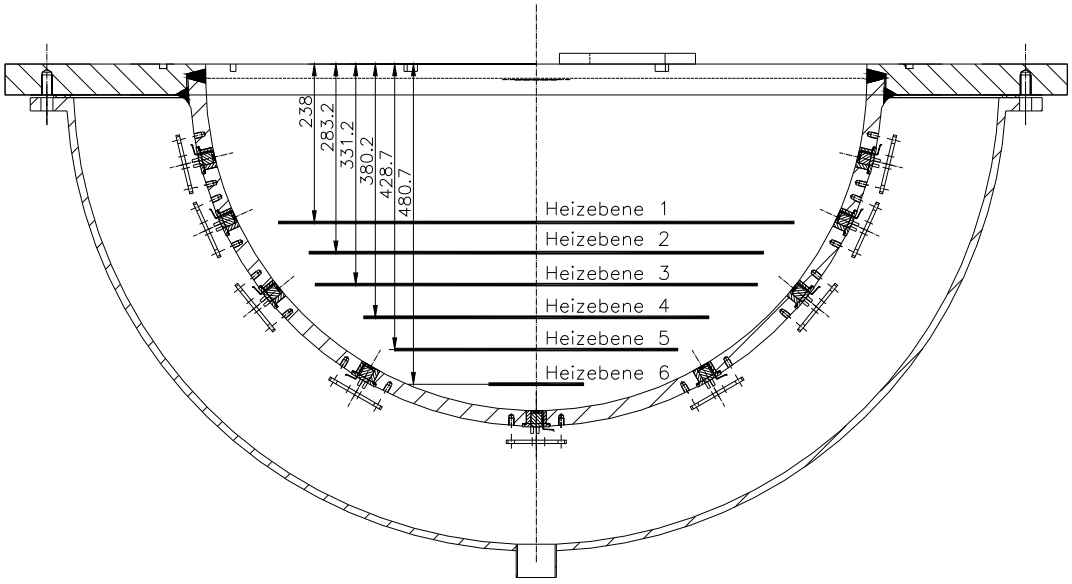

Figure A- 10: Heating planes in the test vessel

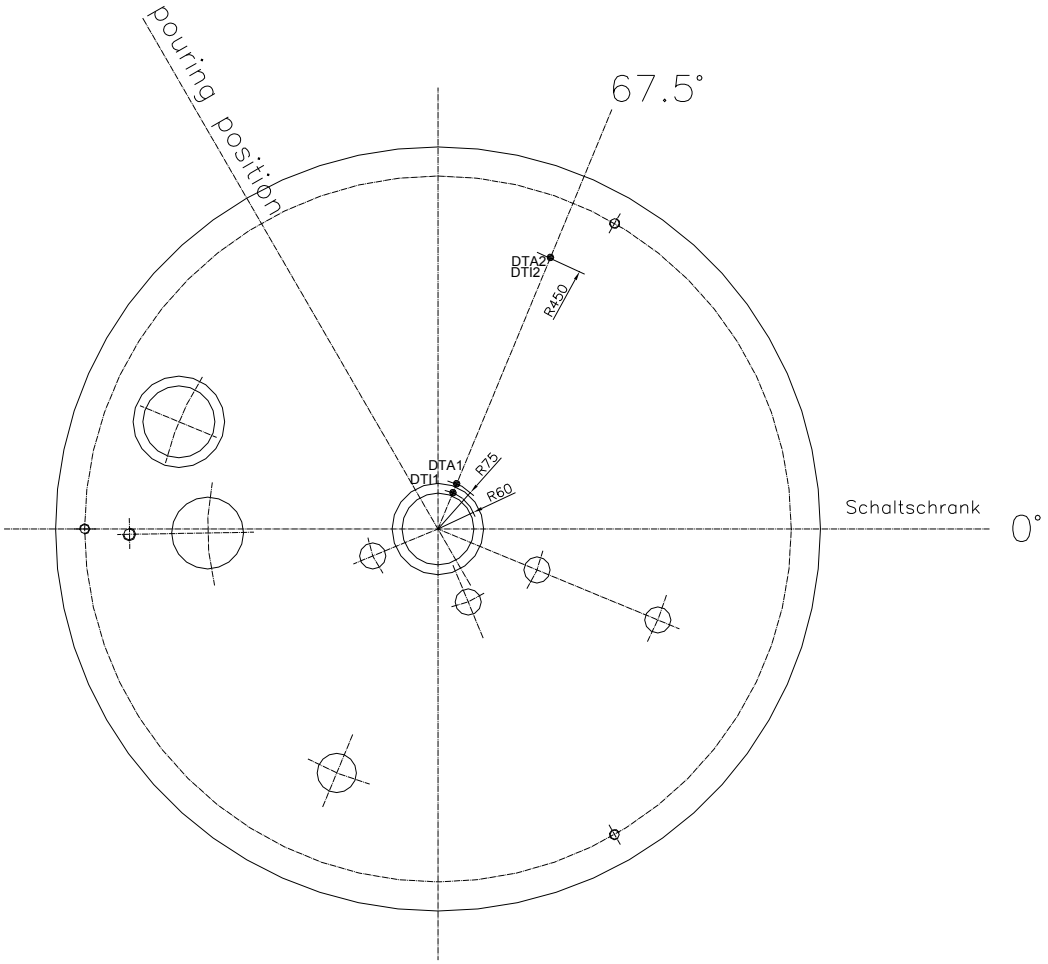

Figure A- 11: Thermocouples on the insulation lid outer surface (DTA2 and DTA1) und on the protection shield under the lid (DTI1 and DTI2).

Annex B Test data of LIVE-L4

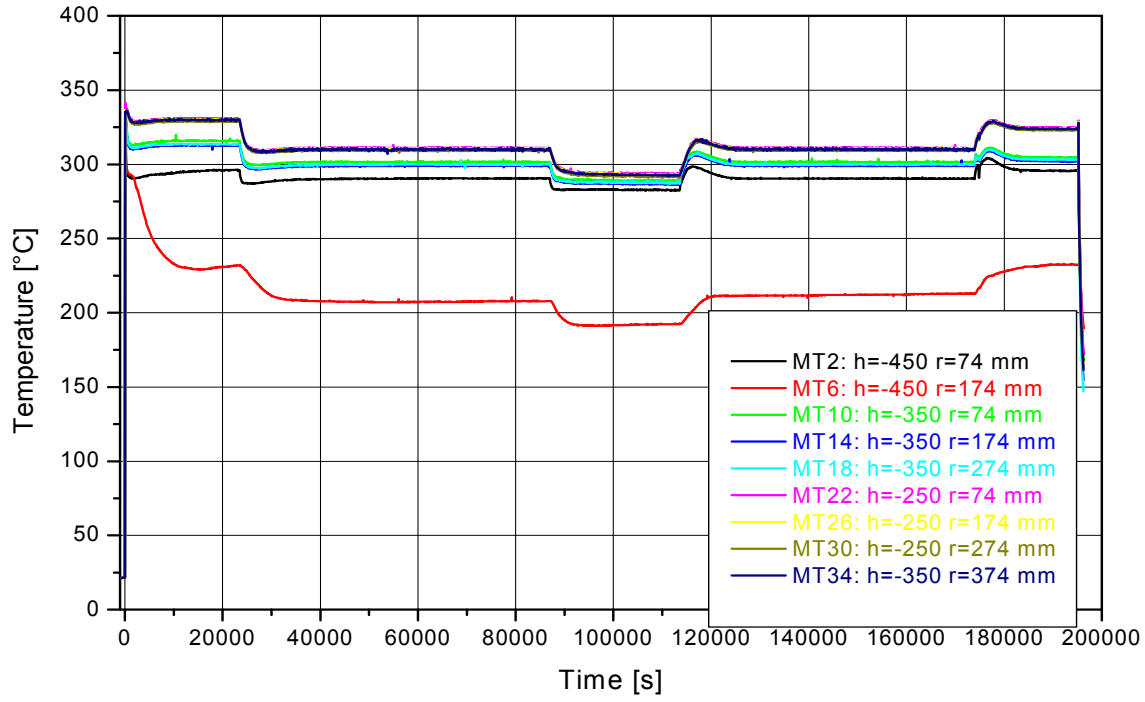

Figure B- 1: L4 melt pool temperature at azimuth 90°

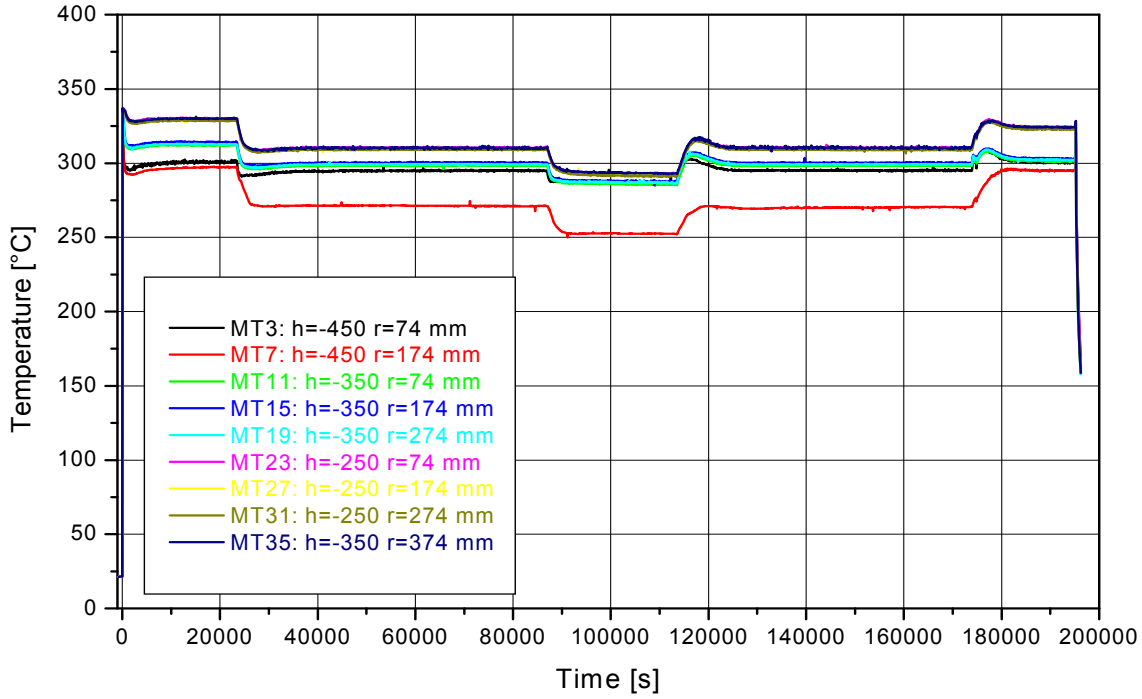

Figure B- 2: L4 melt pool temperature at azimuth 180°

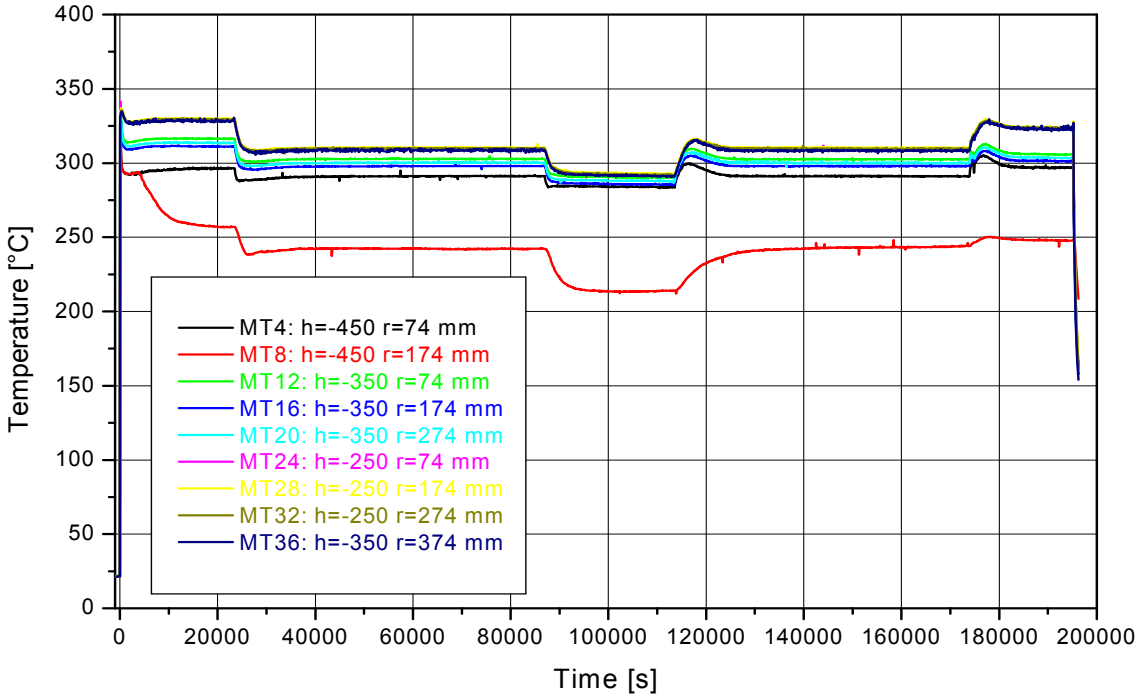

Figure B- 3: L4 melt temperature at azimuth 270°

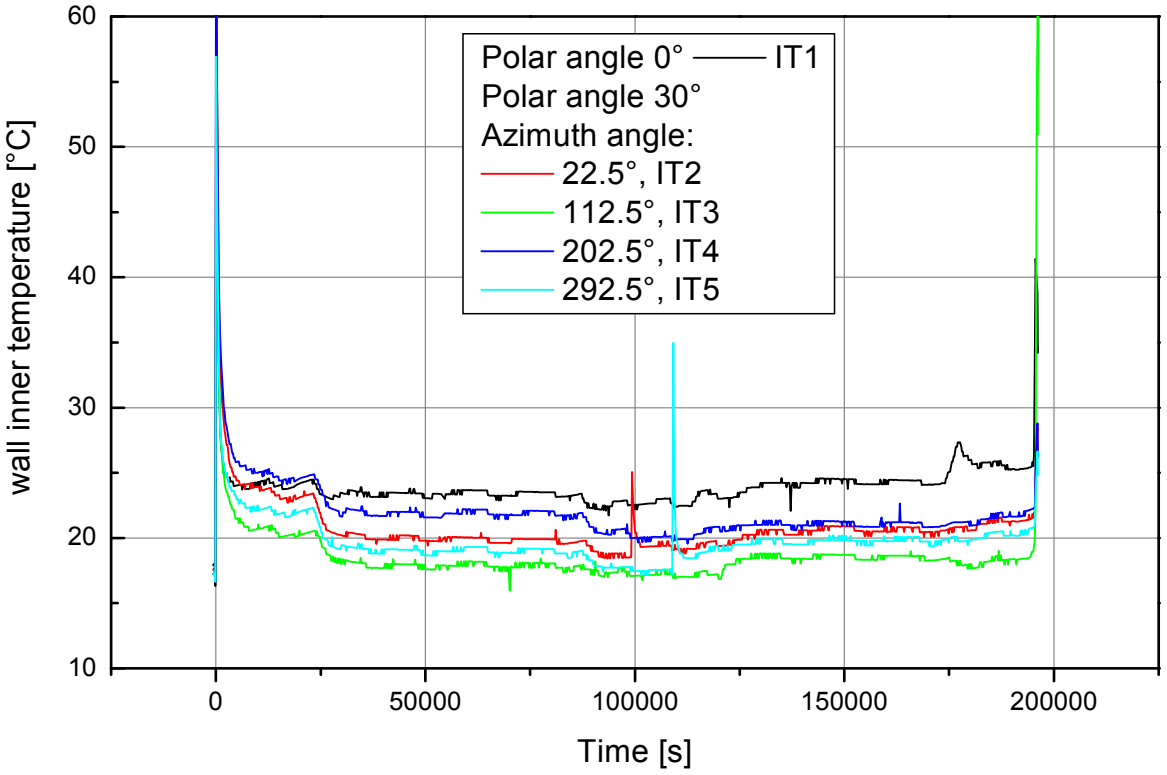

Figure B- 4: L4 vessel wall inner temperatures at polar angle 0° and 30°

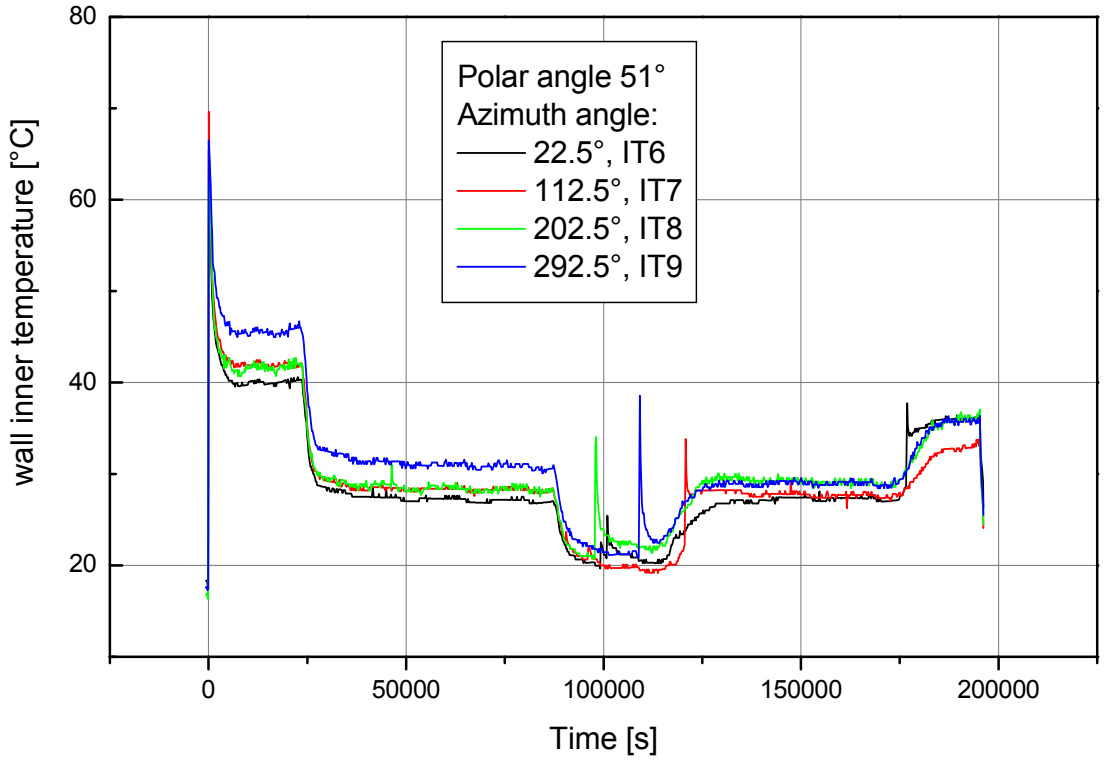

Figure B- 5: L4 vessel wall inner temperature at polar angle 51°

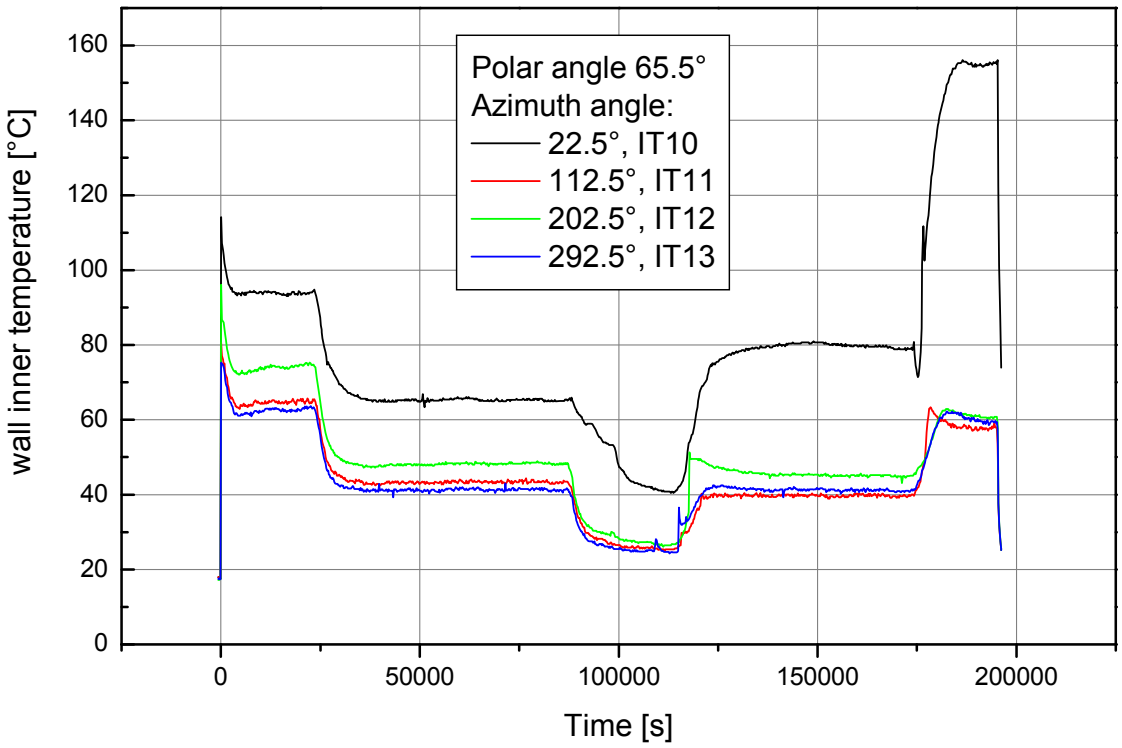

Figure B- 6: L4 vessel wall inner temperature at polar angle 65.5°

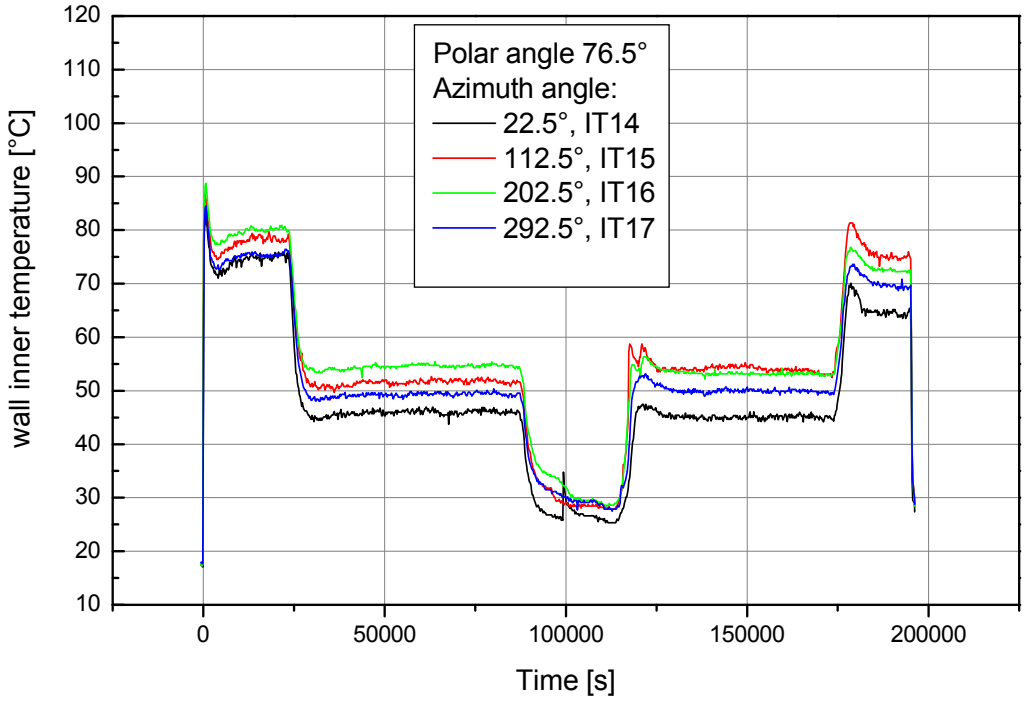

Figure B- 7: L4 vessel wall inner temperature at 76.5°

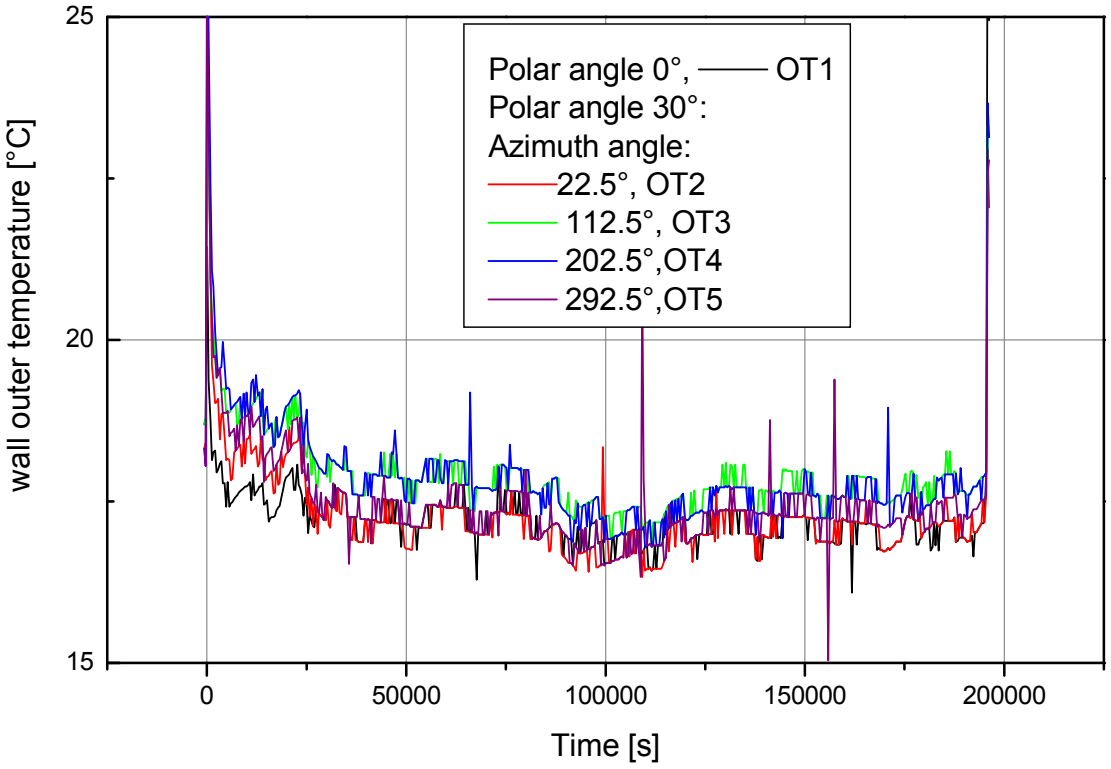

Figure B- 8: L4 vessel wall outer temperature at polar angle 0° and 30°

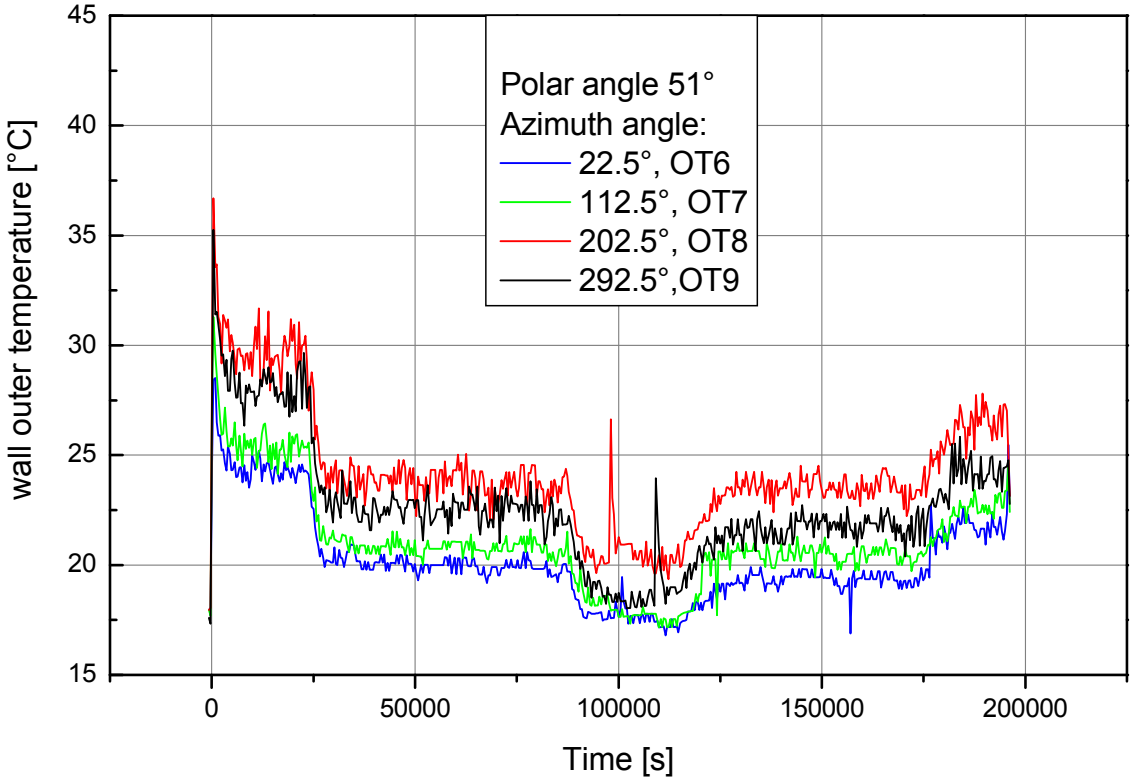

Figure B- 9: L4 vessel wall outer temperature at polar angle 51°

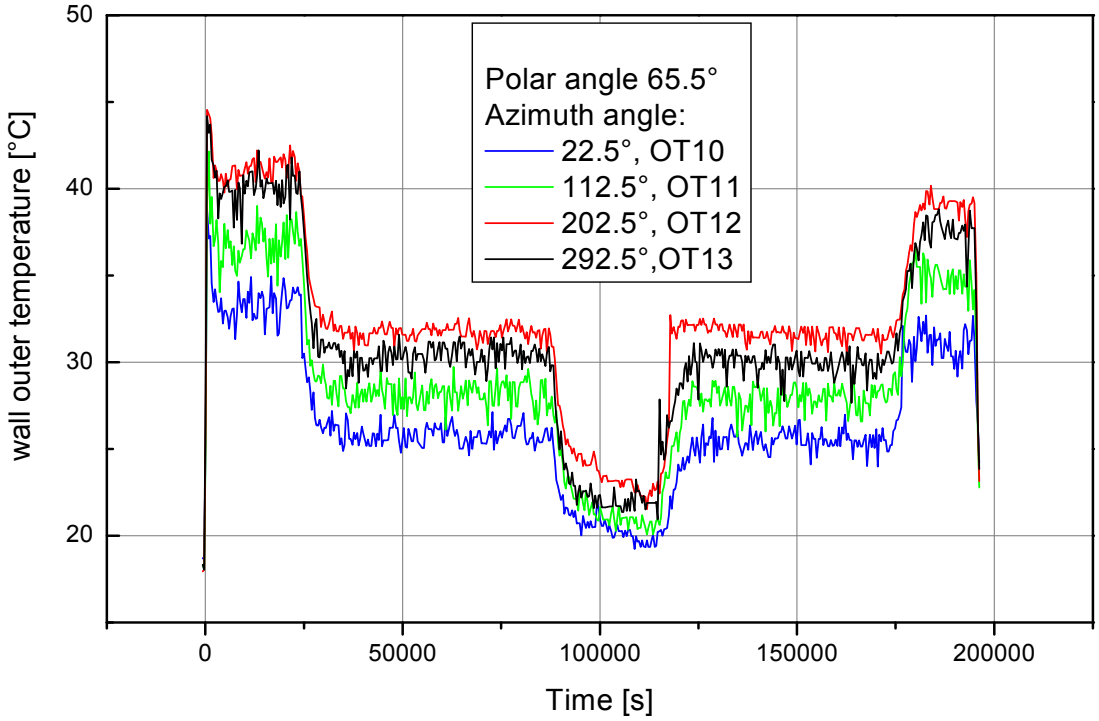

Figure B- 10: L4 vessel wall outer temperatures at polar angle 65.5°

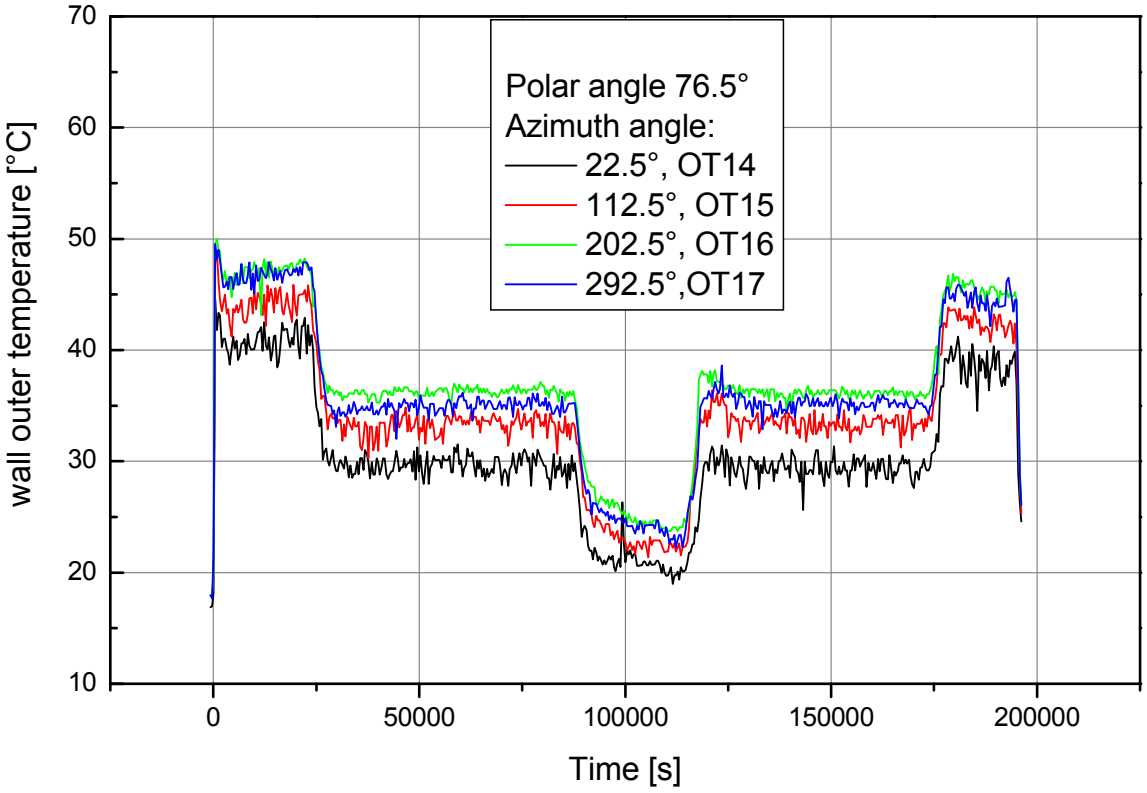

Figure B- 11: L4 vessel wall outer temperatures at polar angle 76.5°

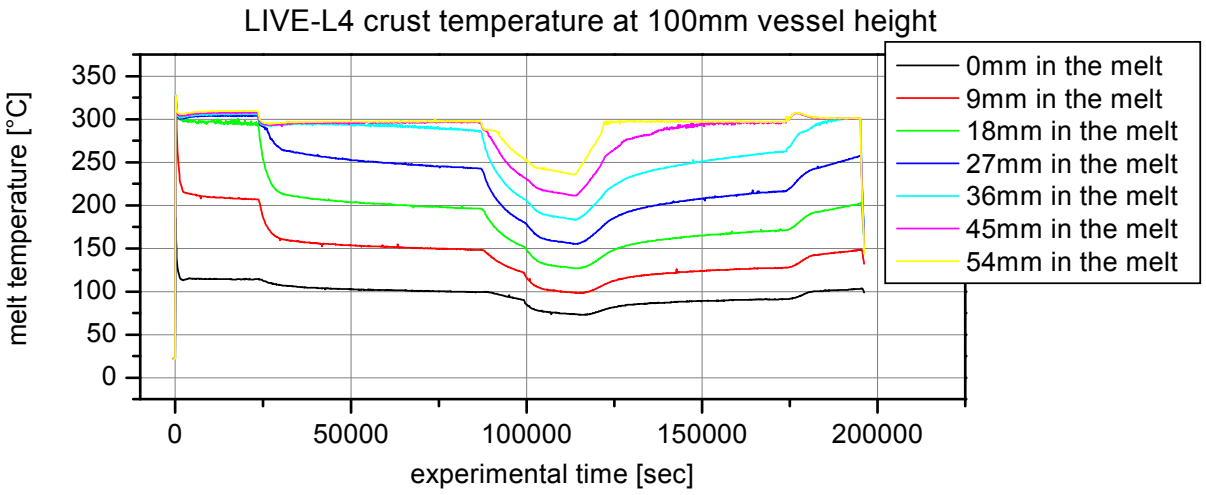

Figure B- 12: L4 crust temperature at 37.6°, 100 mm height

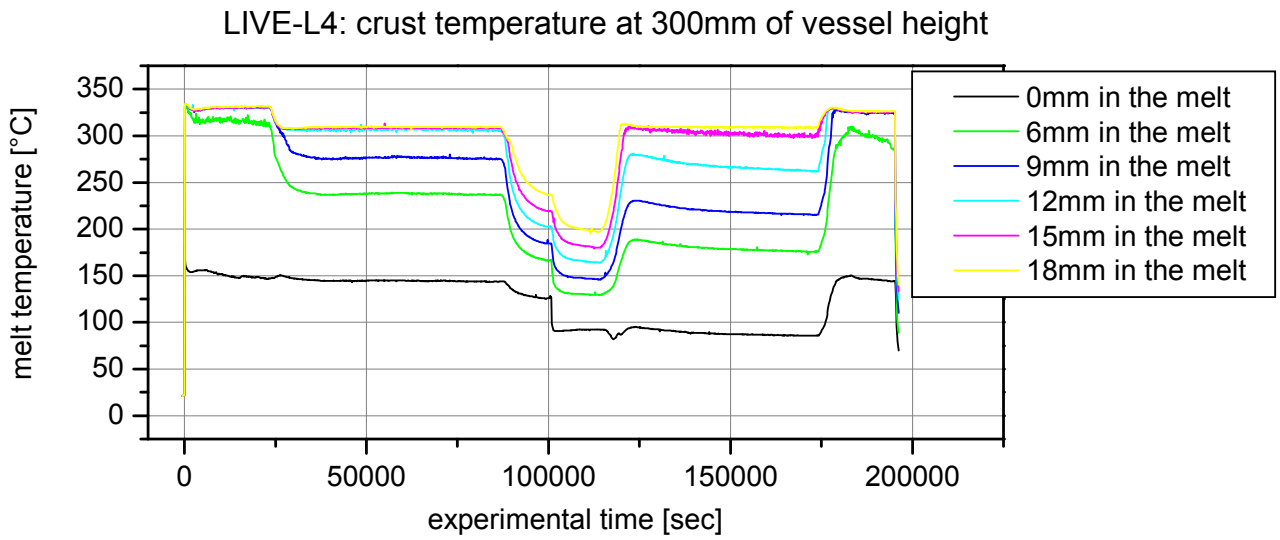

Figure B- 13: L4 crust temperature at CT2, 200 mm height

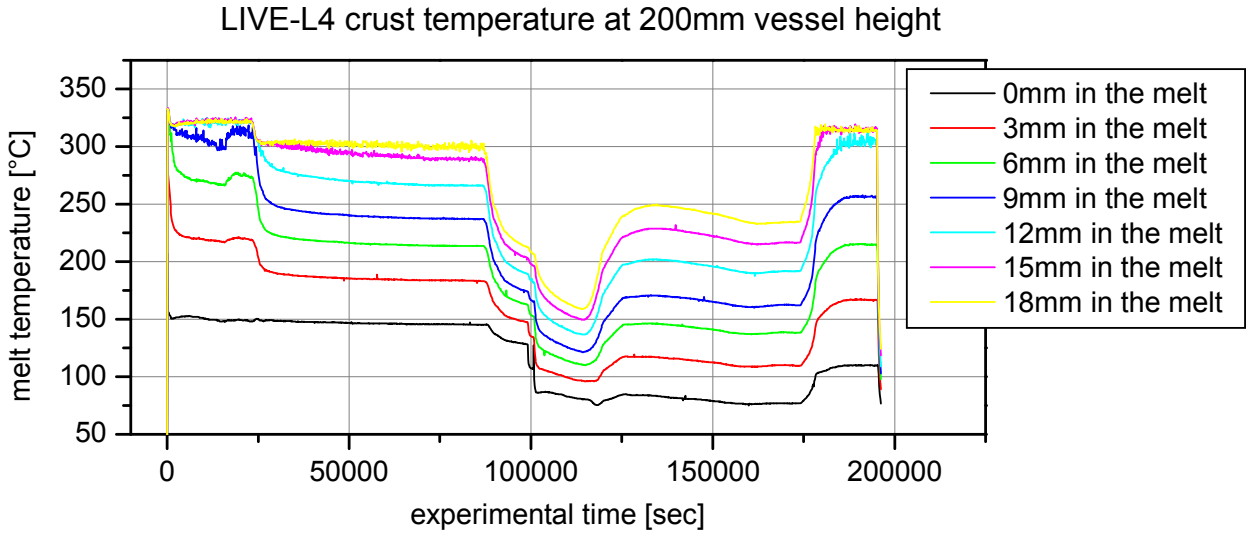

Figure B- 14: L4 crust temperature at 66.9°, 300 mm height

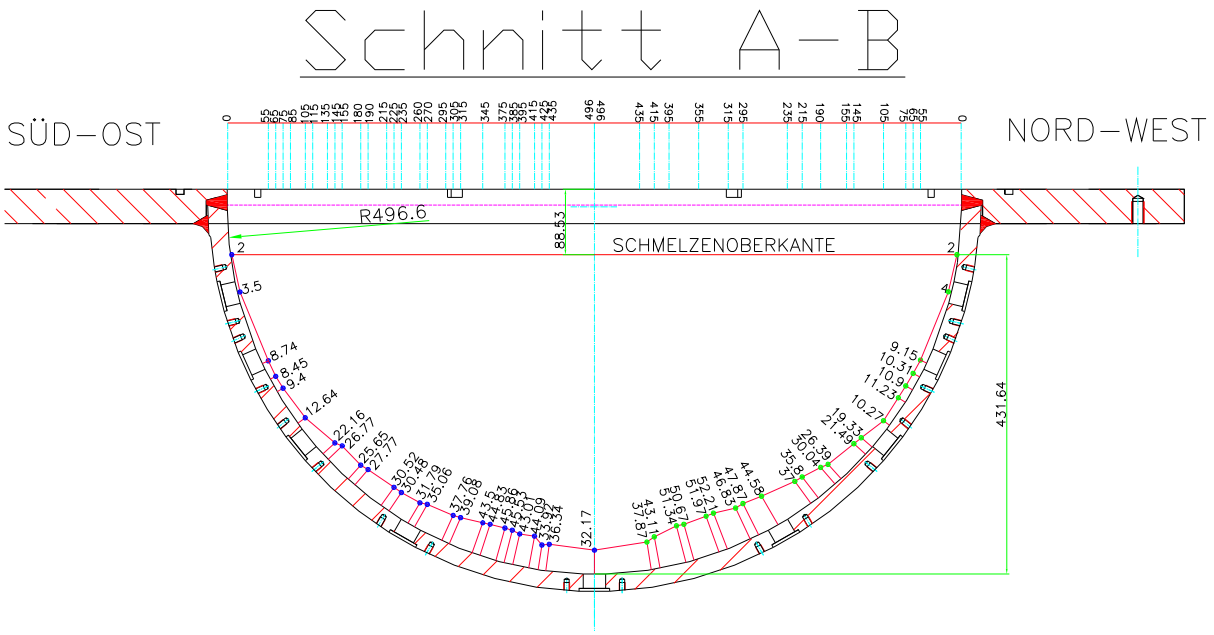

Figure B- 15: Crust thickness profile at the end of 15 kW, azimuth 157.5°-337.5°

Annex C Test data of LIVE-L5L

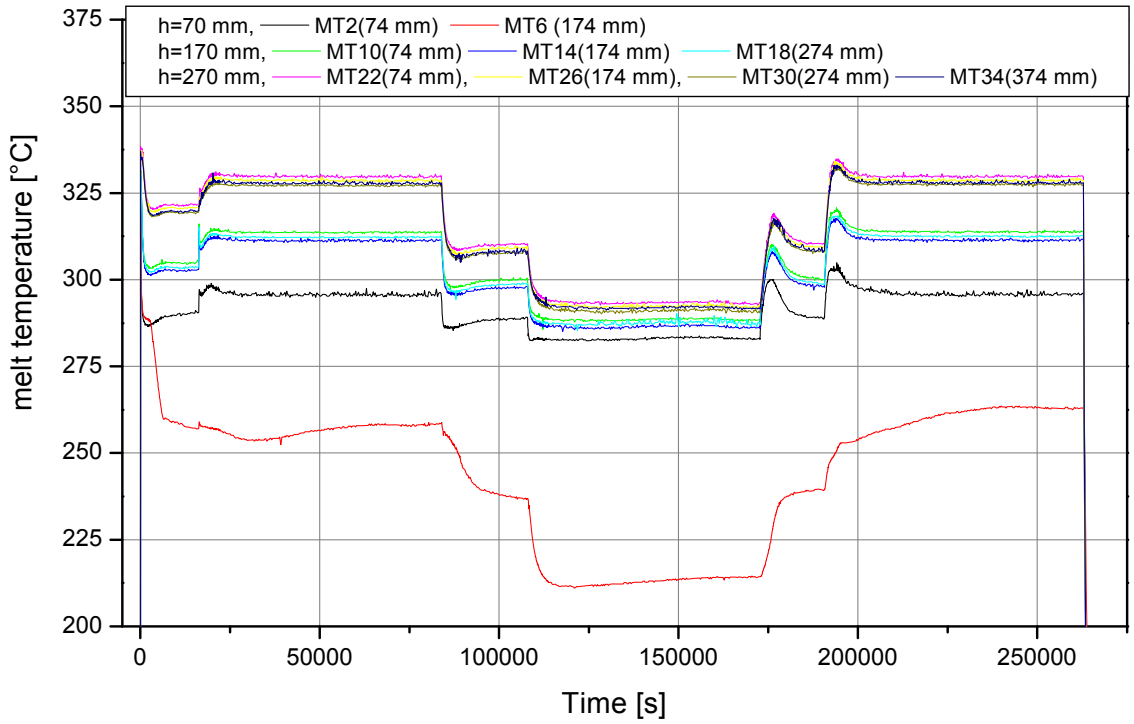

Figure C- 1: L5L melt pool temperature at azimuth angle 90°

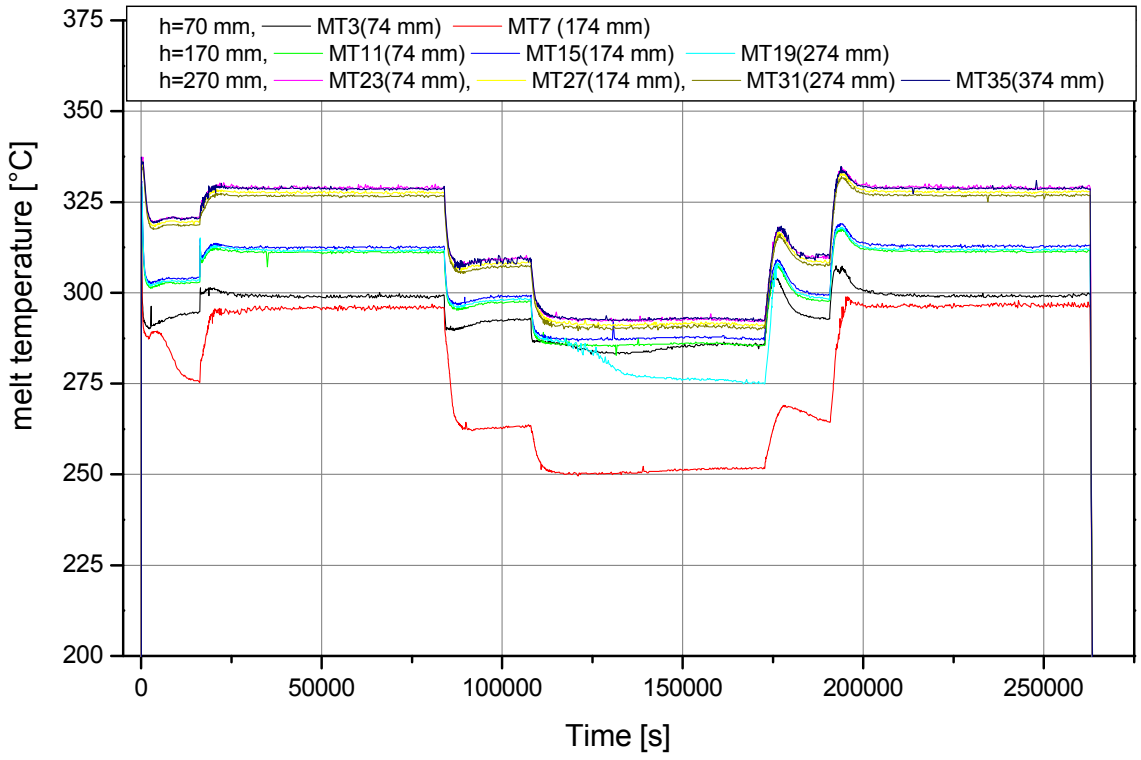

Figure C- 2: L5L melt pool temperature at azimuth angle 180°

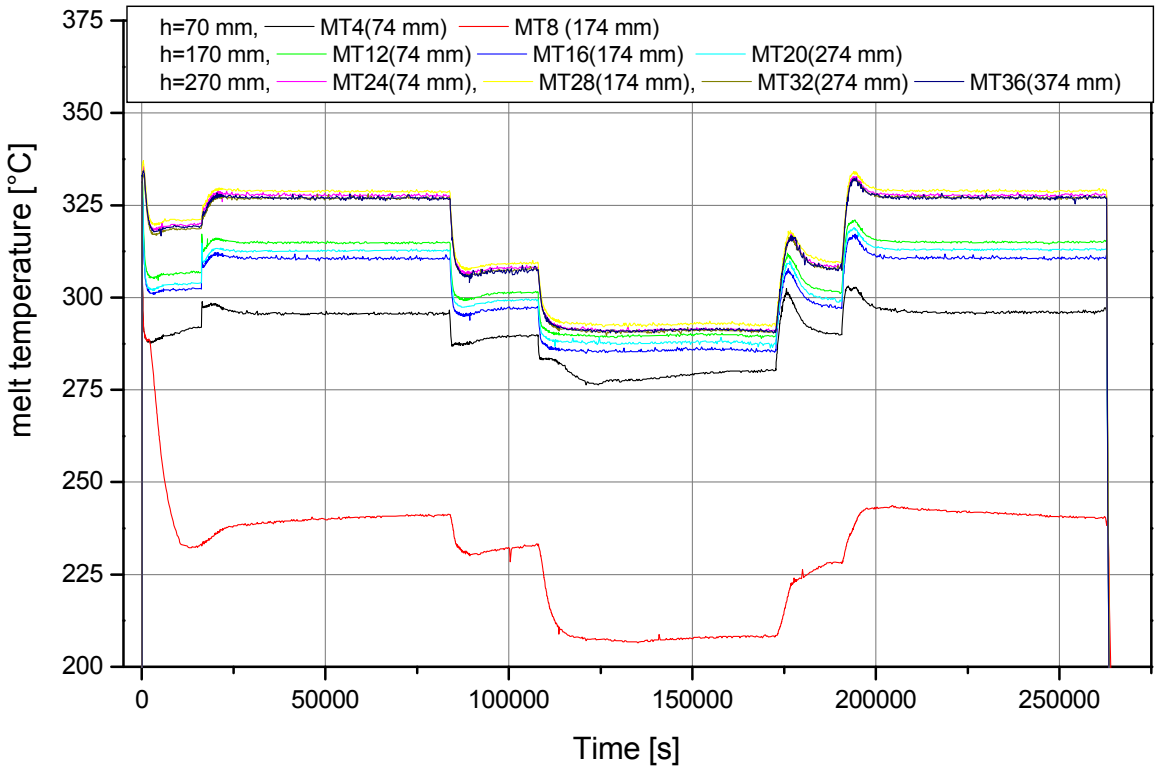

Figure C- 3: L5L melt pool temperature at azimuth angle 270°

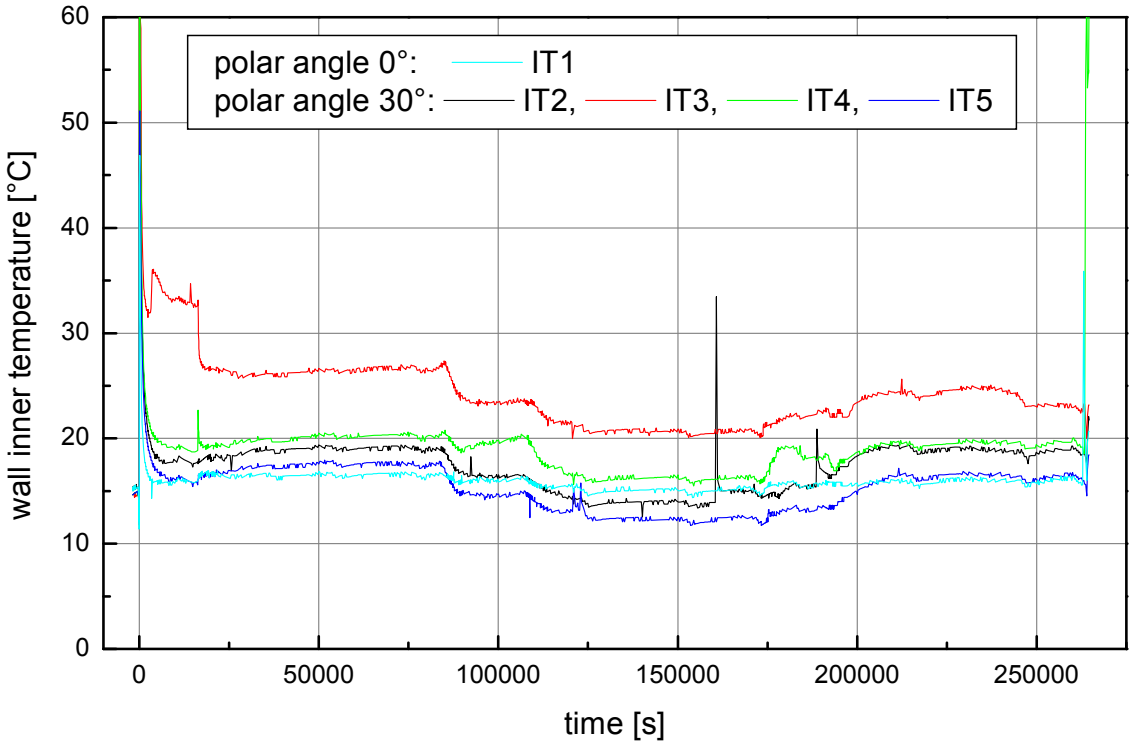

Figure C- 4: L5L test vessel wall inner temperature at 0° and 30°

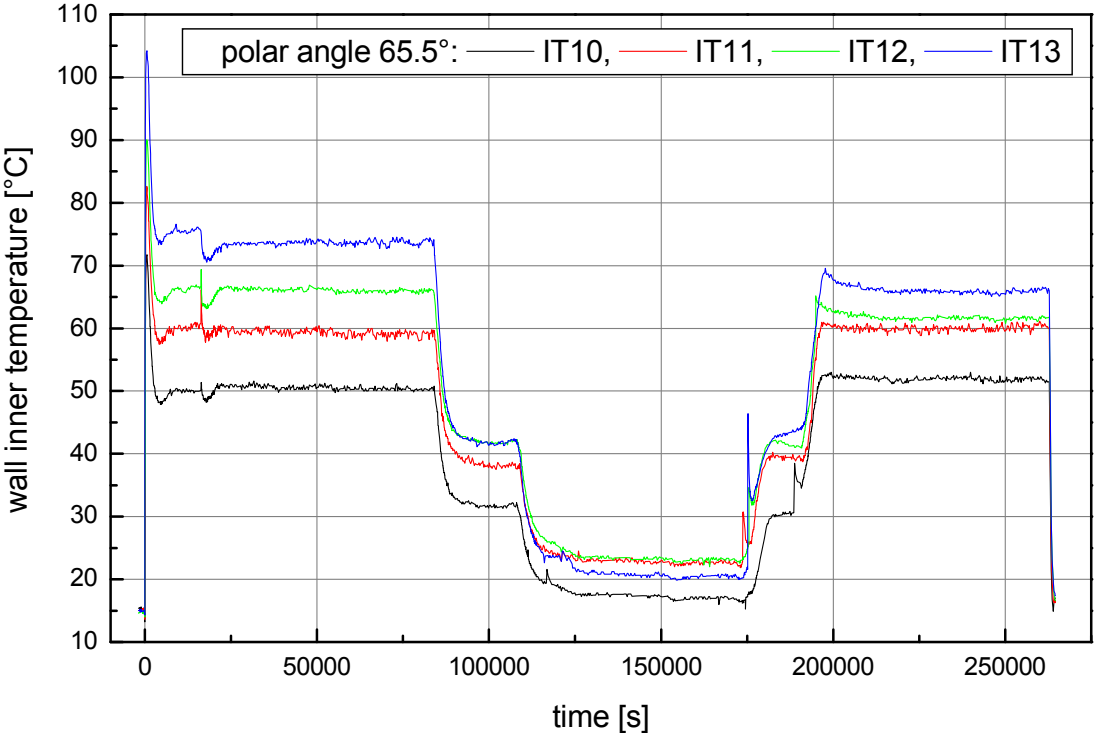

Figure C- 5: L5L test vessel wall inner temperature at 65.5°

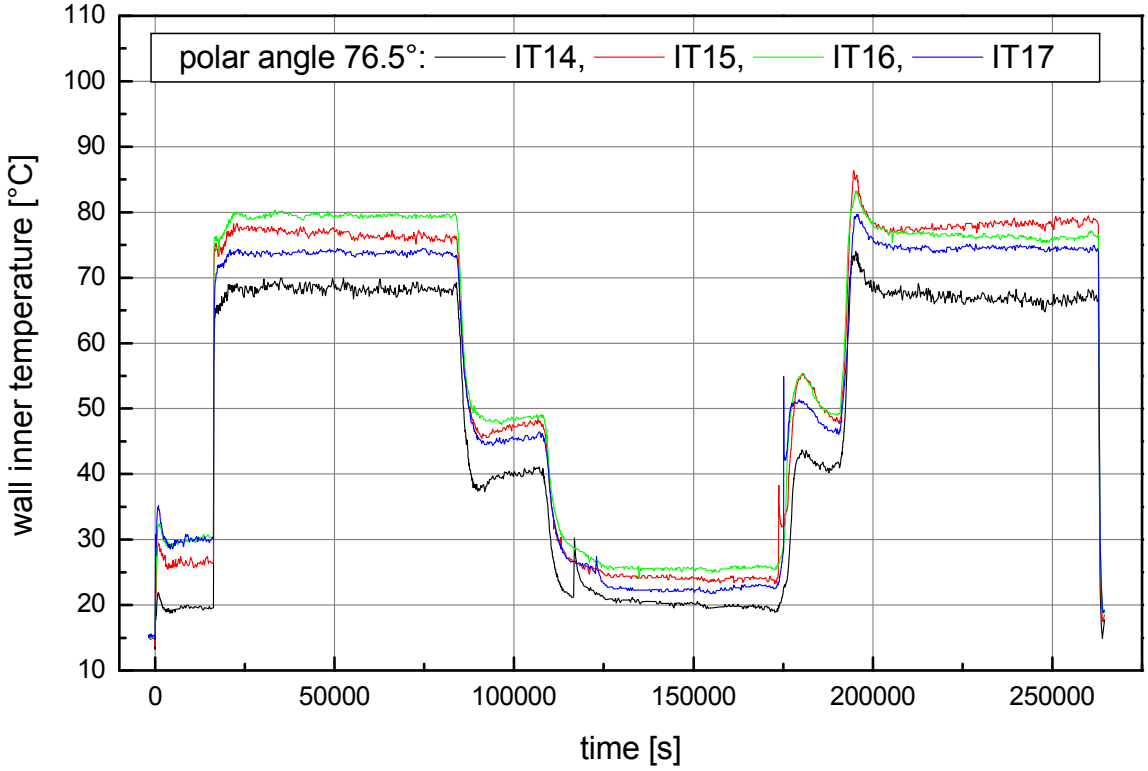

Figure C- 6: L5L test vessel wall inner temperature at 76.5°

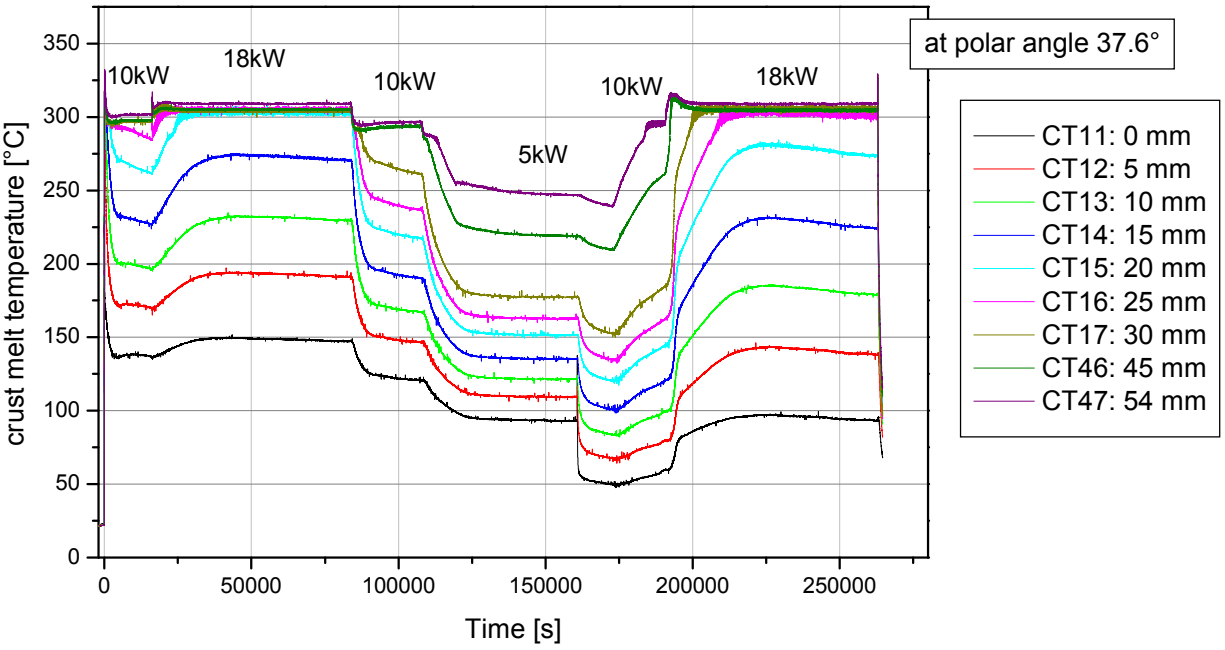

Figure C- 7: L5L crust temperature at 37.6°

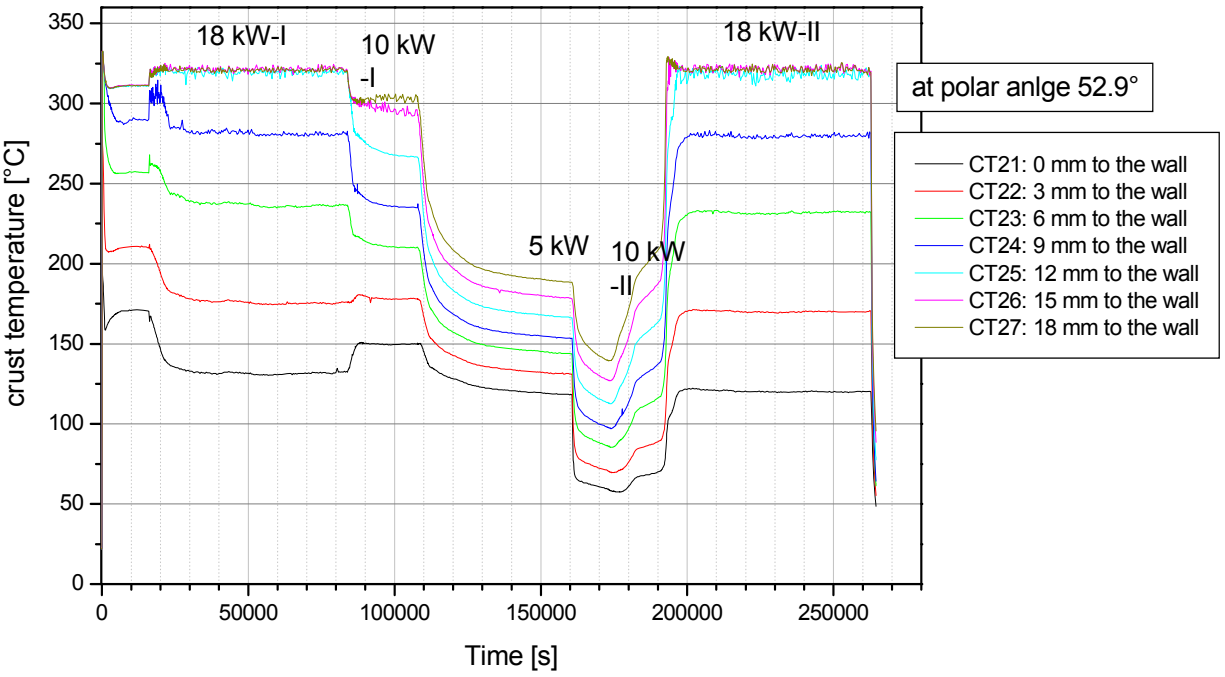

Figure C- 8: L5L crust temperature at 52.9°

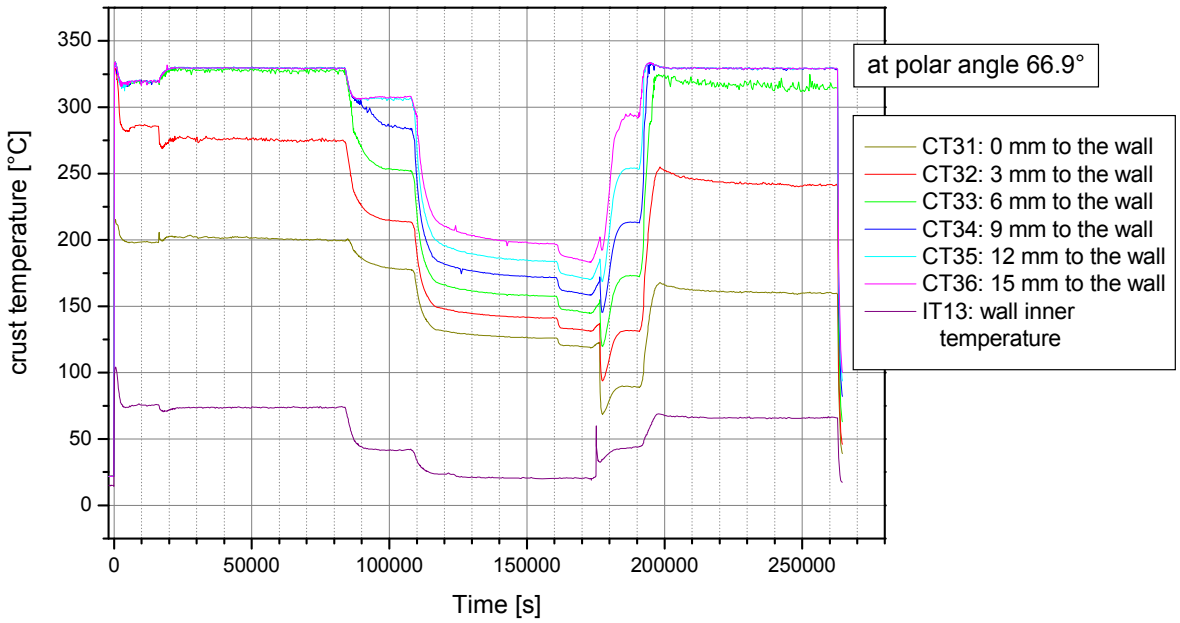

Figure C- 9: L5L crust temperature at 66.9°

Annex D Measurement deviation and error

Table D- 1: relative deviation and relative error in L4 test

Signal	Nr of Meas.	18 kW-I, , 20000-20120 s		10 kW-I, 80000-80120 s		5 kW 110000-110120s		10 kW-II 160000-160120s		15 kW 190000-190120	
		rel. deviation	rel. error	rel. deviation	rel. error	rel. deviation	rel. error	rel. deviation	rel. error	rel. deviation	rel. error
MT_{mean}	25	0.06%	0.01%	0.07%	0.01%	0.08%	0.02%	0.07%	0.01%	0.06%	0.01%
CT_{mean}	25	0.22%	0.04%	0.14%	0.03%	0.11%	0.02%	0.12%	0.02%	0.20%	0.04%
mean in the crust	25	0.16%	0.03%	0.11%	0.02%	0.10%	0.02%	0.10%	0.02%	0.11%	0.02%
OT_{mean}	25	1.51%	0.30%	1.39%	0.28%	1.22%	0.24%	1.28%	0.26%	1.46%	0.29%
IT_{mean}	25	0.30%	0.06%	0.42%	0.08%	0.56%	0.11%	0.61%	0.12%	0.35%	0.07%
AT	25	0.47%	0.09%	1.18%	0.24%	1.16%	0.23%	0.53%	0.11%	0.07%	0.01%
ZT	25	3.12%	0.62%	2.08%	0.42%	2.51%	0.50%	1.96%	0.39%	4.37%	0.87%
DF	25	0.21%	0.04%	0.72%	0.14%	0.15%	0.03%	0.09%	0.02%	1.47%	0.29%
HE	25	0.10%	0.020%	0.25%	0.050%	0.27%	0.054%	0.22%	0.044%	0.10%	0.020%
HF_{mean}	25	3.60%	0.70%	6.00%	1.20%	8.90%	1.80%	6.40%	1.30%	3.70%	0.70%
HF_{lev2}	4	34.60%	17.30%	59.21%	29.61%	48.36%	24.18%	33.73%	16.87%	40.31%	20.15%
HF_{lev3}	4	11.51%	5.75%	13.90%	6.95%	37.49%	18.74%	5.64%	2.82%	13.95%	6.97%
HF_{lev4}	3	19.71%	11.38%	20.81%	12.01%	14.40%	8.31%	10.97%	6.33%	2.47%	1.43%
HF_{lev5}	4	8.53%	4.27%	13.70%	6.85%	9.02%	4.51%	16.94%	8.47%	14.50%	7.25%

Table D- 2: relative deviation and relative error in L5L test

Signal	Nr of meas	1. pouring		18 kW-I, ,		10 kW-I,		5 kW		10 kW-II		18 kW-II	
		15000s-15120 s		80000-80120 s		100000-100120 s		170000-170120 s		185000-185120 s		250000-250120 s	
		rel. de-viation	rel. error	rel. de-viation	rel. error	rel. de-viation	rel. error	rel. de-viation	rel. error	rel. de-viation	rel. error	rel. de-viation	rel. error
MT_{mean}	25	0.04%	0.01%	0.06%	0.01%	0.07%	0.01%	0.08%	0.02%	0.07%	0.01%	0.06%	0.01%
CT_{mean}	25	0.11%	0.02%	0.16%	0.03%	0.14%	0.03%	0.13%	0.03%	0.12%	0.02%	0.23%	0.05%
CT in the crust	25	0.08%	0.02%	0.13%	0.03%	0.09%	0.02%	0.13%	0.03%	0.10%	0.02%	0.14%	0.03%
OT_{mean}	25	1.64%	0.33%	1.83%	0.37%	1.78%	0.36%	1.37%	0.27%	1.77%	0.35%	2.22%	0.44%
IT_{mean}	25	0.46%	0.09%	0.38%	1.32%	0.50%	1.34%	0.72%	1.38%	0.40%	1.32%	0.32%	1.31%
AT	25	0.77%	0.153%	1.67%	0.333%	0.81%	0.162%	1.00%	0.199%	1.68%	0.335%	0.16%	0.032%
ZT	25	4.34%	0.867%	6.90%	1.379%	2.18%	0.435%	0.65%	0.130%	3.07%	0.615%	4.81%	0.962%
DF	25	0.14%	0.028%	0.14%	0.028%	0.14%	0.027%	0.15%	0.030%	0.15%	0.029%	0.18%	0.037%
HE_{total}	25	0.29%	0.057%	0.15%	0.029%	0.15%	0.030%	0.72%	0.143%	0.18%	0.036%	0.13%	0.027%
HF_{mean}	25	4.3%	0.9%	2.9%	0.6%	4.3%	0.9%	6.9%	1.4%	4.3%	0.9%	3.3%	0.7%
HF_{lev2}	3	27.72%	16.006%	19.63%	11.334%	42.35%	24.448%	55.23%	31.889%	52.13%	30.098%	33.02%	19.066%
HE_{lev3}	3	8.62%	4.978%	13.80%	7.968%	13.36%	7.712%	38.58%	27.281%	12.43%	8.791%	5.37%	3.795%
HF_{lev4}	4	22.90%	11.451%	20.48%	10.240%	9.88%	4.942%	16.05%	8.025%	9.24%	4.618%	9.43%	4.714%
HF_{lev5}	4	8.63%	4.315%	9.47%	4.735%	12.72%	6.359%	12.11%	6.053%	11.18%	5.592%	10.26%	5.128%

Annex E CONV calculation

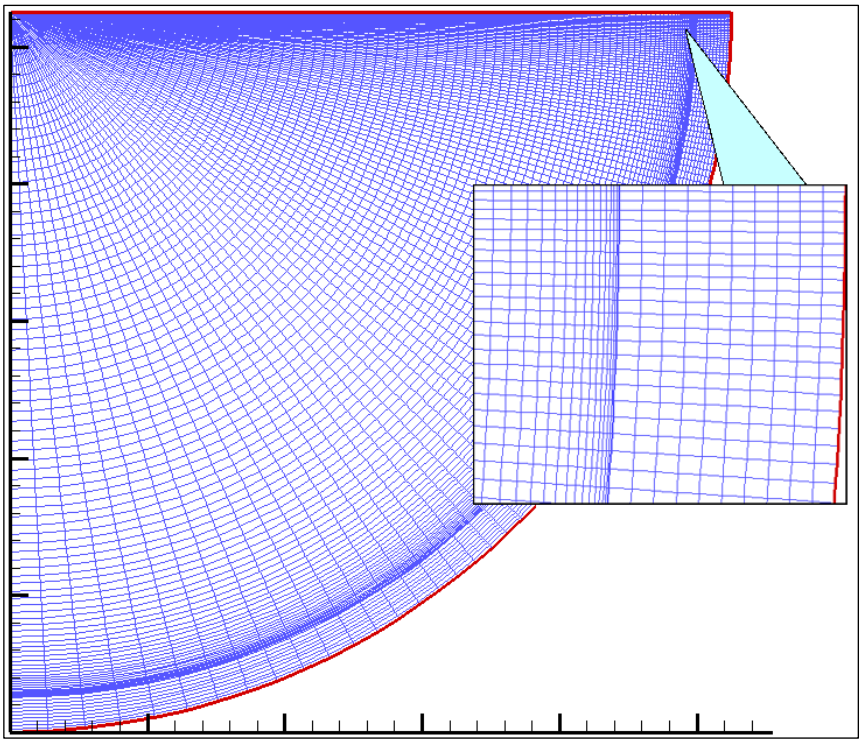

Figure E- 1: Orthogonal curvi-linear grid used in the calculations

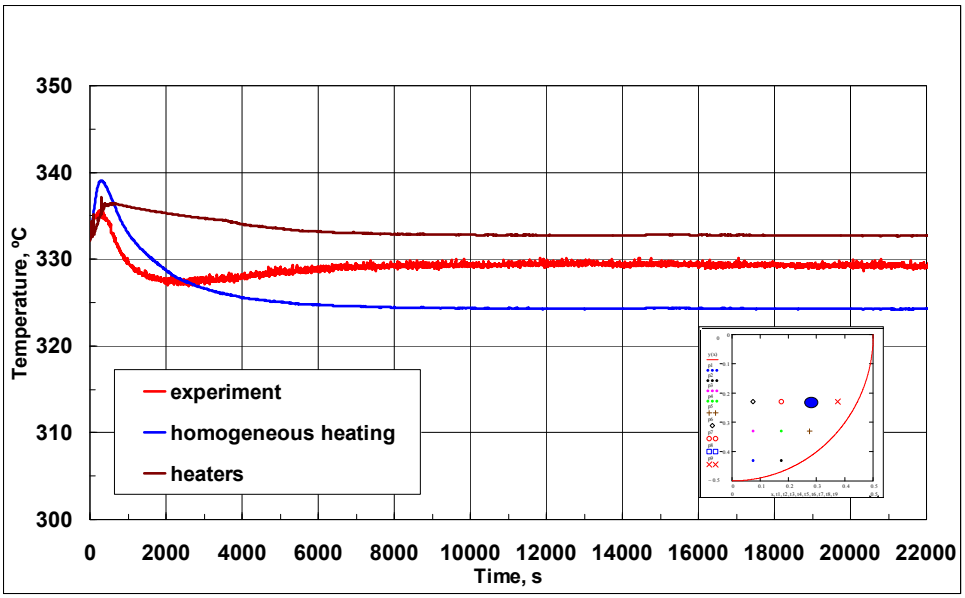

Figure E- 2: Measured and calculated temperature evolution in the bulk of liquid at the first phase of the test (18 kW)

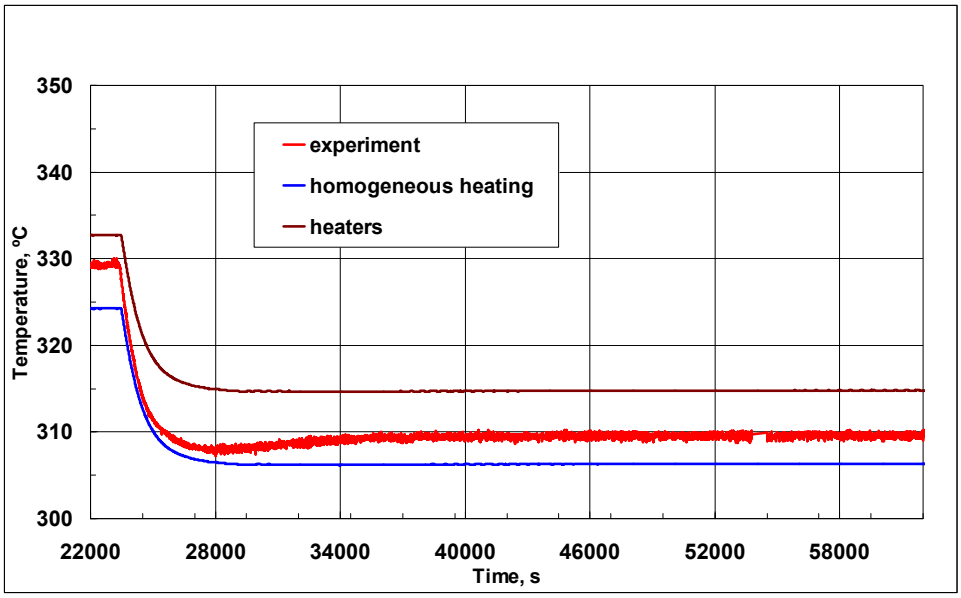

Figure E- 3: Measured and calculated temperature evolution in the bulk of liquid at the second phase of the test (10 kW)

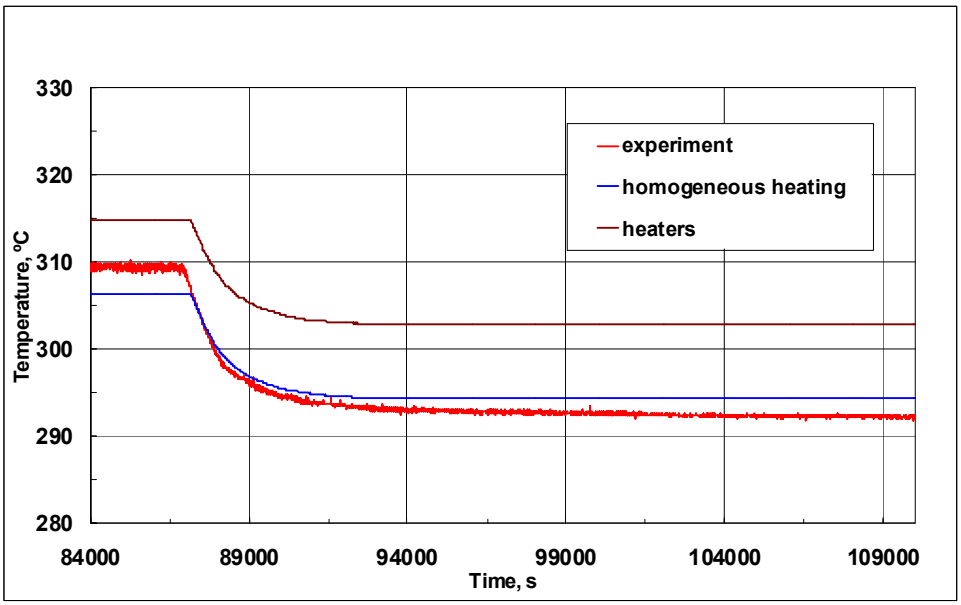

Figure E- 4: Measured and calculated temperature evolution in the bulk of liquid at the third phase of the test (5 kW)

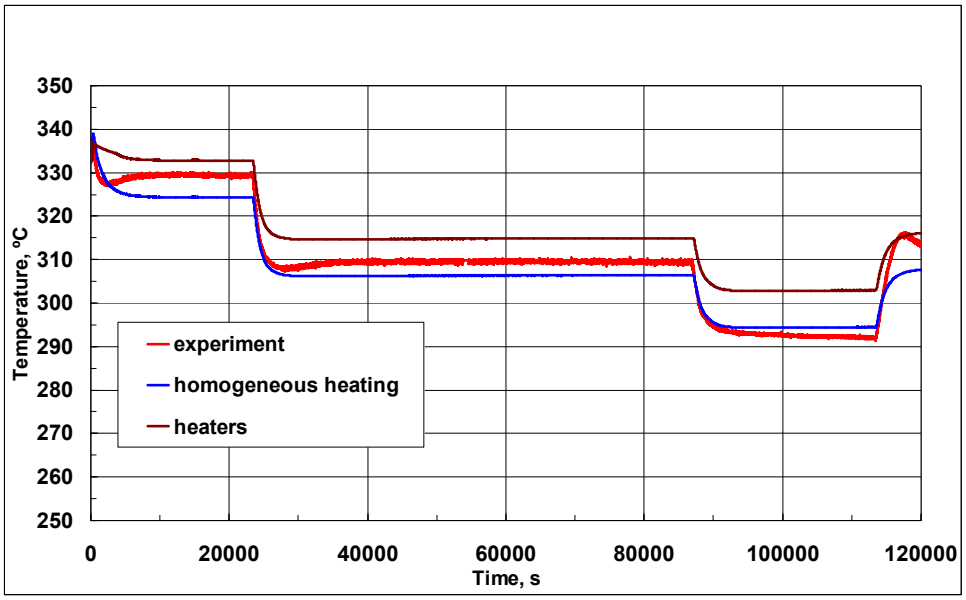

Figure E- 5: Measured and calculated temperature evolution in the bulk of liquid at the first three phases of the test.

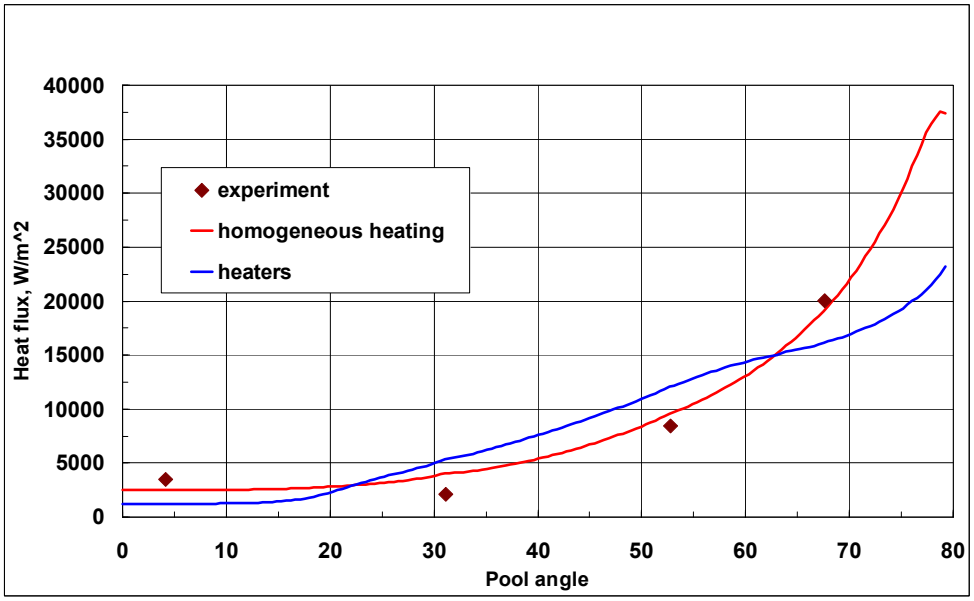

Figure E- 6: Heat flux to the vessel side wall at the first phase of the test (18 kW).

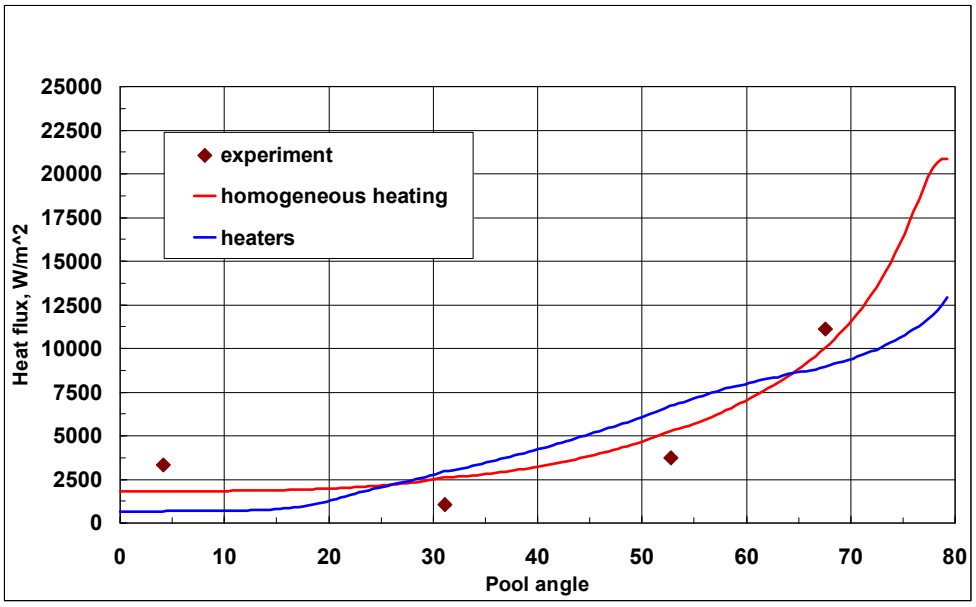

Figure E- 7: Heat flux to the vessel side wall at the second phase of the test (10 kW).

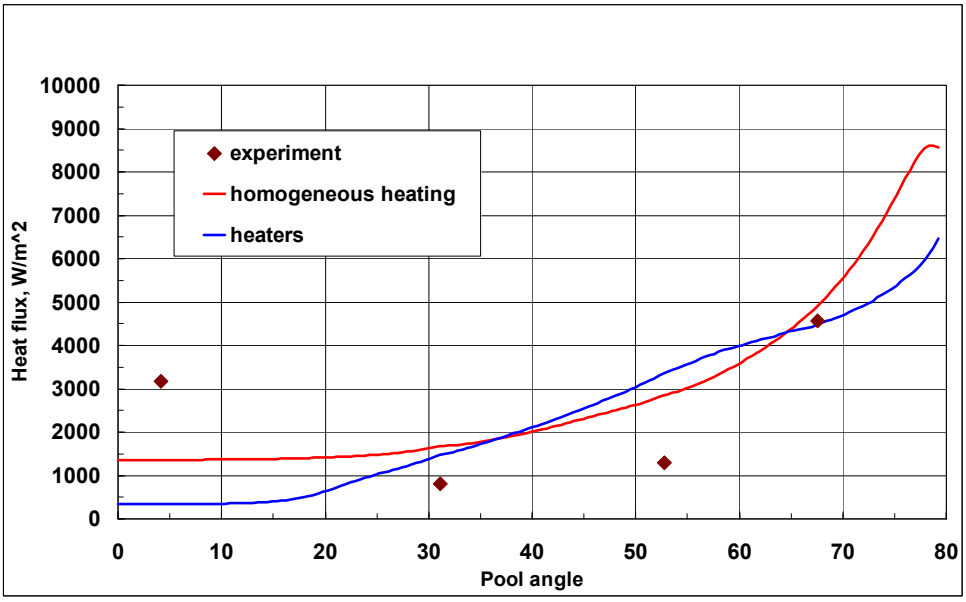

Figure E- 8: Heat flux to the vessel side wall at the third phase of the test (5 kW).

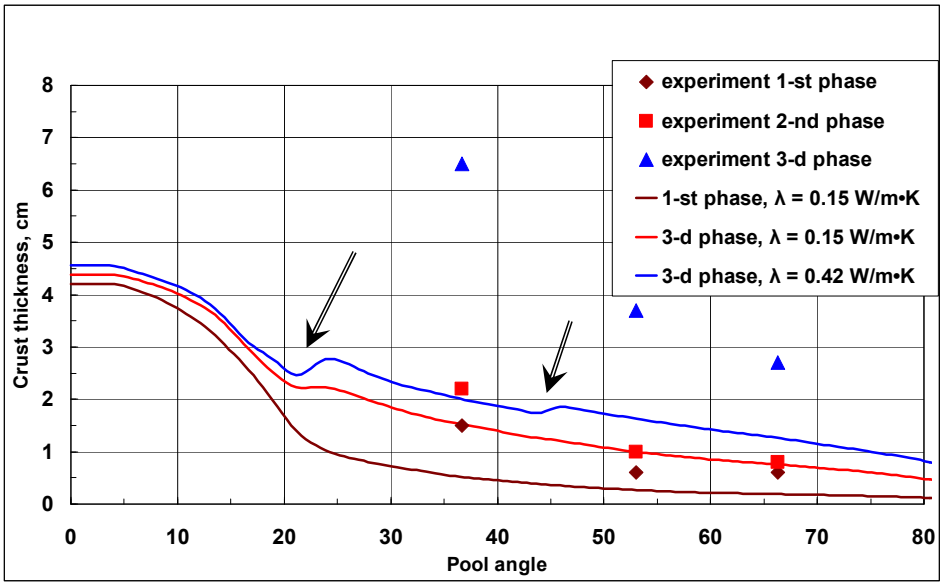

Figure E- 9: Measured and calculated crust thickness.

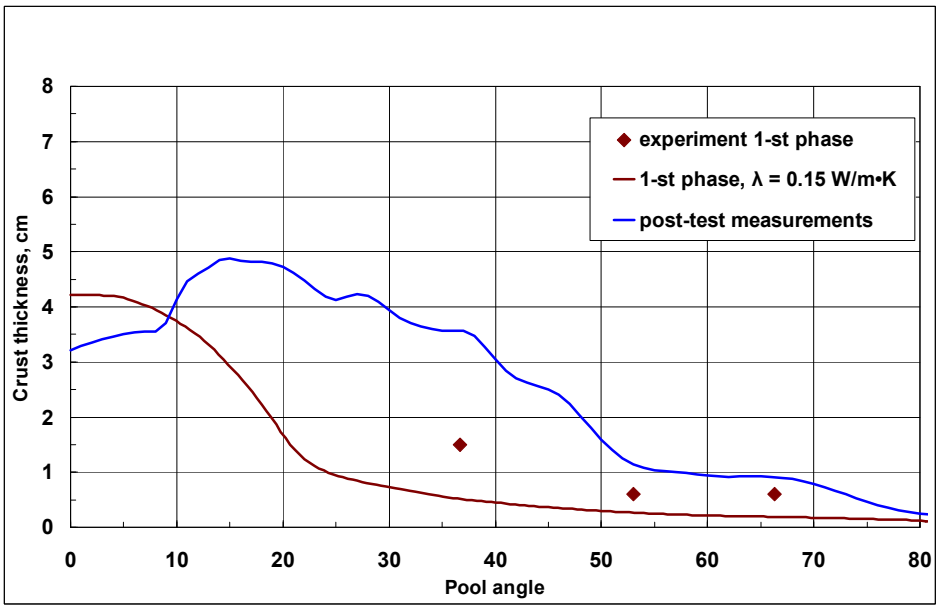

Figure E- 10: The comparison between the crust thicknesses measured at the first phase of the test and at the end of the test as well as the calculated crust thickness.

ISSN 1869-9669
ISBN 978-3-86644-692-2